

**Thermal noise investigations in
gravitational wave research**

Von der Fakultät für Mathematik und Physik
der Gottfried Wilhelm Leibniz Universität Hannover
zur Erlangung des Grades

Doktor der Naturwissenschaften
– **Dr. rer. nat.** –

genehmigte Dissertation von

Luciano Ribichini

geboren am 08. Mai 1971 in Macerata, Italien.

2007

Referent: Prof. K. Danzmann
Korreferent: Prof. M. Kock
Tag der Promotion: 19. Juli 2007
Druckdatum: 01. November 2007

Zusammenfassung

In interferometrischen Gravitationswellendetektoren ist das thermische Rauschen eine der limitierenden Rauschquellen. Effekte, die auf thermischem Rauschen beruhen, dominieren im Frequenzbereich zwischen einigen zehn Hz und einige hundert Hz.

In dieser Arbeit werden zwei Experimente beschrieben, mit denen wir diese Rauschquelle untersuchen.

Im ersten Experiment wurde das „nicht-resonante“ thermische Pendelrauschen untersucht, d.h. die zufällige Pendelbewegung, die durch die Temperatur getrieben wird. Schon Saulson [1] zeigte Anfang der 90er Jahre, dass das Spektrum dieses Rauschens stark von der Art der mechanischen Dissipation abhängt, d.h. dass es sehr wichtig ist, ob viskose oder strukturelle Dämpfung überwiegt. In unseren Untersuchungen wurde das Rauschen stark durch seismische Kopplungen dominiert. Durch Modifikationen der Pendelaufhängung konnte die Empfindlichkeit verbessert werden. Es stellte sich heraus, dass das Holz-ersche Verfahren für die numerische Analyse der mechanischen Kopplungen im Prinzip anwendbar ist. Die bekannte numerische Instabilität des Verfahrens konnte beseitigt werden.

Ziel des zweiten beschriebenen Experimentes war die Vermessung des internen thermischen Rauschens in einer optischen Beschichtung. Zusätzlich zu dem o.g. thermischen Rauschen gewinnen hier von Braginsky [2, 3, 4] in den 90er Jahren angeführte, von lokalen Variationen der Temperatur getriebene Rauschbeiträge an Bedeutung. Um das in genannte Literatur beschriebene Rauschen direkt zu untersuchen, wurde ein Experiment mit einem Mikroresonator entworfen. Dazu wurde mit Ion-Beam-Sputtering Techniken ein Etalon auf ein kommerzielles Substrat beschichtet. Auch bei der Realisierung dieses Experimentes trafen wir auf unerwartete Schwierigkeiten, da die harte Anforderungen an die Toleranzen des Etalons die Möglichkeiten der Beschichtungsfirma überschritten. In Kooperation mit der Beschichtungsfirma wurde versucht, einen Kompromiss zwischen den beschichtungstechnischen Möglichkeiten und minimalen experimentellen Anforderungen zu finden. Mit den heutigen bei den weltweit besten Firmen verfügbaren Technologien und anhand der gewonnenen Erfahrungen sollte die Fertigung eines solchen Etalons möglich sein.

Schlagwörter: Pendel, Etalon, Beschichtung.

Summary

Thermal noise is a limiting noise source for interferometric gravitational wave detectors. More precisely, thermal noise effects are expected to be relevant in the frequency range from a few tens Hz up to a few hundred Hz.

In this work we describe two experiments undertaken to investigate this noise source.

The aim of the first experiment was to measure off-resonant thermal noise due to the random pendulum movement, driven by temperature. In the early 1990s Saulson [1] pointed out that the spectrum of this motion is very sensitive to the dominant dissipation mechanism, i.e. it matters whether the dissipation happens through a friction-like mechanism, or through internal damping. While investigating this effect we faced the unexpected influence of seismic noise that led us to develop modifications to the pendulum suspension, which resulted in an enhancement of the instruments sensitivity. It resulted also that the Holzer's method for the numerical analysis of the mechanical couplings could in principle be used. The well-known numerical instability of the method has been practically eliminated.

The second experiment was aimed at investigating internal thermal noise effects in optical coatings. In this case, additional noise contributions, studied in the late 1990s by Braginsky [2, 3, 4], play an important role. In order to investigate such effects we drafted an experiment with a microresonator. The microresonator itself was coated on a commercial substrate by using the Ion Beam Sputtering technique. Also here, during realization of the experiment, we faced some unexpected difficulties. In this case the etalon itself turned out quite challenging to produce for the coating company given the strict specification needed to reach our goal. We then started an intensive collaboration with the coating company to tailor our specification to the production constraints. As a result of this collaboration, we believe that the Etalon could be successfully produced, albeit at the edge of present-day technology.

Keywords: Pendulum, Etalon, Coating.

Contents

Zusammenfassung	i
Summary	iii
1. Introduction	3
2. Toward off-resonant thermal noise measurement	5
2.1. Thermal noise of the pendulum: velocity vs. internal damping	5
2.1.1. A quantitative example	7
2.2. Pendulum transfer functions	7
2.2.1. One stage	8
2.2.2. Two stages	9
2.2.3. Three [identical] stages	11
2.3. The experimental setup	15
2.4. The noise floor	16
3. Optimization of the pendulum suspension	19
3.1. Seismic noise still leaking into the system	19
3.2. Enhancement of the moments of inertia	21
3.3. Input-output formalism: Holzer's method	21
3.3.1. A simple mass	23
3.3.2. An ideal spring	23
3.4. Consistency checks	23
3.4.1. Two masses, two springs	24
3.4.2. A spring-mass system: TF	24
3.5. Two, three harmonic oscillators connected in series	25
3.5.1. Lagrangian formalism for a 2-stage-system	25
3.5.2. Matrix formalism for a 2-stage-system	26
3.5.3. Lagrangian formalism for 3 [identical] stages	26
3.5.4. Matrix formalism for 3 [identical] stages	27
3.6. Harmonic oscillator [spring-mass system] vs. pendulum	27
3.7. The matrix for a pendulum	28
3.7.1. A double pendulum in the matrix formalism	29
3.7.2. A triple pendulum in the matrix formalism [identical stages]	30
3.8. Generalization to complex systems: Newton's equations method	30
3.9. Two degrees of freedom: input-output method	31
3.10. Stabilization of the algorithm	32
3.11. The next step	33

4. Internal thermal noise	35
4.1. Thermal noise in mirror coatings	35
4.2. From elasticity theory to the thermoelastic problem	36
4.2.1. The strain and stress tensors	36
4.2.2. Hooke's law	39
4.2.3. The equilibrium equations	42
4.2.4. Equilibrium of an elastic body constrained by a plane	45
4.3. The thermoelastic problem	49
4.3.1. Computation of the stress at the free surface: $\sigma_{zz} _{z=0}$	52
4.3.2. Computation of the displacement of the free surface: $\bar{X}(t)$	54
4.3.3. Computation of the spectrum of the thermoelastic noise	54
4.3.4. Interpretation of equation (4.3.36)	56
4.4. Photo-thermal noise	57
4.5. Quantitative comparison between the different thermal noise effects	59
5. Toward internal thermal noise measurement	61
5.1. Shaping the experiment around the required sensitivity	61
5.1.1. Calibration issues	63
5.2. Tight constraints on the etalon	63
5.2.1. Etalon's internal tilt	67
5.2.2. Etalon production: a challenge for thin film technology	68
5.3. Etalon performance	70
5.4. Additional etalon simulations	70
5.4.1. Temperature tuning	73
6. Conclusion and outlook	75
A. Parameter list for internal thermal noise calculations	77
B. Shot noise and electronic noise sources	81
B.1. Shot noise	81
B.2. Electronic noise sources	82
C. Etalon simulations	85
Thanks	91

1. Introduction

Gravitational waves (henceforth GW) are ripples in the curvature of space-time and manifest themselves as fluctuating forces on the masses in the wave's path. They are a consequence of Einstein's general relativity, but since their predicted amplitude is very small, only in the 1960s did the scientific community start experiments to detect them. There are currently some detectors in operation, whose sensitivity is constantly improving. Even though a direct detection has not yet happened, an indirect one is well accepted by the scientific community [5], confirming Einstein's theory. All types of detectors detect a signal h , which in the case of an interferometric GW detector is

$$h = 2 \frac{\Delta L}{L}$$

where L is the instrument's length.

In the time domain this quantity is obviously dimensionless, but as is customary in GW research, people prefer to speak about the amplitude spectral density (also denoted by h) which is the Fourier transform¹ of h .

The dimension of the amplitude spectral density h is

$$[h] = \frac{1}{\sqrt{\text{Hz}}}.$$

In order to achieve a direct measurement of gravitational wave, the signal h (also called *strain amplitude*) needs to be as small as possible. This task is currently underway and provides the motivation a large part of this work. Figure 1.1 shows the design sensitivity of GEO600 [6], one of the interferometric gravitational wave detectors which is already taking data of scientific value.

The sensitivity of GW detectors, like that shown in Figure 1.1, is ultimately limited by a number of fundamental noise sources. In the case of interferometric gravitational wave detectors their core technologies, namely laser interferometry and suspended optics, lead directly to noise sources that invariably limit their sensitivity. With increasing frequency we list them as follows:

- *Seismic noise*: intrinsic noise of the Earth surface, also present in the absence of exceptional events like earthquakes: it is mainly due to ocean waves and anthropogenic noise.
- *Suspension thermal noise*: noise of the mechanical suspension systems holding the optics, driven by temperature fluctuations.

¹Actually since ΔL is a noise term whose average is equal to zero, it is necessary to take its power spectrum and then the square root.

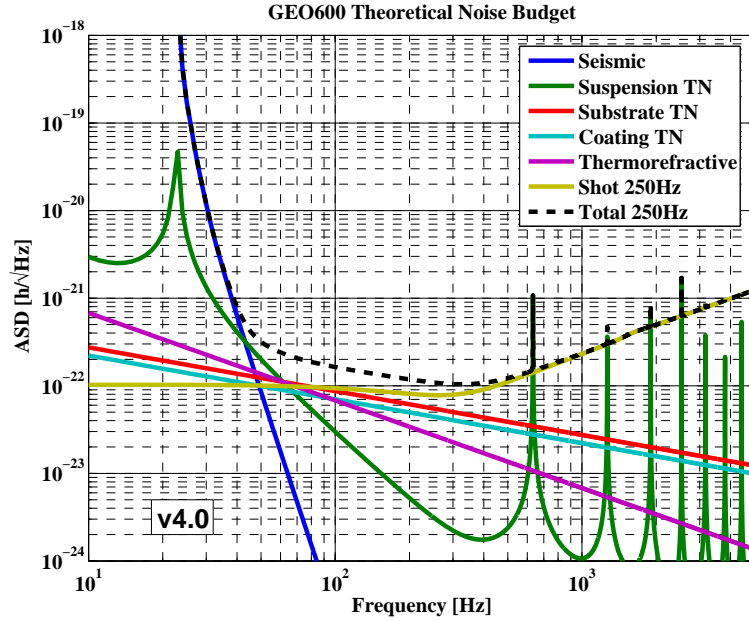


Figure 1.1.: Sensitivity curve (strain as a function of the frequency) for GEO600 with an optimization at 250 Hz.

- *Internal thermal noise*: noise of the optical components themselves (from coatings and from substrates), also driven by temperature fluctuations.
- *Shot noise*: noise due to the quantum nature of the light (in our case coming from a laser).

In this work we report the results of our investigations of thermal noise within the framework of gravitational wave research, that is we will show our attempt to approach, by means of a small-scale experiment, a sensitivity level at which thermal noise effects become measurable.

2. Toward off-resonant thermal noise measurement

2.1. Thermal noise of the pendulum: velocity vs. internal damping

The whole optical setup of interferometric GW detectors is suspended as a multiple-stage pendulum to provide isolation from seismic noise. Even in the case of perfect seismic isolation, the suspended optics are expected to exhibit a residual movement due to some sort of Brownian motion. Here, following Saulson's [1] approach (which relies on the fluctuation-dissipation theorem of Callen and coworkers [7]), we will show how different dissipation mechanisms show up in different motions of the suspended mass.

Consider a one dimensional system with mass m moving along the x -axis, whose equation of motion can be written as

$$m\ddot{x} + f(\dot{x}) + g(x) = F \quad (2.1.1)$$

where

- x is the coordinate
- $f(\dot{x})$ is a term which describes a friction force
- $g(x)$ is a force term, resulting from a potential
- F is an external force.

If we Fourier transform this equation¹ we obtain²

$$-m\omega^2\tilde{x} + f(i\omega\tilde{x}) + g(\tilde{x}) = \tilde{F} \quad (2.1.2)$$

(ω is the angular frequency). Now we introduce the *impedance*

$$Z \equiv \frac{\tilde{F}}{\tilde{v}} \equiv \frac{\tilde{F}}{i\omega\tilde{x}} \quad (2.1.3)$$

The fluctuation-dissipation theorem states that each time we have dissipation, the corresponding variable is subject to fluctuation, whose one-sided spectral density is given by

$$S_x(\omega) = \frac{4k_B T}{\omega^2} \Re(Z^{-1}) \quad (2.1.4)$$

where

¹We suppose that both f and g are linear functions of their respective arguments.

²We will indicate the fourier trasform of a quantity x with \tilde{x} .

2. Toward off-resonant thermal noise measurement

- $\Re(Z^{-1})$ indicates the real part of Z^{-1}
- k_B is the Boltzmann's constant
- T is the temperature.

Taking the square root of this equation gives the *linear spectral density*

$$\delta\tilde{x} \equiv \sqrt{S_x(\omega)} = \sqrt{\left(\frac{4k_B T}{\omega^2} \Re(Z^{-1})\right)}. \quad (2.1.5)$$

The linear spectral density has the dimension of $\text{m}/\sqrt{\text{Hz}}$. It depends heavily on the dissipation mechanism, as we shall see in the next two examples.

Let's suppose now that the damping is proportional to the velocity through a damping constant γ , then the equation of motion takes the form (considering the system being also driven by a spring-like term with spring constant k)

$$m\ddot{x} + \gamma\dot{x} + kx = F. \quad (2.1.6)$$

In the Fourier domain we have

$$-m\omega^2\tilde{x} + i\gamma\omega\tilde{x} + k\tilde{x} = \tilde{F}. \quad (2.1.7)$$

The impedance and its inverse are respectively

$$Z = \gamma + i\left(m\omega - \frac{k}{\omega}\right) \quad (2.1.8)$$

$$\frac{1}{Z} = \frac{\gamma - i\left(m\omega - \frac{k}{\omega}\right)}{\gamma^2 + \left(m\omega - \frac{k}{\omega}\right)^2} \quad (2.1.9)$$

The linear spectral density of the displacement in the case of velocity damping is

$$\delta\tilde{x}^{(vd)} \equiv \sqrt{S_x^{(vd)}(\omega)} = \sqrt{\frac{4k_B T \gamma}{\omega^2 \gamma^2 + (m\omega^2 - k)^2}}. \quad (2.1.10)$$

In the case of internal damping the dissipation is taken into account by replacing the spring constant k with a complex one $k^* = k(1+i\phi)$, and therefore setting $\gamma = 0$. Starting from the equation of motion

$$m\ddot{x} + k^*x = F \quad (2.1.11)$$

and following the same procedure as before we obtain

$$\delta\tilde{x}^{(id)} \equiv \sqrt{S_x^{(id)}(\omega)} = \sqrt{\frac{1}{\omega} \frac{4k_B T k \phi}{k^2 \phi^2 + (m\omega^2 - k)^2}}. \quad (2.1.12)$$

2.1.1. A quantitative example

We introduce the angular resonant frequency ω_0

$$\omega_0 \equiv \sqrt{\frac{k}{m}}$$

and the quality factor Q , given by

$$Q \equiv \frac{\omega_0}{\Delta\omega}$$

where $\Delta\omega$ is the full width measured at the half-power points. We then plot the displacement relative to the two models given the following parameters, which are close to those actually used in our experiment.

Physical quantity	Numerical value	Units
m	$50 \cdot 10^{-3}$	Kg
$f_0 = \frac{\omega_0}{(2\pi)}$	1.3	Hz
Q	10^4	–
$\phi \equiv \frac{1}{Q}$	10^{-4}	–
$\gamma = m \frac{\omega_0}{Q}$	$4.08 \cdot 10^{-5}$	Kg · s ⁻¹
T	300	K

As shown in Figure 2.1 the two models result in different displacements, particularly away from the angular resonance frequency ω_0 .

Our first goal was to investigate which of the two models is adequate in the case of a pendulum suspension, that is we wanted to measure the off-resonant thermal noise of a pendulum suspension. Being aware of the extremely small displacement we undertook to measure, we set our sensitivity goal initially to 10^{-17} m/ $\sqrt{\text{Hz}}$ at 100 Hz

2.2. Pendulum transfer functions

From the beginning we addressed what we regarded as the main noise source to be expected in our experiment: seismic noise. In Figure 2.2 we show a fit of a typical seismic spectrum compared to the signal we wanted to measure. From this we realize that the isolation system has to provide *at least seven orders of magnitude of isolation at 100 Hz*. By far the most common tool to provide isolation is a pendulum in one of its variants. A pendulum provides attenuation above its resonance frequency, that is if we shake the suspension point, the mass at the lower end will shake less for excitations whose frequencies are greater than the resonant frequency of the pendulum itself.

Let's now make these ideas more quantitative.

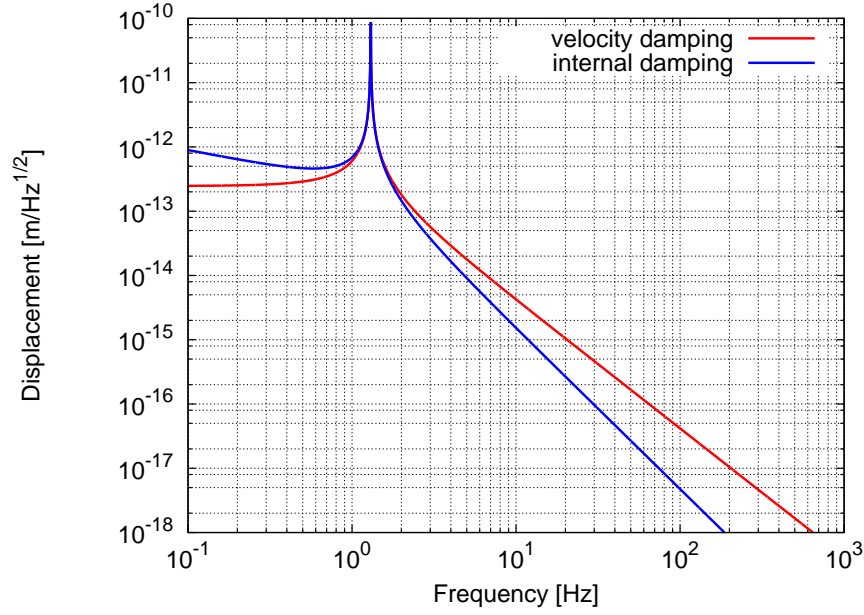


Figure 2.1.: Linear spectral density of the displacement, in the case of velocity damping and internal damping.

2.2.1. One stage

The equation of motion for an ideal pendulum of length l is³

$$\ddot{x}_1 + \omega_0^2 x_1 = 0 \quad (2.2.1)$$

where

$$\omega_0 = \sqrt{\frac{g}{l}} \quad (2.2.2)$$

and where we indicate the mass position with x_1 . In the case of a movement of the suspension point (whose coordinate is denoted by x_0) it is easy to see that the equation of motion is now

$$\ddot{x}_1 + \omega_0^2(x_1 - x_0) = 0. \quad (2.2.3)$$

Moving to the Fourier domain⁴

$$-\omega^2 \tilde{x}_1 + \omega_0^2(\tilde{x}_1 - \tilde{x}_0) = 0 \quad (2.2.4)$$

and introducing the transfer function

$$\text{TF} \equiv \left| \frac{\tilde{x}_1}{\tilde{x}_0} \right| \quad (2.2.5)$$

³We will confine ourselves to the *small angle approximation*.

⁴To be general, a phase between \tilde{x}_1 and \tilde{x}_0 should appear. However here we are interested only in the modulus of the transfer function which does not depend on any phase. Moreover, pendulum transfer functions will be multiplied with a noise term (seismic) whose phase is not observable.

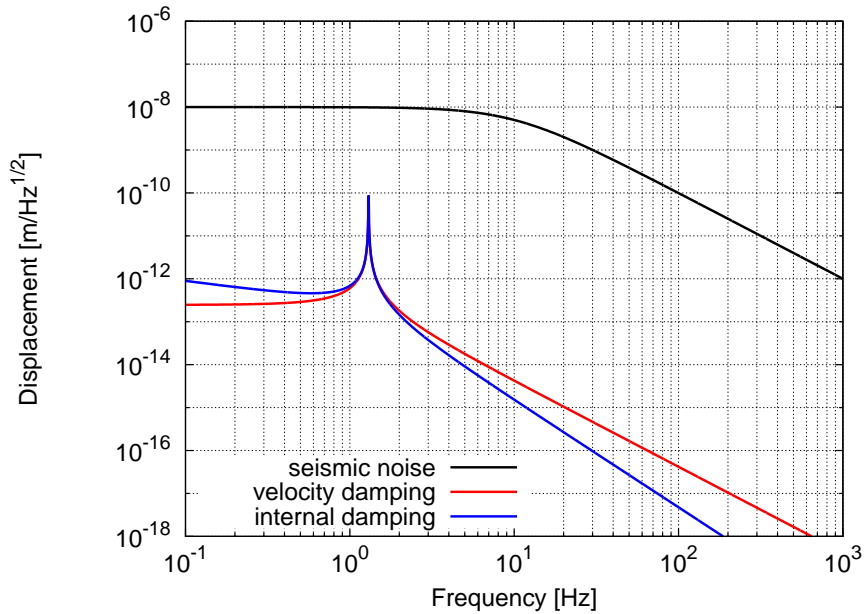


Figure 2.2.: A Typical (fitted) seismic noise is shown in black. The off-resonant thermal noise, our sensitivity goal, is also shown.

we obtain

$$\text{TF} = \left| \frac{1}{1 - \frac{\omega^2}{\omega_0^2}} \right|. \quad (2.2.6)$$

The transfer function is a measure of the “output” movement of the system normalized to the “input” movement. In Figure 2.4 we can show a typical pendulum transfer function: above its resonance frequency a pendulum provides isolation. Note that TF depends on the resonance frequency: the lower it is, the better. Nevertheless since the resonance frequency depends on the pendulum length through a square root, it is practically impossible to obtain resonance frequencies lower than 1 Hz. (Note that the pendulum needs to be put into a vacuum system and vacuum tanks of 10 m or more are just not practical.) Since one pendulum stage does not provide enough seismic noise isolation, we will study multiple-stage pendulum systems built by connecting identical stages together. The various stages will be identical to one another to achieve a good coupling between them, and therefore a good overall performance of the whole system.

2.2.2. Two stages

A two stage pendulum (see Figure 2.5) is a well known physical system, however here we study its transfer function, which is not easily found in common textbooks. We begin

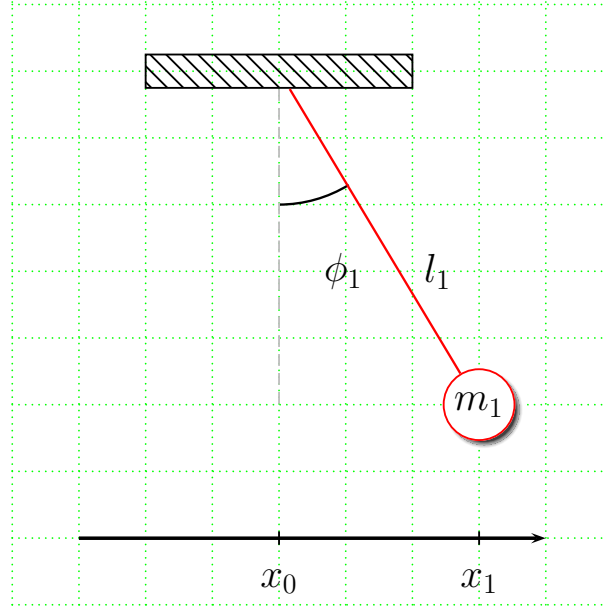


Figure 2.3.: An ideal pendulum (the angle is not to scale, since we limit ourselves to the small angle approximation).

with the system's Lagrangian [8]

$$L^{\text{exact}} = \frac{m_1 + m_2}{2} l_1^2 \dot{\phi}_1^2 + \frac{m_2}{2} l_2^2 \dot{\phi}_2^2 + m_2 l_1 l_2 \dot{\phi}_1 \dot{\phi}_2 \cos(\phi_1 - \phi_2) + (m_1 + m_2) g l_1 \cos \phi_1 + m_2 g l_2 \cos \phi_2. \quad (2.2.7)$$

This Lagrangian, valid for arbitrary angles, leads to very complex and nonlinear equations of motion: in the limit of small angles as is in our case, we can write it as

$$L = \frac{m_1 + m_2}{2} l_1^2 \dot{\phi}_1^2 + \frac{m_2}{2} l_2^2 \dot{\phi}_2^2 + m_2 l_1 l_2 \dot{\phi}_1 \dot{\phi}_2 - \frac{m_1 + m_2}{2} g l_1 \phi_1^2 - \frac{m_2}{2} g l_2 \phi_2^2. \quad (2.2.8)$$

The equations of motion are

$$\begin{aligned} (m_1 + m_2) l_1 \ddot{\phi}_1 + m_2 l_2 \ddot{\phi}_2 + (m_1 + m_2) g \phi_1 &= 0 \\ l_1 \ddot{\phi}_1 + l_2 \ddot{\phi}_2 + g \phi_2 &= 0. \end{aligned} \quad (2.2.9)$$

In order to obtain the transfer function of this system we have to apply a “stimulus” for instance at the top of the suspension and observe the effect on the lower mass. This can be done displacing the angular variable by applying a “translation”: this translation represents the stimulus which we feed into the system⁵:

$$\begin{aligned} \phi_1 &\rightarrow (\phi_1 - \phi_0) \\ \phi_2 &\rightarrow (\phi_2 - \phi_0). \end{aligned} \quad (2.2.10)$$

⁵Another equivalent approach would be to introduce the displacement coordinates $x_1 \equiv l_1 \phi_1$ and $x_2 \equiv l_1 \phi_1 + l_2 \phi_2$, reformulate the equations of motion in terms of the new variable and apply the displacement on the x_i . Both methods lead to the same result.

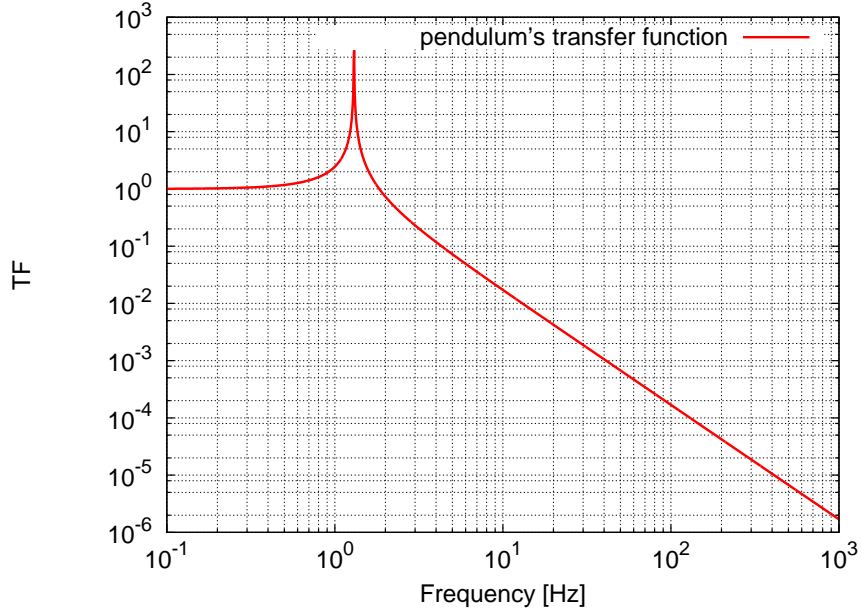


Figure 2.4.: The transfer function of an ideal pendulum: the resonant frequency of 1.3 Hz is close to the value we implemented in the experiment.

The translated equations of motion are (the accelerations remain unaffected by the translation)

$$\begin{aligned} (m_1 + m_2)l_1\ddot{\phi}_1 + m_2l_2\ddot{\phi}_2 + (m_1 + m_2)g(\phi_1 - \phi_0) &= 0 \\ l_1\ddot{\phi}_1 + l_2\ddot{\phi}_2 + g(\phi_2 - \phi_0) &= 0. \end{aligned} \quad (2.2.11)$$

Proceeding as above and introducing the TF now as

$$\text{TF} \equiv \left| \frac{\tilde{\phi}_2}{\tilde{\phi}_0} \right| \quad (2.2.12)$$

we obtain

$$\text{TF} = \left| \frac{1}{\frac{m_1l_1l_2}{(m_1+m_2)g^2}\omega^4 - \frac{(l_1+l_2)}{g}\omega^2 + 1} \right|. \quad (2.2.13)$$

As a simple check, we observe that this transfer function exhibits resonances which coincide with those given by Landau [8]. This observation has important consequences in the following, when we develop an alternative approach to this problem, and the question of where the resonances occur will represent a crucial consistency check.

2.2.3. Three [identical] stages

The triple pendulum (see Figure 2.6) is a straightforward extension of the double pendulum. Nevertheless, since the relevant expressions turn out to be quite cumbersome, we

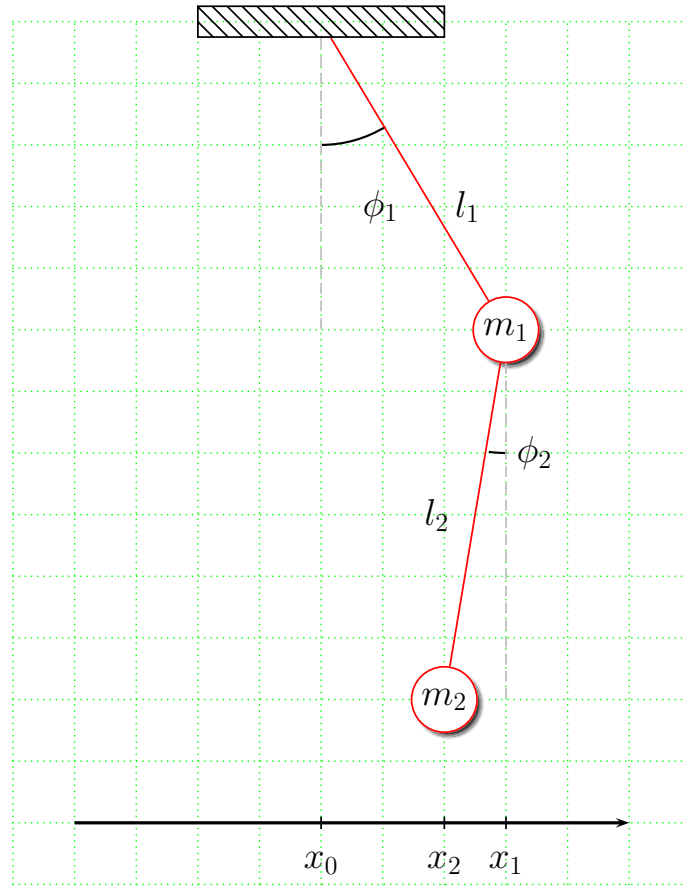


Figure 2.5.: A double pendulum.

will limit ourselves to the particular case in which the three stages are identical. This is also the most important case since identical stages provide good coupling and therefore good overall performance of the system. Given equal masses and pendulum lengths,

$$\begin{aligned} m_1 = m_2 = m_3 &\equiv m \\ l_1 = l_2 = l_3 &\equiv l \end{aligned} \quad (2.2.14)$$

the exact Lagrangian for the system is

$$\begin{aligned} L^{\text{exact}} &= \frac{1}{2}ml^2 \{3\dot{\phi}_1^2 + 2\dot{\phi}_2^2 + \dot{\phi}_3^2\} \\ &+ ml^2 \{2\dot{\phi}_1\dot{\phi}_2 \cos(\phi_1 - \phi_2) + \dot{\phi}_1\dot{\phi}_3 \cos(\phi_1 - \phi_3) + \dot{\phi}_3\dot{\phi}_2 \cos(\phi_3 - \phi_2)\} \\ &+ mgl \{3 \cos \phi_1 + 2 \cos \phi_2 + \cos \phi_3\}. \end{aligned} \quad (2.2.15)$$

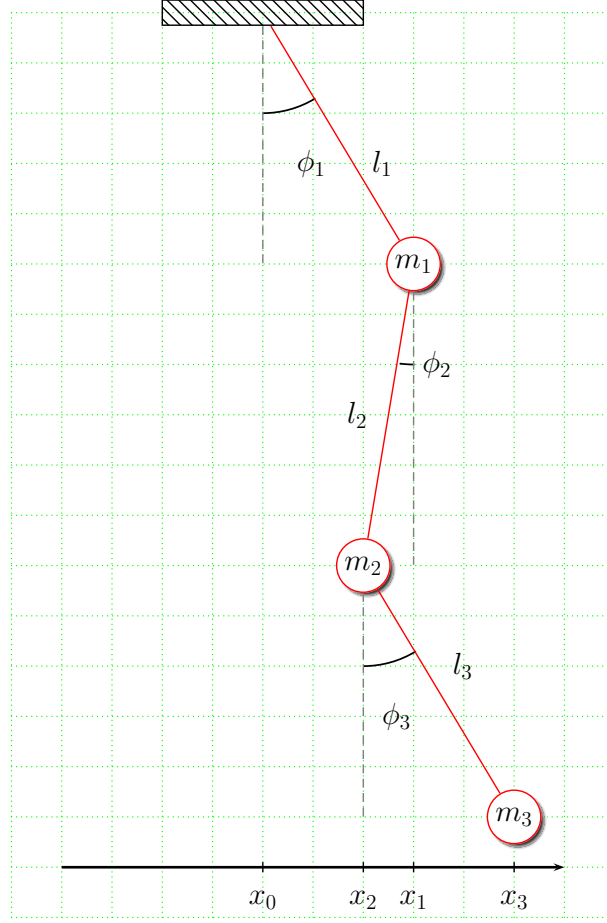


Figure 2.6.: A triple pendulum. We consider the case in which the three stages are identical to one another.

Now, in the small angle approximation we can write

$$L = \frac{1}{2}ml^2 \left\{ 3\dot{\phi}_1^2 + 2\dot{\phi}_2^2 + \dot{\phi}_3^2 + 4\dot{\phi}_1\dot{\phi}_2 + 2\dot{\phi}_1\dot{\phi}_3 + 2\dot{\phi}_2\dot{\phi}_3 \right\} - \frac{mgl}{2} \left\{ 3\phi_1^2 + 2\phi_2^2 + \phi_3^2 \right\}. \quad (2.2.16)$$

The Euler-Lagrange equations are:

$$\begin{aligned} 6\ddot{\phi}_1 + 4\ddot{\phi}_2 + 2\ddot{\phi}_3 + 6\omega_0^2\phi_1 &= 0 \\ 4\ddot{\phi}_1 + 4\ddot{\phi}_2 + 2\ddot{\phi}_3 + 4\omega_0^2\phi_2 &= 0 \\ 2\ddot{\phi}_1 + 2\ddot{\phi}_2 + 2\ddot{\phi}_3 + 2\omega_0^2\phi_3 &= 0 \end{aligned} \quad (2.2.17)$$

where we have introduced

$$\omega_0^2 \equiv \frac{g}{l}. \quad (2.2.18)$$

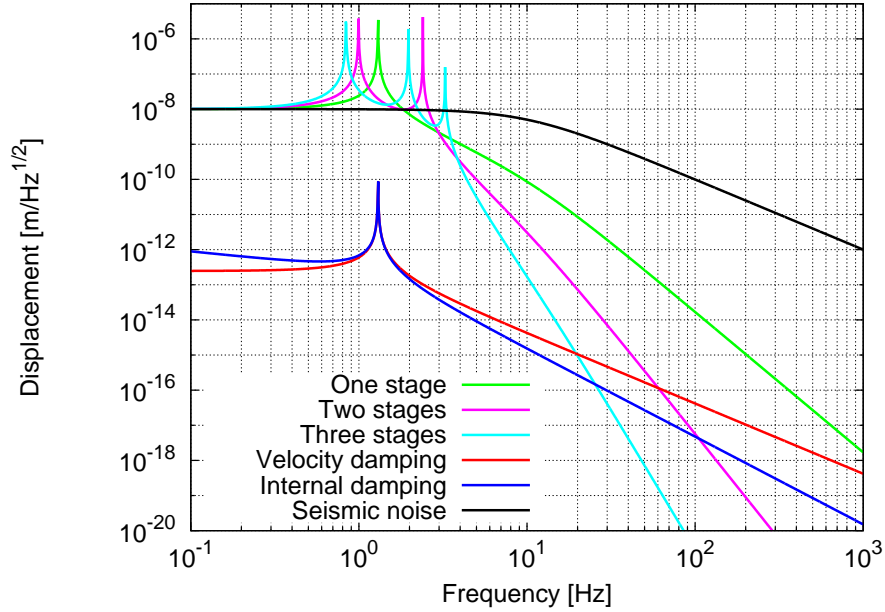


Figure 2.7.: The isolation provided by one, two and three (identical) stages is plotted against the target which is labeled as velocity and internal damping. Three stages provide, *within this approximation*, enough seismic isolation to ensure a detection at 100 Hz.

As in the two previous cases we introduce the “stimulus” in the form of a translation of the Lagrangian coordinate ϕ_i

$$\begin{aligned}\phi_1 &\rightarrow (\phi_1 - \phi_0) \\ \phi_2 &\rightarrow (\phi_2 - \phi_0) \\ \phi_3 &\rightarrow (\phi_3 - \phi_0).\end{aligned}\tag{2.2.19}$$

The Euler-Lagrange equations now read:

$$\begin{aligned}6\ddot{\phi}_1 + 4\ddot{\phi}_2 + 2\ddot{\phi}_3 + 6\omega_0^2(\phi_1 - \phi_0) &= 0 \\ 4\ddot{\phi}_1 + 4\ddot{\phi}_2 + 2\ddot{\phi}_3 + 4\omega_0^2(\phi_2 - \phi_0) &= 0 \\ 2\ddot{\phi}_1 + 2\ddot{\phi}_2 + 2\ddot{\phi}_3 + 2\omega_0^2(\phi_3 - \phi_0) &= 0\end{aligned}\tag{2.2.20}$$

Fourier transforming this system of differential equations, we obtain a system of algebraic equations. Eliminating $\tilde{\phi}_1$ and $\tilde{\phi}_2$ we finally find the system’s transfer function:

$$\text{TF} \equiv \left| \frac{\tilde{\phi}_3}{\tilde{\phi}_0} \right| = \left| \frac{6\omega_0^6}{\omega^6 - 9\omega_0^2\omega^4 + 18\omega_0^4\omega^2 - 6\omega_0^6} \right|.\tag{2.2.21}$$

We can see in Figure 2.7 that a pendulum isolation chain with three stages could *in principle* provide the required isolation from seismic noise. We decided to build a

system with three pendulum stages, considering the resulting isolation good enough for our purposes. We note, on a practical level, that the isolation chain shows very sharp resonances at low frequency, which will need proper damping.

2.3. The experimental setup

The experiment itself has already been discussed in Volker Leonhardt's PhD thesis [9], here we provide a quick description of the setup, since we want to discuss mainly the simulations and the theoretical work we did regarding the isolation from seismic noise. The experiment can be summarized as follows:

- **Goal:** Measure the off-resonant thermal noise in a suspended pendulum, addressing the theoretical issue raised by Saulson [1].
- **Target sensitivity:** In order to reach the goal, a measurement above resonance is required. A sensitivity of 10^{-17} m/ $\sqrt{\text{Hz}}$ at 100 Hz was planned.
- **Measuring device:** A suspended resonator as the last stage of a complex pendulum suspension chain.
- **Measuring technique:** We locked the suspended resonator to a frequency stabilized laser. The feedback signal of the lock is then directly related to the relative motion of the resonator, by a frequency-dependent calibration factor.
- **Actuator:** In order to lock the resonator frequency to the laser frequency we used a system of coils and magnets as actuator. The coils are provided with shadow sensors and locking loop keeps the movement of the magnet inside the coil to a minimum at the resonances of the suspension. The magnets are attached to one of the two resonator masses, the coils must also be suspended in order not to feed seismic noise into the system.
- **Laser:** The laser that we used to lock the resonator had to be frequency stabilized to a rigid high-finesse resonator (kept in a small vacuum tank), by means of the standard Pound-Drever-Hall technique.
- **Seismic isolation:** Great care was taken in providing as much seismic isolation as possible, since we knew that this noise source could spoil the sensitivity. This problem turned out to be even more severe than expected and will be discussed in the following chapter.
- **Technicalities:** Among the technical details we mention:
 - The pendulum suspension was installed in a vacuum tank to provide isolation from damping caused by the air.
 - The frequency locking mechanism, relying on a system of coil and magnet actuators, was also suspended to avoid feeding seismic noise through the locking scheme.

- The sharp resonances at low frequency, resulting from the multiple stage pendulum suspension itself, needed a damping scheme also provided by a set of coils and magnets.

2.4. The noise floor

After setting up the experiment we were able to routinely take data. Since the sensitivity did not match our expectations we went into an intense noise-hunting phase.

A list of the noise sources we investigated includes:

- **Seismic shortcut through wires:** we replaced the wires going inside the tank carrying control signals with thinner ones.
- **Autoalignment:** we developed and installed an auto-alignment system to ensure a better light-coupling into the resonator.
- **Higher finesse:** we replaced the resonator with another with higher finesse, hence narrower bandwidth, in order to have bigger signals.
- **Quiet operation:** we operated the experiment late at night, to avoid seismic noise through human activities (the so-called anthropogenic noise).
- **Control electronics:** We optimized the electronics in order to lower electronic noise.
- **Additional isolation stage:** we added an extra isolation stage in the chain, to gain more isolation from seismic noise.
- **Lower Q :** we built a low Q pendulum, to increase the thermal noise signal with respect to the technical noise.

During this noise hunting the sensitivity level remained remarkably constant (in Figure 2.8 we show a result of a typical measurement), so we decided to take another approach, focusing again on a noise source known from the beginning: seismic noise.

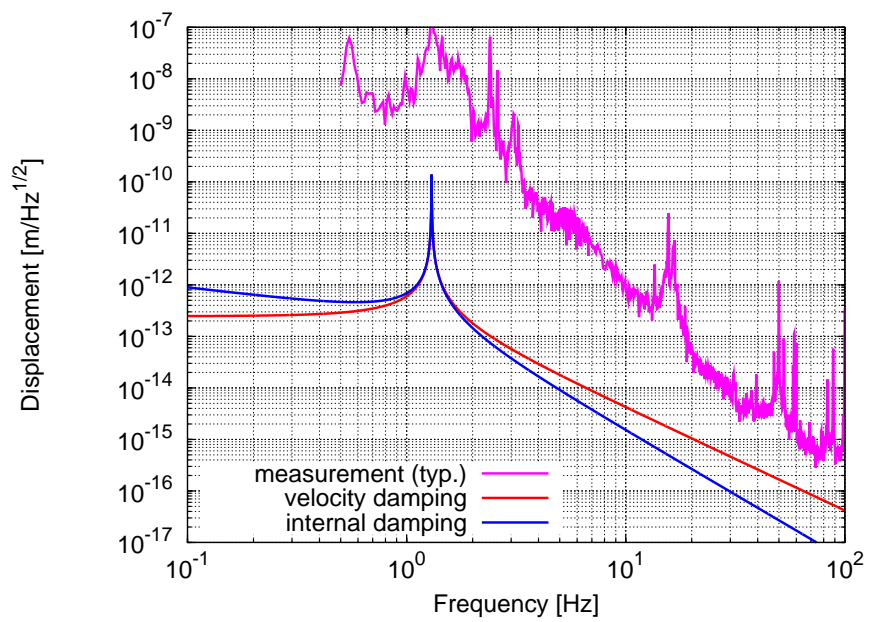


Figure 2.8.: The typical sensitivity of our setup: lots of possible noise sources were addressed but the sensitivity stayed remarkably constant. For comparison also the off-resonant thermal noise goal is shown.

3. Optimization of the pendulum suspension

3.1. Seismic noise still leaking into the system

The difficulties to lower the noise floor in our experiment led us to a deeper investigation of our system. The broad resonances in the spectrum and its atypical slope, gave us reason to think about the seismic isolation again. We made the following hypothesis:

The seismic isolation was not good enough, seismic noise was still leaking into the system. Since this hypothesis is not compatible with the simple pendulum model we developed in the previous chapter, we decided to analyze the behaviour of the pendulum suspension system with respect to all degrees of freedom, namely with respect to movement of the pendulum masses in their six degrees of freedom. This problem, at the core of the technology of gravitational wave detectors, is not yet fully understood, so we proceeded in a twofold way, carrying out investigations in the lab and at the same time, theoretical studies. To be more specific:

- We altered the pendulum suspension, within the constraints of the existing experimental setup.
- We started to develop new theoretical models capable of explaining the experimental data and to make useful predictions.

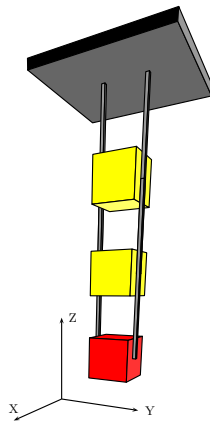


Figure 3.1.: Schematic representation of the pendulum suspension. The movement of each mass has to be analyzed in its six degrees of freedom. The pendulum suspension is designed to minimize the seismic movement of the lowest pendulum stage (here the red one).

As already mentioned, the simple pendulum model turned out to be misleading when applied to our setup, which looked similar to that shown in Figure 3.1. Each mass has

3. Optimization of the pendulum suspension

six degrees of freedom: three displacements along the x, y, z axis and three rotations around the same axis. It must additionally be noted that a length measurement is always relative to a reference point and because of the presence of seismic noise we cannot take any reference in direct contact to the ground. So we built *a pair* of pendulum suspensions and then measured the relative motion of the lowest pendulum stages (see Figure 3.2). In the experiment one pendulum suspension was much heavier and bigger than the other, thereby providing the reference point for the length measurement. The experimental setup is described in Volker Leonhardt's PhD thesis [9].

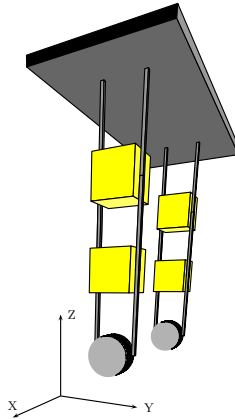


Figure 3.2.: In order to measure the off-resonant thermal noise, a pair of pendulum suspensions were needed. Moreover, the last stage of each pendulum is a mirror: in this way we can optically measure the relative length noise.

The length measurement was performed optically, suspending two mirrors as the last stage, i.e. a resonator, which reacts to length changes by varying its reflection and transmission.

3.2. Enhancement of the moments of inertia

To reduce the vibration of the pendulum suspension caused by seismic noise, we enhanced the moments of inertia of the lowest two pendulum stages. This step was achieved by attaching small wings to the two lowest stages in the pendulum suspensions, as shown in Figure 3.3 which is a photo of the modified last pendulum stage. Such a modification was

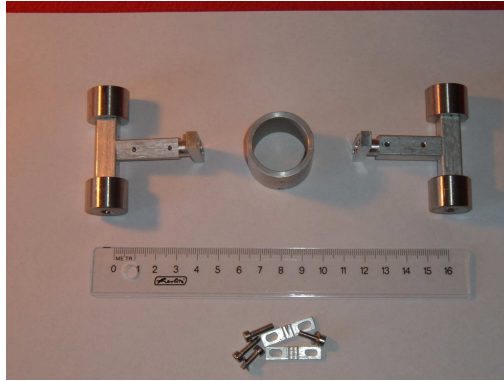


Figure 3.3.: Photo of the last pendulum stage. The hollow cylinder in the center hosted a standard 1 inch optical mirror. The two additional wings increased the overall moment of inertia, thereby reducing the resonance frequencies of the system.

not planned for in the original experimental setup, and this caused some technical difficulties in putting this new stage into place. Nevertheless we were able to overcome these problems and take data, which are shown in Figure 3.4. The improvement with respect to the setup without wings is clearly visible and was *the best result* we could achieve after addressing *many* other possible noise sources (see Volker Leonhardt’s PhD thesis [9]). In order to better understand these data, we also started a theoretical investigation of the whole pendulum suspension, by extending the simple model with one degree of freedom per stage, to a much more complex one, in which each pendulum stage has six degrees of freedom.

3.3. Input-output formalism: Holzer’s method

We used an input-output formalism originally developed by Holzer [10] and recently re-discovered by G. Cella [11] to model the suspension chains in GW detectors. A clear introduction to the method can be found in [12]. A very interesting book by Prof. Pestel [13] also describes this method, albeit from an engineering standpoint. By using this method one avoids complicated analytical expressions for the dynamics of the system: explicit expressions for the time evolution of the single degree of freedom are neither required nor obtained. Rather, each building block of the suspension chain can be modeled as a matrix connecting one input to one output, in the Fourier domain. In principle there are no limits to the complexity that can be achieved. In practice, since the method is a numerical one, great care has to be taken in order to avoid numerical instabilities. In

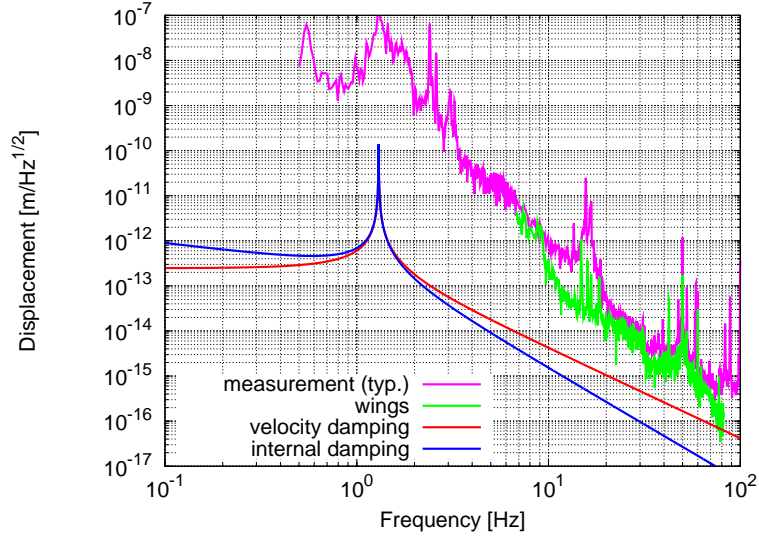


Figure 3.4.: The addition of the small wings resulted in a clear lowering of the measured length noise. The thermal noise curves shown here are calculated for the mass without wings.

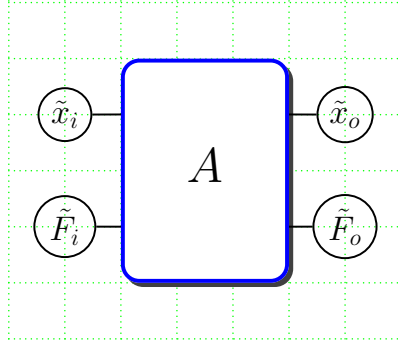


Figure 3.5.: Schematic representation of a system in the input-output formalism.

Holzer's method a system is described by its dynamical variable \tilde{x} , and by the force exerted by the system on its boundary \tilde{F} , in the Fourier domain. Each mechanical element can be modeled by a connecting element between an input pair \tilde{x}_i, \tilde{F}_i and an output one \tilde{x}_o, \tilde{F}_o . We are describing a matrix formalism which takes the form

$$\begin{pmatrix} \tilde{x}_o \\ \tilde{F}_o \end{pmatrix} = \begin{pmatrix} a_{11} & a_{12} \\ a_{21} & a_{22} \end{pmatrix} \begin{pmatrix} \tilde{x}_i \\ \tilde{F}_i \end{pmatrix} \equiv A \begin{pmatrix} \tilde{x}_i \\ \tilde{F}_i \end{pmatrix}. \quad (3.3.1)$$

If two elements are connected in series, that is if the output from one element is the input of the next one, then we can express this in our matrix formalism by ordinary matrix multiplication, i.e. given

$$\begin{pmatrix} \tilde{x}_t \\ \tilde{F}_t \end{pmatrix} = A_1 \begin{pmatrix} \tilde{x}_i \\ \tilde{F}_i \end{pmatrix} \quad (3.3.2)$$

$$\begin{pmatrix} \tilde{x}_o \\ \tilde{F}_o \end{pmatrix} = A_2 \begin{pmatrix} \tilde{x}_t \\ \tilde{F}_t \end{pmatrix} \quad (3.3.3)$$

then

$$\begin{pmatrix} \tilde{x}_o \\ \tilde{F}_o \end{pmatrix} = A_2 A_1 \begin{pmatrix} \tilde{x}_i \\ \tilde{F}_i \end{pmatrix}. \quad (3.3.4)$$

The matrix multiplication is not commutative, so the order in which the matrices appear

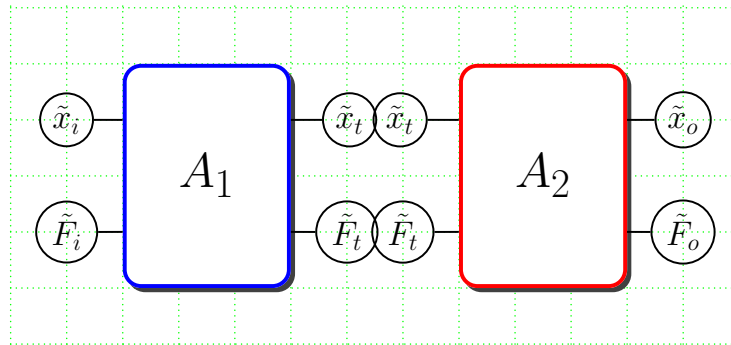


Figure 3.6.: Serial connection of two systems.

does matter.

3.3.1. A simple mass

The Holzer's matrix for a point-like mass m is

$$A(m) \equiv \begin{pmatrix} 1 & 0 \\ m\omega^2 & 1 \end{pmatrix}. \quad (3.3.5)$$

3.3.2. An ideal spring

For an ideal spring with spring constant k we have

$$B(k) \equiv \begin{pmatrix} 1 & -\frac{1}{k} \\ 0 & 1 \end{pmatrix}. \quad (3.3.6)$$

3.4. Consistency checks

Here we give a number of consistency checks in order to show that the method actually works. Moreover, this will enable us to get acquainted with the new tools, and will help in the needed generalization from the first example to a working simulation of a pendulum suspension.

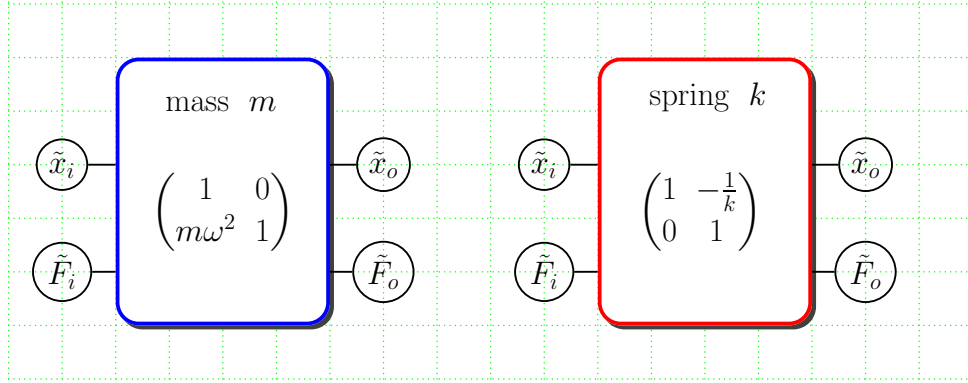


Figure 3.7.: A schematic representation of the two basic elements, in the matrix formalism: a mass and a spring.

3.4.1. Two masses, two springs

We connect two masses m_1 and m_2 in series: we obtain

$$\begin{aligned} A(m_1) \cdot A(m_2) &= \begin{pmatrix} 1 & 0 \\ m_1\omega^2 & 1 \end{pmatrix} \begin{pmatrix} 1 & 0 \\ m_2\omega^2 & 1 \end{pmatrix} \\ &= \begin{pmatrix} 1 & 0 \\ (m_1 + m_2)\omega^2 & 1 \end{pmatrix} = A(m_1 + m_2) = A(m_2) \cdot A(m_1) \end{aligned} \quad (3.4.1)$$

that is the mass is additive and “commutative” as it should be. We can also connect two springs with constants k_1 and k_2 in series:

$$\begin{aligned} B(k_1) \cdot B(k_2) &= \begin{pmatrix} 1 & -\frac{1}{k_1} \\ 0 & 1 \end{pmatrix} \begin{pmatrix} 1 & -\frac{1}{k_2} \\ 0 & 1 \end{pmatrix} \\ &= \begin{pmatrix} 1 & -\left(\frac{1}{k_1} + \frac{1}{k_2}\right) \\ 0 & 1 \end{pmatrix} = B\left(\frac{k_1 k_2}{k_1 + k_2}\right) = B(k_2) \cdot B(k_1) \end{aligned} \quad (3.4.2)$$

also a known result. We observe that in all the examples so far the matrices have a determinant equal to 1.

3.4.2. A spring-mass system: TF

Now we can connect a spring and a mass together (see Figure 3.8).

$$M(m, k) \equiv A(m) \cdot B(k) = \begin{pmatrix} 1 & 0 \\ m\omega^2 & 1 \end{pmatrix} \begin{pmatrix} 1 & -\frac{1}{k} \\ 0 & 1 \end{pmatrix} = \begin{pmatrix} 1 & -\frac{1}{k} \\ m\omega^2 & 1 - \frac{m\omega^2}{k} \end{pmatrix}. \quad (3.4.3)$$

The input-output relation for this system (in the frequency domain) is simply

$$\begin{pmatrix} \tilde{x}_o \\ \tilde{F}_o \end{pmatrix} = M(m, k) \begin{pmatrix} \tilde{x}_i \\ \tilde{F}_i \end{pmatrix}. \quad (3.4.4)$$

The TF is computed by setting the appropriate boundary conditions:

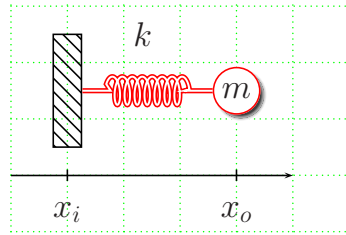


Figure 3.8.: A spring-mass system.

- $\tilde{F}_o = 0$ i.e. we leave the output open.

Then by eliminating \tilde{F}_i we obtain

$$\text{TF} = \left| \frac{\tilde{x}_o}{\tilde{x}_i} \right| = \left| \left(1 - \frac{m\omega^2}{k} \right)^{-1} \right| \equiv \left| \frac{1}{1 - \frac{\omega^2}{\omega_0^2}} \right| \quad (3.4.5)$$

where

$$\omega_0^2 \equiv \frac{k}{m}. \quad (3.4.6)$$

Needless to say, this is the expected transfer function for a mass-spring system. In general, we observe that, given a matrix A , the TF is

$$\text{TF} = \left| \frac{\det(A)}{a_{22}} \right|. \quad (3.4.7)$$

3.5. Two, three harmonic oscillators connected in series

Let's consider systems composed by two and three spring-mass subsystems connected in series¹. We will study these systems with respect to their input-output behaviour by using the usual Lagrangian method and the new matrix formalism.

3.5.1. Lagrangian formalism for a 2-stage-system

The Lagrangian of the system shown in Figure 3.9 is

$$L = K - U = \frac{1}{2} [m_1\dot{x}_1^2 + m_2\dot{x}_2^2 + k_1x_1^2 + k_2(x_1 - x_2)^2] \quad (3.5.1)$$

and the equations of motion are

$$\begin{aligned} m_1\ddot{x}_1 + k_1x_1 + k_2(x_1 - x_2) &= 0 \\ m_2\ddot{x}_2 - k_2(x_1 - x_2) &= 0. \end{aligned} \quad (3.5.2)$$

¹As a matter of fact, we lack a formal proof that the matrix method is indeed correct. We show therefore a number of interesting examples, including the ones we will employ later, to claim that *for our purposes* the method behaves correctly.

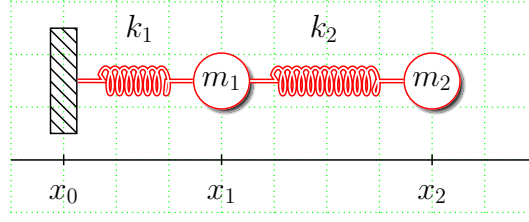


Figure 3.9.: A 2-stage-system.

Introducing the stimulus by displacing the coordinates by x_0 we then have

$$\begin{aligned} m_1 \ddot{x}_1 + k_1(x_1 - x_0) + k_2(x_1 - x_2 + x_0 - x_0) &= 0 \\ m_2 \ddot{x}_2 - k_2(x_1 - x_2 + x_0 - x_0) &= 0. \end{aligned} \quad (3.5.3)$$

Taking the Fourier transform and eliminating \tilde{x}_1 we obtain:

$$\text{TF} \equiv \left| \frac{\tilde{x}_2}{\tilde{x}_0} \right| = \left| \frac{1}{\frac{1}{k_1 k_2} m_1 m_2 \omega^4 - \frac{1}{k_1} (m_1 + m_2) \omega^2 - \frac{1}{k_2} m_2 \omega^2 + 1} \right|. \quad (3.5.4)$$

3.5.2. Matrix formalism for a 2-stage-system

In this matrix formalism, the matrix T representing the whole system (see Figure 3.9) is

$$T \equiv M(k_2, m_2) \cdot M(k_1, m_1) = \begin{pmatrix} 1 & -\frac{1}{k_2} \\ m_2 \omega^2 & 1 - \frac{m_2 \omega^2}{k_2} \end{pmatrix} \cdot \begin{pmatrix} 1 & -\frac{1}{k_1} \\ m_1 \omega^2 & 1 - \frac{m_1 \omega^2}{k_1} \end{pmatrix}. \quad (3.5.5)$$

By using the equation (3.4.7) we get

$$\text{TF} = |T_{22}^{-1}| = \left| \frac{1}{\left(1 - \frac{m_2 \omega^2}{k_2}\right) \left(1 - \frac{m_1 \omega^2}{k_1}\right) - \frac{m_1 \omega^2}{k_1}} \right|. \quad (3.5.6)$$

We can see by direct inspection that the two methods agree, as expected.

3.5.3. Lagrangian formalism for 3 [identical] stages

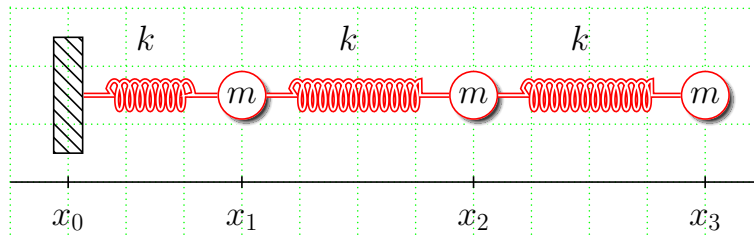


Figure 3.10.: Three identical stages.

The Lagrangian is a straightforward generalization of the previous one (see Figure 3.10)

$$L = K - U = \frac{1}{2} [m\dot{x}_1^2 + m\dot{x}_2^2 + m\dot{x}_3^2 + kx_1^2 + k(x_2 - x_1)^2 + k(x_3 - x_2)^2]. \quad (3.5.7)$$

The equation of motions are

$$\begin{aligned} m\ddot{x}_1 + k(2x_1 - x_2) &= 0 \\ m\ddot{x}_2 + k(2x_2 - x_1 - x_3) &= 0 \\ m\ddot{x}_3 + k(x_3 - x_2) &= 0 \end{aligned} \quad (3.5.8)$$

By following the same procedure as in the 2-stage case we get

$$\text{TF} = \left| \frac{\tilde{x}_3}{\tilde{x}_0} \right| = \left| \frac{1}{\left(\frac{\omega}{\omega_0}\right)^6 - 5\left(\frac{\omega}{\omega_0}\right)^4 + 6\left(\frac{\omega}{\omega_0}\right)^2 - 1} \right| \quad (3.5.9)$$

where

$$\omega_0 \equiv \sqrt{\frac{k}{m}}. \quad (3.5.10)$$

3.5.4. Matrix formalism for 3 [identical] stages

In this case

$$\begin{aligned} T &\equiv M(k, m) \cdot M(k, m) \cdot M(k, m) \\ &= \begin{pmatrix} 1 & -\frac{1}{k} \\ m\omega^2 & 1 - \frac{m\omega^2}{k} \end{pmatrix} \cdot \begin{pmatrix} 1 & -\frac{1}{k} \\ m\omega^2 & 1 - \frac{m\omega^2}{k} \end{pmatrix} \cdot \begin{pmatrix} 1 & -\frac{1}{k} \\ m\omega^2 & 1 - \frac{m\omega^2}{k} \end{pmatrix}. \end{aligned} \quad (3.5.11)$$

The transfer function is

$$\text{TF} = |T_{22}^{-1}| = \left| \frac{1}{\left(\frac{\omega}{\omega_0}\right)^6 - 5\left(\frac{\omega}{\omega_0}\right)^4 + 6\left(\frac{\omega}{\omega_0}\right)^2 - 1} \right| \quad (3.5.12)$$

as expected.

Figure 3.11 shows a comparison of the transfer functions computed by the two methods: the matrix method (solid lines) versus solution of the Newton equation (dotted lines). By using the matrix approach we can stack as many stages as we need, and let a computer, *via a suitable numerical algorithm*, compute the resulting transfer function.

3.6. Harmonic oscillator [spring-mass system] vs. pendulum

We address here a subtle issue: namely the comparison between a harmonic oscillator and a pendulum having the same resonant angular frequency ω_0 . As long as we study *one-stage* systems a pendulum and a spring-mass system behave the same way: this is well known from undergraduate physics. This is *no longer* true when we start adding

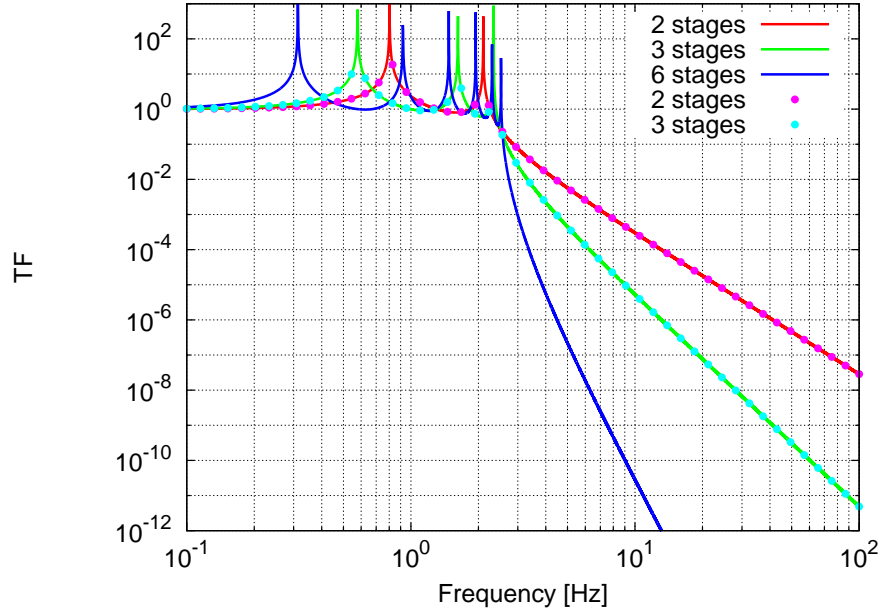


Figure 3.11.: Plot of the transfer function of systems composed by a series connection of an increasing number of identical spring and mass subsystems: the matrix method (solid lines) agrees with the direct method of solving the equations of motion (filled circles). Moreover, the former enables us to obtain TFs (here a system with six stages) that would be difficult to obtain with the latter.

more stages. We have already calculated all the quantities needed to make this issue clear. The transfer function for a double pendulum (with identical stages) is

$$\text{TF}_{\text{pendulum}}^{(2)} = \left| \frac{1}{\frac{1}{2} \frac{\omega^4}{\omega_0^4} - 2 \frac{\omega^2}{\omega_0^2} + 1} \right| \quad (3.6.1)$$

while the transfer function for a 2-stage spring and mass system is

$$\text{TF}_{\text{spring+mass}}^{(2)} = \left| \frac{1}{\frac{\omega^4}{\omega_0^4} - 3 \frac{\omega^2}{\omega_0^2} + 1} \right|. \quad (3.6.2)$$

In Figure 3.12 we show these two transfer functions. This means a simple pendulum *cannot* be modeled by the same matrix as for a spring and mass. So, we need to take a step back and find a matrix that models a pendulum and that reproduces the pendulum transfer function we already derived, for single- and multiple-stage systems.

3.7. The matrix for a pendulum

The task of finding an appropriate matrix for a pendulum is not an easy one. The reason lies in the method itself, which does not use Newton's equation, rather a black-

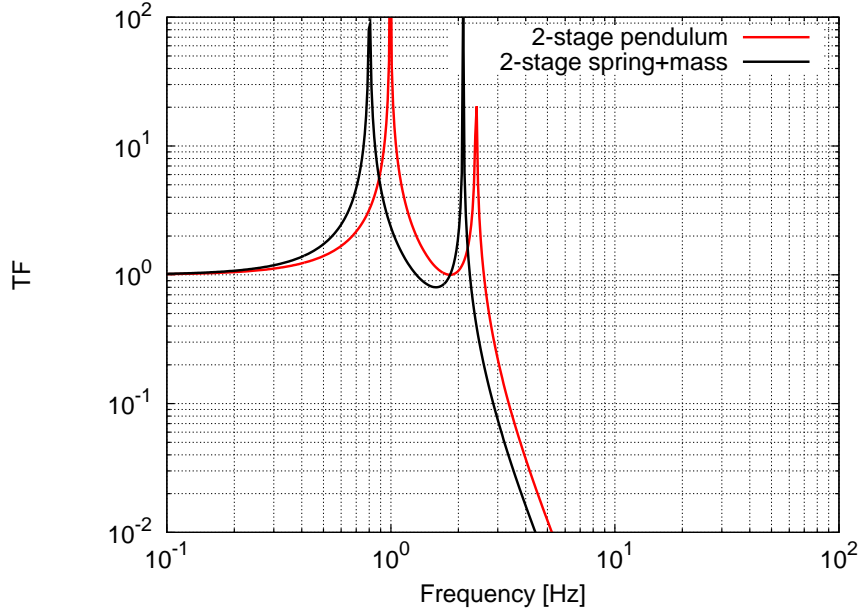


Figure 3.12.: Plot of the transfer functions of two *similar albeit not equivalent* systems: a 2-stage pendulum and a 2-stage spring and mass system.

box approach in which the building blocks (the matrices) are, more or less, taken as given. Consider again the algebraic equation (in Fourier space) governing an oscillator (spring and mass system) or a pendulum stage as well

$$-m\omega^2\tilde{x} + m\omega_0^2(\tilde{x} - \tilde{x}_0) = 0. \quad (3.7.1)$$

We observe that in a double pendulum, for example, the upper mass is subjected to a bigger restoring force since the tension of the upper connecting wire is proportional to the *sum* of the two masses. Therefore we introduce a modified restoring term, through

$$k \equiv m\omega_0^2 \rightarrow m^*\omega_0^2 \quad (3.7.2)$$

where m^* represents the sum of the masses from the bottom to the stage in consideration.

In this way we give up one the feature of the method: namely the possibility to describe each subsystem as a black-box. Nevertheless, since the parameters representing the whole system (here the pendulum chain) are always known, the drawback of describing a stage (a subsystem) by using information belonging to others ones is a minor drawback. This modification enables us to reproduce the already known transfer function for a multiple pendulum which we obtained by solving the Euler-Lagrange equation of the system.

3.7.1. A double pendulum in the matrix formalism

As we suggested, each of the two stages can be modeled by the matrix

$$P(m_i, m_i^*, \omega_i) \equiv \begin{pmatrix} 1 & -\frac{1}{m_i^*\omega_i^2} \\ m_i\omega^2 & 1 - \frac{m_i\omega^2}{m_i^*\omega_i^2} \end{pmatrix} \quad (3.7.3)$$

where $i = 1, 2$. Now for the lower stage ($i = 2$) we have simply

$$m_2^* = m_2 \quad (3.7.4)$$

while for the upper one ($i = 1$)

$$m_1^* = m_1 + m_2. \quad (3.7.5)$$

It follows that the double pendulum can be described by the matrix T

$$\begin{aligned} T &= P(m_2, m_2^*, \omega_2) \cdot P(m_1, m_1^*, \omega_1) \\ &= \begin{pmatrix} 1 & -\frac{1}{m_2^* \omega_2^2} \\ m_2 \omega^2 & 1 - \frac{m_2 \omega^2}{m_2^* \omega_2^2} \end{pmatrix} \cdot \begin{pmatrix} 1 & -\frac{1}{m_1^* \omega_1^2} \\ m_1 \omega^2 & 1 - \frac{m_1 \omega^2}{m_1^* \omega_1^2} \end{pmatrix} \\ &= \begin{pmatrix} 1 & -\frac{1}{m_2 \omega_2^2} \\ m_2 \omega^2 & 1 - \frac{\omega^2}{\omega_2^2} \end{pmatrix} \cdot \begin{pmatrix} 1 & -\frac{1}{(m_1+m_2) \omega_1^2} \\ m_1 \omega^2 & 1 - \frac{m_1 \omega^2}{(m_1+m_2) \omega_1^2} \end{pmatrix}. \end{aligned} \quad (3.7.6)$$

Since the single matrices have determinant equal to 1, the TF is

$$\text{TF} = |T_{22}^{-1}| = \left| \frac{1}{\frac{m_1 l_1 l_2}{(m_1+m_2)g^2} \omega^4 - \frac{l_1+l_2}{g} \omega^2 + 1} \right| \quad (3.7.7)$$

in agreement with Equation (2.2.13).

3.7.2. A triple pendulum in the matrix formalism [identical stages]

Adding one more stage means that the matrix T is the product of three matrices representing the single subsystems. Taking these subsystems to be identical we can write:

$$\begin{aligned} T &= P(m_3, m_3^*, \omega_0) \cdot P(m_2, m_2^*, \omega_0) \cdot P(m_1, m_1^*, \omega_0) \\ &= \begin{pmatrix} 1 & -\frac{1}{m \omega_0^2} \\ m \omega^2 & 1 - \frac{\omega^2}{\omega_0^2} \end{pmatrix} \cdot \begin{pmatrix} 1 & -\frac{1}{2m \omega_0^2} \\ m \omega^2 & 1 - \frac{\omega^2}{2\omega_0^2} \end{pmatrix} \cdot \begin{pmatrix} 1 & -\frac{1}{3m \omega_0^2} \\ m \omega^2 & 1 - \frac{\omega^2}{3\omega_0^2} \end{pmatrix} \equiv \begin{pmatrix} t_{11} & t_{12} \\ t_{21} & t_{22} \end{pmatrix}. \end{aligned} \quad (3.7.8)$$

The transfer function is

$$\text{TF} = \left| \frac{1}{t_{22}} \right| = \left| \frac{6}{-\alpha^6 + 9\alpha^4 - 18\alpha^2 + 6} \right| \quad (3.7.9)$$

where

$$\alpha \equiv \frac{\omega}{\omega_0}. \quad (3.7.10)$$

This is also consistent with our previous result.

3.8. Generalization to complex systems: Newton's equations method

In the case of a system composed by one stage with two mutually coupled degrees of freedom, we can write the equations of motion as

$$\begin{aligned} m_1 \ddot{x}_1 &= -k_{11} x_1 - k_{12} x_2 \\ m_2 \ddot{x}_2 &= -k_{21} x_1 - k_{22} x_2. \end{aligned} \quad (3.8.1)$$

If we introduce the notation

$$q^o \equiv \begin{pmatrix} x_1 \\ x_2 \end{pmatrix} \quad (3.8.2)$$

$$\mathbb{M} \equiv \begin{pmatrix} m_1 & 0 \\ 0 & m_2 \end{pmatrix} \quad (3.8.3)$$

$$\mathbb{K} \equiv \begin{pmatrix} k_{11} & k_{12} \\ k_{21} & k_{22} \end{pmatrix} \quad (3.8.4)$$

we can write

$$\mathbb{M}\ddot{q} = -\mathbb{K}q. \quad (3.8.5)$$

Then, as previously, we displace the coordinate

$$q^o \rightarrow q^o - q^i \quad (3.8.6)$$

and move to the Fourier domain

$$-\omega^2 \mathbb{M} \tilde{q}^o = -\mathbb{K}(\tilde{q}^o - \tilde{q}^i) \quad (3.8.7)$$

we get finally

$$\tilde{q}^o = [\mathbb{K} - \omega^2 \mathbb{M}]^{-1} \mathbb{K} \tilde{q}^i \quad (3.8.8)$$

this Equation generalize the spring-mass system in the case when the system has more than one degree of freedom.

3.9. Two degrees of freedom: input-output method

In the framework of the input-output method, the generalization to coupled (sub)-systems can be expressed by the following system of equations

$$\begin{pmatrix} \tilde{q}^o \\ \tilde{F}^o \end{pmatrix} = T \begin{pmatrix} \tilde{q}^i \\ \tilde{F}^i \end{pmatrix} \quad (3.9.1)$$

where the \tilde{q}^i , \tilde{F}^i are 2-component vectors and T is a 4×4 matrix. Carrying on the analogy with a spring-mass system, we write:

$$T = \begin{pmatrix} \mathbb{1} & -\mathbb{K}^{-1} \\ \omega^2 \mathbb{M} & \mathbb{1} - \omega^2 \mathbb{M} \mathbb{K}^{-1} \end{pmatrix}. \quad (3.9.2)$$

We let the output be free; that is we let

$$\tilde{F}^o = \begin{pmatrix} 0 \\ 0 \end{pmatrix} \quad (3.9.3)$$

so that the equations reads

$$\begin{aligned} \tilde{q}^o &= \mathbb{1} \tilde{q}^i - \mathbb{K}^{-1} \tilde{F}^i \\ \tilde{F}^o &= \begin{pmatrix} 0 \\ 0 \end{pmatrix} = \omega^2 \mathbb{M} \tilde{q}^i + (\mathbb{1} - \omega^2 \mathbb{M} \mathbb{K}^{-1}) \tilde{F}^i. \end{aligned} \quad (3.9.4)$$

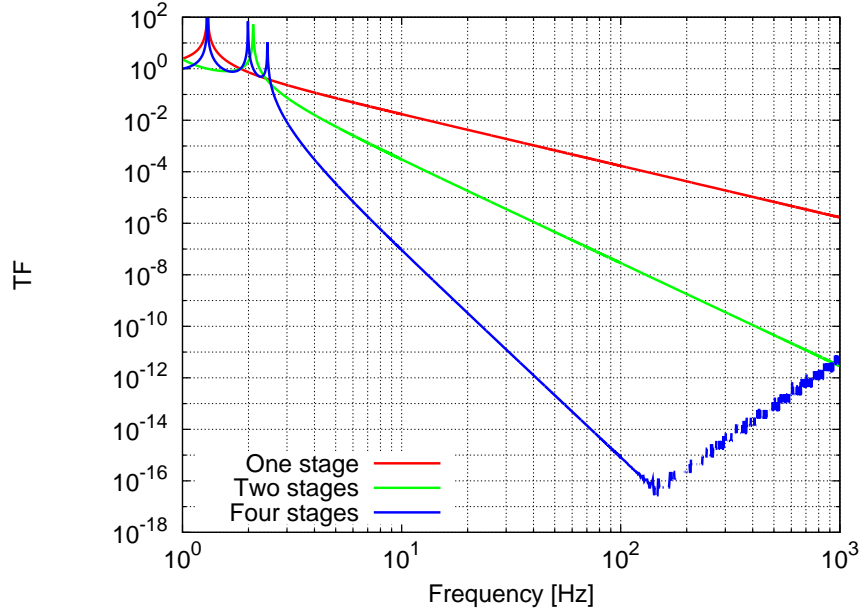


Figure 3.13.: In a two degree of freedom system the method shows numerical instabilities (depending on the number of stages), even in this case when the degrees of freedom of each subsystem are uncoupled.

After eliminating \tilde{F}^i we have

$$\begin{aligned}
 \tilde{q}^o &= \mathbf{1}q^i - \mathbb{K}^{-1} [\mathbf{1} - \omega^2\mathbb{M}\mathbb{K}^{-1}]^{-1} (-\omega^2\mathbb{M})\tilde{q}^i \\
 &= \mathbf{1}\tilde{q}^i - [\mathbb{K} - \omega^2\mathbb{M}]^{-1} (-\omega^2\mathbb{M})\tilde{q}^i \\
 &= [\mathbb{K} - \omega^2\mathbb{M}]^{-1} \mathbb{K}\tilde{q}^i
 \end{aligned} \tag{3.9.5}$$

in agreement with equation (3.8.8).

3.10. Stabilization of the algorithm

It is known that the method just described gives rise to instabilities especially for higher order systems [12]. As an example we again embed our simple system with a resonance at 1.3 Hz in a two degree of freedom formalism and we observe the results when we stack more than one stages together. The results of the simulations are shown in Figure 3.13: the method becomes unstable. In order to stabilize the algorithm we must observe that the TFs we compute are polynomial functions of the frequency. These polynomials contain terms with opposite signs and addition/subtraction of large quantities is known to be a serious issue in numerical methods [14]. We implemented a brute force approach² using a custom number of digits, bigger than the number of digits which can be obtained with `float` variables in the C language. We stress that such experiments are now possible,

²When in doubt use brute force. -Ken Thompson-

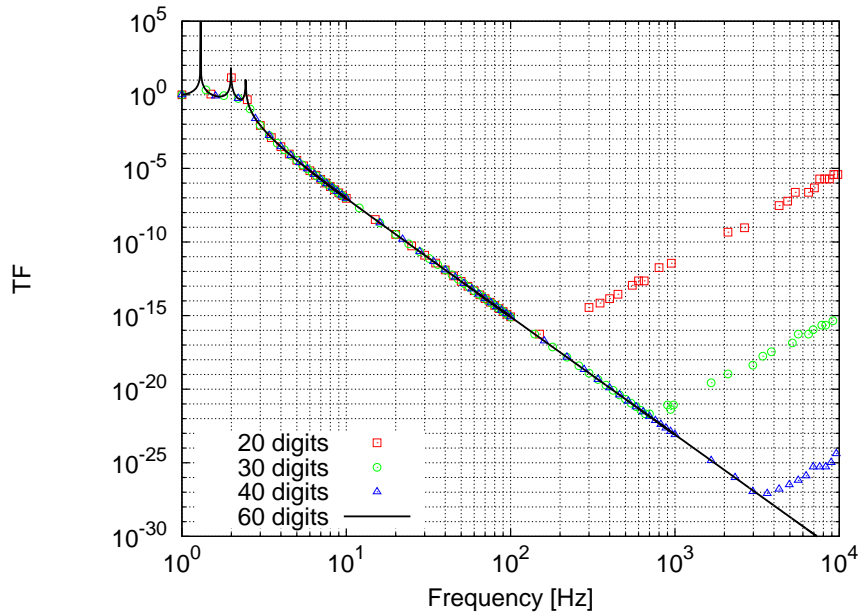


Figure 3.14.: By increasing the number of digits, the numerical instability appears at higher and higher frequencies. Given our needs for a reliable algorithm for TFs up to 1 kHz 60 digits are in this case sufficient.

given the availability of programs or programming languages that offer such a possibility. We employed here a C++ library for symbolic calculations named `ginac`³. In Figure 3.14 we show the simulation of a system with four stages and two degrees of freedom, with no coupling between them: the instability of the algorithm cannot be in principle eliminated, but with a sufficient number of digits we obtain results which are completely satisfactory.

We also observe that every 10 additional digits we can compute 5 additional orders of magnitude of the TF. This is not accidental since the TF itself depends on even powers of the frequency f^2, f^4, \dots

3.11. The next step

The results we achieved are twofold:

- We enhanced the moments of inertia of the suspended masses: the reduction of the measured length noise is a clear indication that in our suspension unwanted cross couplings between different degrees of freedom was a limiting noise source.
- We started to model the suspension by employing a method whose advantages and disadvantages are well known. We were able to eliminate the most evident disadvantage, namely its numerical instability, by using a custom number of digits during the calculations.

³Official Web site: <http://www.ginac.de>

3. Optimization of the pendulum suspension

The identification of the correct matrix to describe the pendulum suspension would enable us to consistently model the whole pendulum suspension and finally fit the measured data. This goal, which in turn would enable us to build even better seismic isolation systems, can be now regarded within reach. In the following chapters we will report our investigations into internal thermal noise, that is the noise due to the optical devices themselves.

4. Internal thermal noise

4.1. Thermal noise in mirror coatings

Internal thermal noise is the noise shown by the optical components themselves. Because of thermodynamic fluctuations in the temperature, and because of losses and absorption, optical coatings and substrates are expected to generate noise which will mimic a length noise. This length noise is expected to be the one of the dominant noise sources in GW detectors, in the frequency range around some hundreds of Hz up to 1 kHz. Despite the relevance of internal thermal noise for GW detectors (apart from some theoretical works) still very little is known. We will take Braginsky’s work as a starting point [2, 3, 4], with special attention to thermal noise arising from the optical coating.

There are four mechanisms leading to thermal noise in coatings:

- Thermodynamic fluctuations in the coating are converted by the thermal expansion coefficient α into length fluctuations: this is *thermoelastic noise*.
- Absorbed photons give rise to local temperature “jumps” in the coating, which are also converted by means of α into length noise: this is the *photo-thermal noise*.
- Thermodynamic fluctuations of temperature also gives rise to variations of the material’s refractive index, thereby changing its optical length: this is the so-called *thermorefractive noise*.
- Losses in the coating are converted to length noise through the fluctuation dissipation theorem: this is *Brownian noise (structural damping)*.

Each of these noise sources has its own “signature”, most importantly its frequency dependence, but also its parameter dependence. It is of great relevance for the optimization of GW detectors to understand these noises and to measure them in the frequency range around 1 kHz.

Let r_0, r_T, d be the laser beam radius, the diffusive heat transfer length, and the coating thickness respectively, we then require

$$r_0 \gg r_T \gg d \tag{4.1.1}$$

We will re-derive the relevant expressions for the thermoelastic and the photo-thermal noise. By a critical application of the same procedure it is possible to deduce the expression for the other two types of noise as well.

4.2. From elasticity theory to the thermoelastic problem

We give here a derivation of the formula for thermoelastic noise. Our approach is to explicitly write down some of the calculations missing in the literature, with the aim to provide some insight neither easily available nor easily reproducible by oneself. Our wish is to show a rather self-contained derivation. We will *closely* follow Landau's book¹ on elasticity [15] and Branginsky's papers [2, 3, 4].

First we will show how the basic equation of the theory of elasticity can be derived, enabling us to solve a simple problem, namely the computation of the displacement of a half-infinite body subjected to a δ -like force.

Then by using the Green tensor we will generalize this result to an arbitrary force, and finally we will apply this result to an optical substrate and its coating.

We anticipate that in this case we will have no direct force acting on the optical substrate, rather the thermodynamic temperature fluctuations will induce a stress which in turn leads to displacement of the surface, which is the quantity of interest.

4.2.1. The strain and stress tensors

Each point P of a generic body is described in a three dimensional Cartesian system by a vector $\mathbf{r} \equiv (x, y, z) \equiv (x_1, x_2, x_3)$. Subjected to a deformation, the vector \mathbf{r} representing P will become \mathbf{r}' , so that the displacement of P is

$$\mathbf{u} = \mathbf{r}' - \mathbf{r}. \quad (4.2.1)$$

Let's consider two points P and Q belonging to the body under consideration. Let dx_i and dx'_i , the components² of the difference vector between P and Q , before and after the displacement, respectively. Then distance between P and Q before the deformation is

$$dl = \sqrt{dx_1^2 + dx_2^2 + dx_3^2} \equiv \sqrt{dx_i^2} \quad (4.2.2)$$

and after the deformation is

$$dl' = \sqrt{(dx'_1)^2 + (dx'_2)^2 + (dx'_3)^2} \equiv \sqrt{(dx'_i)^2}. \quad (4.2.3)$$

Squaring both sides and using the equation (4.2.1) we have

$$dl^2 = dx_i^2 \quad (4.2.4)$$

$$(dl')^2 = (dx'_i)^2 = (dx_i + du_i)^2. \quad (4.2.5)$$

If we now write

$$du_i = \frac{\partial u_i}{\partial x_k} dx_k \quad (4.2.6)$$

¹This means that we will follow step by step Landau's arguments, adding some of the calculations that are left out there, employing the notation found there.

²Here latin indexes run over 1, 2, 3. The summing convention over repeated indices is also assumed.

then the distance between P and Q after the deformation is

$$(dl')^2 = dl^2 + 2 \frac{\partial u_i}{\partial x_k} dx_k dx_i + \frac{\partial u_i}{\partial x_t} dx_t \frac{\partial u_i}{\partial x_k} dx_k \quad (4.2.7)$$

$$= dl^2 + \left(\frac{\partial u_i}{\partial x_k} + \frac{\partial u_k}{\partial x_i} \right) dx_k dx_i + \frac{\partial u_i}{\partial x_t} dx_t \frac{\partial u_i}{\partial x_k} dx_k. \quad (4.2.8)$$

Since the indices on the right hand side of the last expression are summed over, we can rename them getting

$$(dl')^2 = dl^2 + 2u_{ik} dx_i dx_k \quad (4.2.9)$$

where we introduced the *strain tensor* u_{ik} defined as

$$u_{ik} \equiv \frac{1}{2} \left(\frac{\partial u_i}{\partial x_k} + \frac{\partial u_k}{\partial x_i} + \frac{\partial u_l}{\partial x_k} \frac{\partial u_l}{\partial x_i} \right) \approx \frac{1}{2} \left(\frac{\partial u_i}{\partial x_k} + \frac{\partial u_k}{\partial x_i} \right). \quad (4.2.10)$$

We explicitly observe that:

- the strain tensor is symmetric

$$u_{ik} = u_{ki} \quad (4.2.11)$$

- the strain tensor is dimensionless.

Let's consider the special case in which the strain tensor is diagonal: in this case the length element $(dl')^2$ after the deformation is

$$dl' = (\delta_{ik} + 2u_{ik}) dx_i dx_k \quad (4.2.12)$$

$$= (1 + 2u_{11}) dx_1^2 + (1 + 2u_{22}) dx_2^2 + (1 + 2u_{33}) dx_3^2. \quad (4.2.13)$$

In particular, the relative length change along -let's say the x-axis- can be written as

$$\frac{dx'_1 - dx_1}{dx_1} = \sqrt{1 + 2u_{11}} - 1 \approx u_{11} \quad (4.2.14)$$

and the relative volume change is

$$\frac{dV' - dV}{dV} = u_{ii}. \quad (4.2.15)$$

this is a useful result: the trace of the strain tensor represents the relative volume change. The strain tensor tells us about the deformation of the body: in addition, we need another tensor more closely related to the cause of the deformations. This is the so-called *stress tensor*. To introduce it, let's consider a portion of our arbitrary body and the force acting on it. This force can be written as

$$\int \mathbf{F} dV \quad (4.2.16)$$

where \mathbf{F} is the force per unit volume acting on the unit volume of the body, so that $\mathbf{F} dV$ is the force acting on dV . Since inside the volume the resulting force has to be equal to

zero, the net force on the volume should be expressed only via a surface integral. This can be done by introducing a tensor σ_{ik} such that

$$F_i \equiv \frac{\partial \sigma_{ik}}{\partial x_k}. \quad (4.2.17)$$

Now we can transform the volume integral into a surface one

$$\int F_i dV = \int \frac{\partial \sigma_{ik}}{\partial x_k} dV = \oint \sigma_{ik} df_k \quad (4.2.18)$$

where df_k are the components of the vector $d\mathbf{f}$ of an element of the surface, oriented as the external normal to the surface. The σ_{ik} is the so-called *stress tensor*.

Three important facts regarding σ_{ik} should be noted:

- σ_{ik} is symmetric

$$\sigma_{ik} = \sigma_{ki}. \quad (4.2.19)$$

- The stress tensor corresponding to a uniform compression can be expressed as

$$\sigma_{ik} = -p\delta_{ik} \quad (4.2.20)$$

where p is the pressure and δ_{ik} the usual Kronecker delta symbol. From this we get the important result that the dimensions of σ_{ik} are the same as that of a pressure, namely $\text{N} \cdot \text{m}^{-2}$.

- For a body in equilibrium, when no other forces are present, we must have

$$\frac{\partial \sigma_{ik}}{\partial x_k} = 0. \quad (4.2.21)$$

The natural question to ask now is: “what is the relationship between u_{ik} and σ_{ik} ?”

We can answer this question by considering a body subjected to small deformations δu_i due to internal stresses. The work δR done by the forces of the internal stresses per unit volume is

$$\delta R = F_i \delta u_i = \frac{\partial \sigma_{ik}}{\partial x_k} \delta u_i. \quad (4.2.22)$$

Integrating over the body

$$R = \int \delta R dV = \int \frac{\partial \sigma_{ik}}{\partial x_k} \delta u_i dV \quad (4.2.23)$$

and then integrating by parts

$$\int \delta R dV = \oint \sigma_{ik} \delta u_i df_k - \int \sigma_{ik} \frac{\partial \delta u_i}{\partial x_k} dV \quad (4.2.24)$$

By considering an unlimited body whose deformation at infinity is negligible, we can discard the surface term leaving us with

$$\int \delta R dV = -\frac{1}{2} \int \sigma_{ik} \left(\frac{\partial \delta u_i}{\partial x_k} + \frac{\partial \delta u_k}{\partial x_i} \right) dV \quad (4.2.25)$$

$$= - \int \sigma_{ik} \delta u_{ik} dV \quad (4.2.26)$$

and then

$$\delta R = -\sigma_{ik}\delta u_{ik}. \quad (4.2.27)$$

We can check the physical dimensions of this results³. Since R is a work term, its dimensions are Joule. Therefore

$$[\delta R] = \text{J} \cdot \text{m}^{-3} = \text{N} \cdot \text{m}^{-2} = [\sigma_{ik}] = [\sigma_{ik}\delta u_{ik}] \quad (4.2.28)$$

since u_{ik} is dimensionless. If we consider the body undergoing a reversible thermodynamical transformation then, from a well known result, we can write for the variation of the internal energy E per unit volume

$$dE = TdS - dR \quad (4.2.29)$$

(T and S are temperature and entropy, respectively). Substituting our expression for dR we get

$$dE = TdS + \sigma_{ik}du_{ik} \quad (4.2.30)$$

or, recalling the definition of the free energy (per unit volume) F ,

$$F = E - TS \quad (4.2.31)$$

$$dF = -SdT + \sigma_{ik}du_{ik}. \quad (4.2.32)$$

Differentiating E with respect to u_{ik} at constant entropy gives us

$$\sigma_{ik} = \left(\frac{\partial E}{\partial u_{ik}} \right)_S \quad (4.2.33)$$

and similarly

$$\sigma_{ik} = \left(\frac{\partial F}{\partial u_{ik}} \right)_T \quad (4.2.34)$$

This important result, connecting thermodynamic with elasticity theory, will be very useful in the following.

4.2.2. Hooke's law

In order to be able to apply the thermodynamic relation we obtained, it is necessary to know the explicit expression of the free energy of the body as a function of the strain tensor. This expression can be easily found in the case of small deformation of isotropic bodies, by expressing F as a power series in u_{ik} . If we consider a body at constant temperature with no deformation, we must have no stress, and since

$$\sigma_{ik} = \frac{\partial F}{\partial u_{ik}} \quad (4.2.35)$$

we can say that F cannot have terms linear in u_{ik} . It is known that from a symmetric tensor one can build only two independent scalars which are quadratic in the tensor

³We also observe that the summed indices are correctly paired, we have a scalar both on the left and the right hand side of the equation.

components: we can choose u_{ii}^2 , the square of the sum of the diagonal components, and u_{ik}^2 the sum of the square of the tensor components⁴. Developing F in a power series of u_{ik} and stopping at the second order term, we can then write for the free energy of a deformed body

$$F = \frac{\lambda}{2}u_{ii}^2 + \mu u_{ik}^2 \quad (4.2.36)$$

where λ and μ are known as Lamé coefficients. It is useful to consider two kinds of deformation: the ones in which the volume remains constant but the body's shape changes (also known as *shear deformation*), and the ones in which the volume changes while the body's shape remains constant (also known as *compression*). For compression the strain tensor is a diagonal tensor. It turns out that each arbitrary deformation can be expressed as a shear and as a uniform compression: for this purpose we write down the following identity

$$u_{ik} = \left(u_{ik} - \frac{1}{3}\delta_{ik}u_{ll} \right) + \frac{1}{3}\delta_{ik}u_{ll}. \quad (4.2.37)$$

The first term is a pure shear since $\delta_{ii} = 3$ and the second one is a uniform compression. Letting

$$\Omega_{ik} \equiv u_{ik} - \frac{1}{3}\delta_{ik}u_{ll} \quad (4.2.38)$$

we can re-express F as:

$$\begin{aligned} F &= \frac{\lambda}{2}u_{ii}^2 + \mu \left(\Omega_{ik} + \frac{1}{3}\delta_{ik}u_{ll} \right)^2 \\ &= \frac{\lambda}{2}u_{ii}^2 + \mu \left(\Omega_{ik}^2 + \frac{1}{9}\delta_{ik}u_{ll}\delta_{ik}u_{ll} + \frac{2}{3}\delta_{ik}\Omega_{ik}u_{ll} \right) \\ &= \frac{\lambda}{2}u_{ii}^2 + \mu \left(\Omega_{ik}^2 + \frac{1}{3}u_{ll}u_{ll} + \frac{2}{3}\delta_{ik}\Omega_{ik}u_{ll} \right) \\ &= \left(\frac{\lambda}{2} + \frac{1}{3}\mu \right) u_{ii}^2 + \mu(\Omega_{ik})^2 + \frac{2}{3}\mu\delta_{ik}u_{ll} \left(u_{ik} - \frac{1}{3}\delta_{ik}u_{ll} \right) \\ &= \left(\frac{\lambda}{2} + \frac{1}{3}\mu \right) u_{ii}^2 + \mu(\Omega_{ik})^2 + \frac{2}{3}\mu\delta_{ik}u_{ll}u_{ik} - \frac{2}{9}\mu\delta_{ik}\delta_{ik}u_{ll}u_{ll} \\ &= \left(\frac{\lambda}{2} + \frac{1}{3}\mu \right) u_{ii}^2 + \mu(\Omega_{ik})^2 + \left(\frac{2}{3} - \frac{6}{9} \right) \mu u_{ll}^2 \end{aligned}$$

giving

$$F = \mu\Omega_{ik}^2 + \frac{K}{2}u_{ll}^2 \quad (4.2.39)$$

where we introduced

$$K \equiv \lambda + \frac{2}{3}\mu. \quad (4.2.40)$$

Since the free energy is a positive definite quantity and since K and μ are independent quantities related to compressions and shears respectively, they must be both positive

$$K > 0 \quad \mu > 0. \quad (4.2.41)$$

⁴The difference between these two quantities will be very important in the following calculations.

The stress tensor can be computed as the derivative of the free energy at constant temperature. As an intermediate step we compute the differential of F , dF .

$$\begin{aligned} dF &= K u_{ll} du_{tt} + 2\mu \Omega_{ik} d\Omega_{ik} \\ &= K u_{ll} du_{tt} + 2\mu \left(u_{ik} - \frac{1}{3} \delta_{ik} u_{ll} \right) du_{ik} - \frac{2}{3} \delta_{ik} \mu \left(u_{ik} - \frac{1}{3} \delta_{ik} u_{ll} \right) du_{tt} \\ &= K u_{ll} du_{tt} + 2\mu \left(u_{ik} - \frac{1}{3} \delta_{ik} u_{ll} \right) du_{ik} - \frac{2}{3} \mu \left(u_{ii} - \frac{3}{3} u_{ll} \right) du_{tt} \end{aligned}$$

that is

$$dF = K u_{ll} du_{tt} + 2\mu \left(u_{ik} - \frac{1}{3} \delta_{ik} u_{ll} \right) du_{ik} \quad (4.2.42)$$

and the stress tensor is

$$\sigma_{ik} = \frac{\partial F}{\partial u_{ik}} = K u_{ll} \delta_{ik} + 2\mu \left(u_{ik} - \frac{1}{3} \delta_{ik} u_{ll} \right). \quad (4.2.43)$$

We can compute the sum of the diagonal elements of the stress tensor as

$$\sigma_{ii} = K u_{ll} \delta_{ii} + 2\mu \left(u_{ii} - \frac{1}{3} \delta_{ii} u_{ll} \right) = 3K u_{ll}. \quad (4.2.44)$$

Another relation that will be used is the “inverse” relation, that is the expression of u_{ik} as a function of σ_{ik} . In doing this it is sensible to handle the two cases $i = k$ and $i \neq k$ separately, since expressions like σ_{ii} are error prone, due to our summing convention.

$$\sigma_{ik} = \begin{cases} K u_{ll} + 2\mu \left(u_{ik} - \frac{1}{3} u_{ll} \right) & i = k \\ 2\mu u_{ik} & i \neq k \end{cases} \quad (4.2.45)$$

$$= \begin{cases} 2\mu u_{ik} + u_{ll} \left(K - \frac{2}{3} \mu \right) & i = k \\ 2\mu u_{ik} & i \neq k \end{cases} \quad (4.2.46)$$

Re-gathering the two cases together

$$\sigma_{ik} = 2\mu u_{ik} + \delta_{ik} u_{ll} \left(K - \frac{2}{3} \mu \right) \quad (4.2.47)$$

$$u_{ik} = \frac{1}{2\mu} \left[\sigma_{ik} - \delta_{ik} u_{ll} \left(K - \frac{2}{3} \mu \right) \right] \quad (4.2.48)$$

$$= \frac{1}{2\mu} \left[\sigma_{ik} - \frac{\delta_{ik} \sigma_{ll}}{3K} \left(K - \frac{2}{3} \mu \right) \right] \quad (4.2.49)$$

$$= \frac{1}{9K} \delta_{ik} \sigma_{ll} + \frac{1}{2\mu} \left(\sigma_{ik} - \frac{1}{3} \delta_{ik} \sigma_{ll} \right) \quad (4.2.50)$$

This last equation which states that the deformation is proportional to the applied force, is Hooke's law. The physical dimensions of K, μ are the same as of σ_{ik}

$$[K] = [\mu] = \text{N} \cdot \text{m}^{-2}. \quad (4.2.51)$$

Following the standard literature one introduces the Young modulus E and and Poisson's ratio σ

$$E \equiv \frac{9K\mu}{3K + \mu} \quad (4.2.52)$$

$$\sigma \equiv \frac{1}{2} \frac{3K - 2\mu}{3K + \mu}. \quad (4.2.53)$$

By direct substitution we get F, σ_{ik}, u_{ik} expressed by means of E, σ

$$F = \frac{E}{2(1 + \sigma)} \left(u_{ik}^2 + \frac{\sigma}{1 - 2\sigma} u_{ll}^2 \right) \quad (4.2.54)$$

$$\sigma_{ik} = \frac{E}{1 + \sigma} \left(u_{ik} + \frac{\sigma}{1 - 2\sigma} u_{ll} \delta_{ik} \right) \quad (4.2.55)$$

$$u_{ik} = \frac{1}{E} [(1 + \sigma)\sigma_{ik} - \sigma\sigma_{ll}\sigma_{ik}]. \quad (4.2.56)$$

The physical dimensions of E, σ are

$$[E] = \text{N} \cdot \text{m}^{-2} \quad (4.2.57)$$

$$[\sigma] \quad \text{dimensionless} \quad (4.2.58)$$

From here on, we will employ the expressions containing the constants E, σ .

4.2.3. The equilibrium equations

We are now in a position to write the equilibrium equation for an isotropic body: this equation comes in many different forms, but it can always be deduced from very simple principles. Let's consider for example an isotropic body subjected only to internal stresses: the equilibrium equation reads

$$\frac{\partial \sigma_{ik}}{\partial x_k} = 0. \quad (4.2.59)$$

Regarding external forces that are directly applied to the body and usually are the cause of deformations, they appear as boundary conditions that should be obeyed by the solution of the equilibrium equation. If we indicate with \mathbf{P} the external force per unit area acting on the unit surface of the body, $\mathbf{P}df$ is the force acting on the element df . At equilibrium this force has to be compensated by $-\sigma_{ik}df_k$. We have then

$$P_i df - \sigma_{ik} df_k = 0. \quad (4.2.60)$$

Writing

$$df_k = n_k df \quad (4.2.61)$$

where \mathbf{n} is the unit vector normal to the surface, we have

$$\sigma_{ik}n_k = P_i. \quad (4.2.62)$$

This boundary condition will be used in the forthcoming calculations. We now give an explicit form for the equilibrium equations. Using our expression for the stress tensor employing E and σ we have⁵

$$\frac{\partial}{\partial x_k} \left(\frac{\sigma}{(1-2\sigma)} u_{ll} \delta_{ik} + u_{ik} \right) = 0 \quad (4.2.63)$$

$$\frac{\sigma}{(1-2\sigma)} \frac{\partial u_{ll}}{\partial x_i} + \frac{\partial u_{ik}}{\partial x_k} = 0. \quad (4.2.64)$$

After substituting the definition of the strain tensor in terms of the displacement, we get the following second order differential equation for the displacement itself:

$$\frac{\partial^2 u_i}{\partial x_k^2} + \frac{1}{(1-2\sigma)} \frac{\partial^2 u_l}{\partial x_i \partial x_l} = 0. \quad (4.2.65)$$

To help to translate this equation into vectorial form, we introduce the following unit vectors

$$\hat{i} \equiv \text{unit vector along the } x \text{ axis} \quad (4.2.66)$$

$$\hat{j} \equiv \text{unit vector along the } y \text{ axis} \quad (4.2.67)$$

$$\hat{k} \equiv \text{unit vector along the } z \text{ axis} \quad (4.2.68)$$

and we recall the definitions of three operators:

- the divergence of a vector \mathbf{u}

$$\vec{\nabla} \cdot \mathbf{u} \equiv \sum_{i=1}^3 \frac{\partial u_i}{\partial x_i} \equiv \frac{\partial u_i}{\partial x_i} \quad (4.2.69)$$

- the gradient of a scalar ϕ

$$\vec{\nabla} \phi \equiv \hat{i} \frac{\partial \phi}{\partial x} + \hat{j} \frac{\partial \phi}{\partial y} + \hat{k} \frac{\partial \phi}{\partial z} \quad (4.2.70)$$

- the Laplacian of a scalar ϕ

$$\Delta \phi \equiv \frac{\partial^2 \phi}{\partial x^2} + \frac{\partial^2 \phi}{\partial y^2} + \frac{\partial^2 \phi}{\partial z^2} \quad (4.2.71)$$

⁵ E, σ are *not* supposed to depend on x_i .

By virtue of linearity we can also apply the Laplacian (component-wise) to a vector \mathbf{u} , obtaining

$$\begin{aligned}\Delta \mathbf{u} &\equiv \hat{i}\Delta u_x + \hat{j}\Delta u_y + \hat{k}\Delta u_z \\ &= \hat{i}\left(\frac{\partial^2 u_x}{\partial x^2} + \frac{\partial^2 u_x}{\partial y^2} + \frac{\partial^2 u_x}{\partial z^2}\right) \\ &\quad + \hat{j}\left(\frac{\partial^2 u_y}{\partial x^2} + \frac{\partial^2 u_y}{\partial y^2} + \frac{\partial^2 u_y}{\partial z^2}\right) \\ &\quad + \hat{k}\left(\frac{\partial^2 u_z}{\partial x^2} + \frac{\partial^2 u_z}{\partial y^2} + \frac{\partial^2 u_z}{\partial z^2}\right)\end{aligned}$$

It is then easy to see that Equation (4.2.65) can be written in vector form as

$$\Delta \mathbf{u} + \frac{1}{1-2\sigma} \vec{\nabla} \vec{\nabla} \mathbf{u} = \mathbf{0}. \quad (4.2.72)$$

If we use the following standard result from vector analysis

$$\vec{\nabla} \vec{\nabla} \mathbf{u} = \Delta \mathbf{u} + \vec{\nabla} \times (\vec{\nabla} \times \mathbf{u}) \quad (4.2.73)$$

we can equivalently write

$$\vec{\nabla} \vec{\nabla} \mathbf{u} - \frac{1-2\sigma}{2(1-\sigma)} \vec{\nabla} \times (\vec{\nabla} \times \mathbf{u}) = \mathbf{0}. \quad (4.2.74)$$

It is important to note that surface forces do appear in the solutions only through the boundary conditions. The equilibrium equations we wrote do not take any other volume forces into account, other than the ones resulting from the stress itself. This is not enough to study the effect of temperature variation, since on a qualitative basis, temperature variation leads via the expansion coefficient to additional volume forces that should appear in the equilibrium equation. However the correction can be made afterwards, this means that, given the equilibrium equations we found, we can “add” additional terms that represent such a volume force. The appropriate starting point is our expression of the free energy F

$$F = \frac{K}{2} u_{ll}^2 + \mu \Omega_{ik}^2. \quad (4.2.75)$$

Variation of the temperature causes the free energy to change; if we take this change as small we can introduce an extra term into the free energy which is a first order scalar built from u_{ik} . The only possible choice is then to add a term proportional to the temperature change and to u_{ll} , therefore we can write

$$F(T) = -K\alpha(T - T_0)u_{ll} + \mu\Omega_{ik} + \frac{K}{2}u_{ll}^2. \quad (4.2.76)$$

The stress tensor becomes then

$$\sigma_{ik} = \frac{\partial F}{\partial u_{ik}} = -K\alpha(T - T_0)\delta_{ik} + K u_{ll}\delta_{ik} + 2\mu\Omega_{ik} \quad (4.2.77)$$

where α is a new extra coefficient we added. What can we say about it? Let's look at the case in which the body undergoes a *free thermal expansion*: in such a case the stress must be identically zero; $\sigma_{ik} = 0$. This in turn means that the displacement vector u_{ik} must be diagonal, moreover we have for the sum of its diagonal elements

$$u_{ll} = \alpha(T - T_0) \quad (4.2.78)$$

$$u_{ll} = \frac{dV}{V}. \quad (4.2.79)$$

since the sum of the diagonal elements is the relative volume change, we can say that α is the thermal volumetric⁶ expansion coefficient. With the extra term due to the thermal expansion the equilibrium equation now reads

$$\frac{\partial \sigma_{ik}}{\partial x_k} = \frac{E\sigma}{(1+\sigma)(1-2\sigma)} \frac{u_{ll}}{x_i} + \frac{E}{1+\sigma} \frac{\partial u_{ik}}{\partial x_k} - K\alpha \frac{\partial T}{\partial x_i} = 0. \quad (4.2.80)$$

Inserting the expression for K , and moving to vector notation we have

$$\frac{E}{1-2\sigma} \left[\frac{3(1-\sigma)}{1+\sigma} \vec{\nabla} \vec{\nabla} \mathbf{u} - \frac{3(1-2\sigma)}{2(1+\sigma)} \vec{\nabla} \times (\vec{\nabla} \times \mathbf{u}) \right] = \frac{E}{1-2\sigma} \alpha \vec{\nabla} T. \quad (4.2.81)$$

The reason why we do not simplify the coefficients that appear in both the right and the left hand sides of this equation is an important one.

The left hand side is more related to the body under study and to its elastic properties. The right hand side is more related to the source term which leads to the stress. If we have a body which can be thought of as a composition of a bulk and a coating and if we are interested in studying the stress induced by the coating, then we must substitute into the left hand side the parameters for the body itself that are responsible for the global elastic properties of the whole body, and into the right hand side the parameters for the coating, which are to be considered as "source" terms.

4.2.4. Equilibrium of an elastic body constrained by a plane

Before we can attack the main problem, we can benefit by studying the following example, whose geometry is already similar to the one we will employ in the thermal noise calculation. Let's consider a semi-infinite elastic body whose free surface we choose to be coincident with the plane $z = 0$. Our goal is to find the deformation of the surface as a response to forces applied on that surface.

The equilibrium equation is

$$\vec{\nabla} \vec{\nabla} \mathbf{u} + (1-2\sigma) \Delta \mathbf{u} = \mathbf{0} \quad (4.2.82)$$

We look for solutions which are of the form

$$\mathbf{u} = \mathbf{f} + \vec{\nabla} \phi \quad (4.2.83)$$

⁶The term volumetric is quite relevant since we will see that in Braginsky's paper another expansion coefficient is introduced, leading to an annoying "missing coefficient problem."

where ϕ is a scalar and the vector \mathbf{f} obeys the Laplace equation

$$\Delta \mathbf{f} = \mathbf{0}. \quad (4.2.84)$$

Substituting equation (4.2.83) into (4.2.82)

$$\vec{\nabla} \vec{\nabla} \mathbf{f} + 2(1 - 2\sigma)\Delta(\vec{\nabla} \phi) = \mathbf{0} \quad (4.2.85)$$

$$\vec{\nabla} \left(\vec{\nabla} \mathbf{f} + 2(1 - 2\sigma)\Delta \phi \right) = \mathbf{0} \quad (4.2.86)$$

gives

$$2(1 - 2\sigma)\Delta \phi = -\vec{\nabla} \mathbf{f}. \quad (4.2.87)$$

Let's choose the reference system such that the z axis is directed into the body. We now write f_x and f_y as derivatives with respect to z of two corresponding functions g_x and g_y belonging to a vector function \mathbf{g}

$$f_x \equiv \frac{\partial g_x}{\partial z}; \quad f_y \equiv \frac{\partial g_y}{\partial z}. \quad (4.2.88)$$

Since f_x and f_y obey the Laplace equation, g_x and g_y can be chosen such that they obey it also

$$\Delta g_x = 0; \quad \Delta g_y = 0 \quad (4.2.89)$$

Then Equation (4.2.87) becomes (by exchanging the order in which the derivatives are taken)

$$2(1 - 2\sigma)\Delta \phi = -\frac{\partial}{\partial z} \left(\frac{\partial g_x}{\partial x} + \frac{\partial g_y}{\partial y} + f_z \right). \quad (4.2.90)$$

Since f_z , g_x , g_y are harmonic functions, that is they obey Laplace equation, we can express ϕ in the following way

$$\phi = -\frac{z}{4(1 - \sigma)} \left(f_z + \frac{\partial g_x}{\partial x} + \frac{\partial g_y}{\partial y} \right) + \psi \quad (4.2.91)$$

where ψ is also harmonic

$$\Delta \psi = 0. \quad (4.2.92)$$

We have reduced the problem of finding \mathbf{u} to the problem of finding f_z , g_x , g_y and ψ , each satisfying the Laplace equation. The boundary conditions for this problem are simple, since we have only one free surface at our disposal and we are interested only in the response to a pressure applied orthogonally to that surface. Mathematically the boundary condition (4.2.62) now simplifies to

$$\sigma_{xz}|_{z=0} = 0 \quad (4.2.93)$$

$$\sigma_{yz}|_{z=0} = 0 \quad (4.2.94)$$

$$\sigma_{zz}|_{z=0} = P_z. \quad (4.2.95)$$

Substituting the expression for σ_{ik} as function of g_x, g_z, f_z and ψ we have

$$\left\{ \frac{\partial^2 g_x}{\partial z^2} + \frac{\partial \Gamma}{\partial x} \right\} \Big|_{z=0} = 0 \quad (4.2.96)$$

$$\left\{ \frac{\partial^2 g_y}{\partial z^2} + \frac{\partial \Gamma}{\partial x} \right\} \Big|_{z=0} = 0 \quad (4.2.97)$$

$$\frac{\partial}{\partial z} \left\{ f_z - \left(\frac{\partial g_x}{\partial x} + \frac{\partial g_y}{\partial y} \right) + 2 \frac{\partial \psi}{\partial z} \right\} \Big|_{z=0} = -\frac{2(1+\sigma)}{E} P_z \quad (4.2.98)$$

where we introduced the quantity

$$\Gamma \equiv \frac{1-2\sigma}{2(1-\sigma)} f_z - \frac{1}{2(1-\sigma)} \left(\frac{\partial g_x}{\partial x} + \frac{\partial g_y}{\partial y} \right) + 2 \frac{\partial \psi}{\partial z}. \quad (4.2.99)$$

It turns out that since the functions f_x, g_x, g_y and ψ we introduced are not uniquely determined by their defining formulas, we are still left with some freedom in their specification: we then require that

$$\Gamma = 0 \quad (4.2.100)$$

so that the boundary conditions simplify to

$$\frac{\partial^2 g_x}{\partial z^2} \Big|_{z=0} = 0 \quad (4.2.101)$$

$$\frac{\partial^2 g_y}{\partial z^2} \Big|_{z=0} = 0 \quad (4.2.102)$$

$$\frac{\partial}{\partial z} \left\{ f_z - \left(\frac{\partial g_x}{\partial x} + \frac{\partial g_y}{\partial y} \right) + 2 \frac{\partial \psi}{\partial z} \right\} \Big|_{z=0} = -\frac{2(1+\sigma)}{E} P_z. \quad (4.2.103)$$

Now that we have set up the proper equations and the proper boundary conditions, we specify the kind of force to apply to the free surface. The force will be δ -like, parallel to the z -axis and applied to the center of the reference system:

$$P_z = F_z \delta(x) \delta(y). \quad (4.2.104)$$

This kind of pressure, despite its very singular mathematical behavior, can be easily handled since in the following this pressure will be integrated over x and y and the presence of the δ functions makes computing the integral trivial. Moreover, once the problem for a δ -like pressure is known, we can, by using the standard Green's tensor method, easily solve for arbitrary pressures. It is known from potential theory that a harmonic function Υ going to zero at infinity and having a normal derivative $\frac{\partial \Upsilon}{\partial z}$ at $z = 0$ is given by the expression

$$\Upsilon(x, y, z) = -\frac{1}{2\pi} \iint \frac{\partial \Upsilon(x', y', z)}{\partial z} \Big|_{z=0} \frac{dx' dy'}{\tilde{r}} \quad (4.2.105)$$

$$\tilde{r} \equiv \sqrt{(x-x')^2 + (y-y')^2 + z^2}. \quad (4.2.106)$$

Now substituting for Υ the following three functions

$$\Upsilon_1 \equiv f_z - \left(\frac{\partial g_x}{\partial x} + \frac{\partial g_y}{\partial y} \right) + 2 \frac{\partial \psi}{\partial z} \quad (4.2.107)$$

$$\Upsilon_2 \equiv \frac{\partial g_x}{\partial z} \quad (4.2.108)$$

$$\Upsilon_3 \equiv \frac{\partial g_y}{\partial z} \quad (4.2.109)$$

whose boundary conditions we have already computed, we get

$$\begin{aligned} \Upsilon_1(x, y, z) &= -\frac{1}{2\pi} \iint \frac{\partial \Upsilon_1(x', y', z)}{\partial z} \Big|_{z=0} \frac{dx' dy'}{\tilde{r}} = \\ &= -\frac{1}{2\pi} \frac{-2(1+\sigma)}{E} \iint P_z \frac{dx' dy'}{\tilde{r}} = \frac{1+\sigma}{\pi E} \frac{F_z}{r} \\ \Upsilon_2(x, y, z) &= -\frac{1}{2\pi} \iint \frac{\partial \Upsilon_2(x', y', z)}{\partial z} \Big|_{z=0} \frac{dx' dy'}{\tilde{r}} = 0 \\ \Upsilon_3(x, y, z) &= -\frac{1}{2\pi} \iint \frac{\partial \Upsilon_3(x', y', z)}{\partial z} \Big|_{z=0} \frac{dx' dy'}{\tilde{r}} = 0 \\ \tilde{r} &\equiv \sqrt{(x-x')^2 + (y-y')^2 + z^2} \\ r &\equiv \sqrt{x^2 + y^2 + z^2}. \end{aligned}$$

Or, using the definitions of Υ_i

$$f_z - \left(\frac{\partial g_x}{\partial x} + \frac{\partial g_y}{\partial y} \right) + 2 \frac{\partial \psi}{\partial z} = \frac{1+\sigma}{\pi E} \frac{F_z}{r} \quad (4.2.110)$$

$$\frac{\partial g_x}{\partial z} = 0 \quad (4.2.111)$$

$$\frac{\partial g_y}{\partial z} = 0. \quad (4.2.112)$$

Taking the derivative of $\partial g_x / \partial z$ with respect to x and then integrating with respect to dz from ∞ to z we obtain

$$\frac{\partial g_x}{\partial x} = 0 \quad (4.2.113)$$

and similarly

$$\frac{\partial g_y}{\partial y} = 0. \quad (4.2.114)$$

We are left with a system of two equations in two unknowns: f_z and $\partial \psi / \partial z$, namely

$$\Gamma = \frac{1-2\sigma}{2(1-\sigma)} f_z + 2 \frac{\partial \psi}{\partial z} = 0 \quad (4.2.115)$$

$$f_z + 2 \frac{\partial \psi}{\partial z} = \frac{1+\sigma}{\pi E} \frac{F_z}{r} \quad (4.2.116)$$

which gives

$$f_z = \frac{2(1 - \sigma^2) F_z}{\pi E r} \quad (4.2.117)$$

$$\frac{\partial \psi}{\partial z} = \frac{(2\sigma - 1)(1 + \sigma) F_z}{2\pi E r}. \quad (4.2.118)$$

The displacement of the free surface is finally given by

$$u_z|_{z=0} = \frac{1 - \sigma^2}{\pi E} \frac{F_z}{r} \Big|_{z=0}. \quad (4.2.119)$$

If we remember the definition of F_z we can write

$$\begin{aligned} u_z|_{z=0} &= \frac{1 - \sigma^2}{\pi E} \int_{-\infty}^{\infty} \int_{-\infty}^{\infty} dx' dy' \frac{F_z \delta(x - x') \delta(y - y')}{\sqrt{(x - x')^2 + (y - y')^2}} \\ &= \frac{1 - \sigma^2}{\pi E} \int_{-\infty}^{\infty} \int_{-\infty}^{\infty} dx' dy' \frac{P_z|_{z=0}}{\sqrt{(x - x')^2 + (y - y')^2}}. \end{aligned} \quad (4.2.120)$$

In the simple case of a uniform compression, the pressure along the z -axis, for example, is just the σ_{33} component of the stress tensor. In this particular case we have

$$u_z|_{z=0} = \frac{1 - \sigma^2}{\pi E} \int_{-\infty}^{\infty} \int_{-\infty}^{\infty} dx' dy' \frac{\sigma_{zz}(x', y')|_{z=0}}{\sqrt{(x - x')^2 + (y - y')^2}}. \quad (4.2.121)$$

This result, though very specific, is the key to understanding thermoelastic noise, since in the thermoelastic noise calculations no forces appear directly and one has to compute the displacement of the free surface expressing it as an integral on the stress tensor which in turn, through the elasticity and the heat equation, is connected to temperature fluctuations whose behavior is known from thermodynamics.

4.3. The thermoelastic problem

We can now face the main task: the derivation of the expression for thermoelastic noise as given by Braginsky [4]. Before turning to the actual calculation we point out that just by the word “thermoelastic” we are faced with two kinds of problems mixed together: we have an elastic problem where no direct forces are applied to the body, rather the stresses which cause the displacements are due to thermodynamic fluctuations of the temperature, which are converted thorough the expansion coefficient into volume change and then stress.

We will from now on employ Braginsky’s notation [4]. Such a decision to change the notation in the middle of a work which should be consistent is motivated by the desire to be able to closely follow two distinct but related works, and to show the links between

them. The temperature fluctuations are given quite generally by the heat equation with a source term, which we will write as

$$\frac{\partial u}{\partial t} - a^2 \Delta u = F(\mathbf{r}, t) \quad (4.3.1)$$

$$a \equiv \frac{\kappa}{\rho C} \quad (4.3.2)$$

where u is the temperature fluctuation of the body at (\mathbf{r}, t) around the mean value T , and the source term F is a statistical term whose mean value is given by⁷

$$\begin{aligned} \langle F(\mathbf{r}, t) F^*(\mathbf{r}_1, t_1) \rangle &= 2 \frac{k_B T^2 \kappa}{(\rho C)^2} \delta(t - t_1) \Delta \Upsilon \\ \Upsilon &\equiv [\delta(x - x_1) \delta(y - y_1) (\delta(z - z_1) + \delta(z + z_1))]. \end{aligned} \quad (4.3.3)$$

If we take the Fourier transform of the heat equation, the temperature fluctuations can be written as

$$u(\mathbf{r}, t) = \int_{-\infty}^{\infty} \int_{-\infty}^{\infty} \int_{-\infty}^{\infty} \int_{-\infty}^{\infty} \frac{d^3 k d\omega}{(2\pi)^4} u(\mathbf{k}, \omega) e^{i\omega t + i\mathbf{k}\mathbf{r}} \quad (4.3.4)$$

$$u(\mathbf{k}, \omega) = \frac{F(\mathbf{k}, \omega)}{a^2(\mathbf{k})^2 + i\omega} \quad (4.3.5)$$

$$\begin{aligned} \langle F(\mathbf{k}, \omega) F^*(\mathbf{k}_1, \omega_1) \rangle &= (2\pi)^4 \left(2 \frac{k_B T^2 \kappa}{(\rho C)^2} \right) \delta(\omega - \omega_1) |\mathbf{k}|^2 \tilde{\Upsilon} \\ &= F_0^2 T_0^2 (2\pi)^4 |\mathbf{k}|^2 \tilde{\Upsilon} \end{aligned} \quad (4.3.6)$$

where

$$\begin{aligned} \tilde{\Upsilon} &\equiv [\delta(k_x - k_{x_1}) \delta(k_y - k_{y_1}) (\delta(k_z - k_{z_1}) + \delta(k_z + k_{z_1}))] \\ F_0^2 T_0^2 &\equiv 2 \frac{k_B T^2 \kappa}{(\rho C)^2}. \end{aligned}$$

We approximate the body under investigation by a semi-infinite one: the elasticity equation is then (we indicate Poisson's ratio⁸ with ν and the elastic deformations with \vec{v})

$$\frac{1 - \nu}{1 + \nu} \vec{\nabla} \vec{\nabla} \vec{v} - \frac{1 - 2\nu}{2(1 + \nu)} \vec{\nabla} \times \vec{\nabla} \times \vec{v} = \alpha \vec{\nabla} \mathbf{u}. \quad (4.3.7)$$

The boundary conditions on the free surface are given by

$$\sigma_{zz}|_{z=0} = 0 \quad (4.3.8)$$

$$\sigma_{yz}|_{z=0} = 0 \quad (4.3.9)$$

$$\sigma_{xz}|_{z=0} = 0 \quad (4.3.10)$$

⁷We explicitly introduce complex conjugation and complex terms like $e^{i\omega t}$ for the Fourier transform. At the end of a calculation, when a physically measurable quantity is presented, it should be verified that it is real.

⁸In the previous section we indicated Poisson's ratio with σ .

With respect to Equation (4.2.81) we note a factor of 3 is missing. This is simple to explain, given our preliminary work. In Landau's notation $\alpha \equiv \alpha_L$ is a volume expansion coefficient, that is

$$\frac{dV}{V} = \alpha_L dT \quad (4.3.11)$$

while in Braginsky's notation $\alpha \equiv \alpha_B$ is a linear expansion coefficient

$$\frac{dl}{l} = \alpha_B dT \quad (4.3.12)$$

and since

$$\frac{dV}{V} = \frac{dl^3}{l^3} = 3 \frac{dl}{l} \quad (4.3.13)$$

we see no contradiction between the two equations. In the following we will use the linear expansion coefficient, that is it should be read

$$\alpha \equiv \alpha_B \quad (4.3.14)$$

unless stated otherwise. In a gravitational wave detector the mirrors are massive objects made of high quality fused silica and coated to be highly reflective for laser light. These mirrors have linear dimensions l which are much bigger than the laser beam spot size r_0 : this justifies the half infinite approximation. Moreover, since the coating thickness d is usually much smaller than the laser beam spot size, the source term can be further simplified to

$$\alpha \vec{\nabla} u \rightarrow \alpha d \vec{\nabla} (u \delta(z - \epsilon)) \quad (4.3.15)$$

that is, it can be considered as δ -like. (ϵ is a small quantity to stress the fact that we are interested in a thin layer near $z = 0$.) Now, applying the same strategy as before, we write the solution for the displacement \vec{v} as

$$\vec{v} = \vec{v}^{(a)} + \vec{\nabla} \varphi. \quad (4.3.16)$$

It is easy to see that φ satisfies the following Poisson's equation

$$\Delta \varphi = \frac{1 + \nu}{1 - \nu} \alpha d u \delta(z - \epsilon) \quad (4.3.17)$$

without boundary conditions. The function $\vec{v}^{(a)}$ satisfies the usual elasticity equation (4.3.7) with its right hand side equal to zero, and the following boundary conditions

$$\begin{aligned} \sigma_{zz} &= \frac{E}{1 + \nu} \left(\frac{\partial^2 \varphi}{\partial y^2} + \frac{\partial^2 \varphi}{\partial x^2} \right) \Big|_{z=0} \\ \sigma_{xz} &= -\frac{E}{(1 + \nu)} \frac{\partial^2 \varphi}{\partial z \partial x} \Big|_{z=0} \\ \sigma_{yz} &= -\frac{E}{(1 + \nu)} \frac{\partial^2 \varphi}{\partial z \partial y} \Big|_{z=0}. \end{aligned} \quad (4.3.18)$$

The solution of the Poisson equation (4.3.17) is

$$\begin{aligned} \varphi(x, y, z) = & -\frac{\alpha d(1+\nu)}{4\pi(1-\nu)} \int_{-\infty}^{\infty} \int_{-\infty}^{\infty} \int_{-\infty}^{\infty} dx' dy' dz' \\ & \times \frac{u(x', y', z')(\delta(z-\epsilon) + \delta(z+\epsilon))}{\sqrt{(x-x')^2 + (y-y')^2 + (z-z')^2}}. \end{aligned}$$

Carrying out the integration over z' gives

$$\begin{aligned} \varphi(x, y, z) = & -\frac{\alpha d(1+\nu)}{4\pi(1-\nu)} \int_{-\infty}^{\infty} \int_{-\infty}^{\infty} dx' dy' \\ & \times \frac{2u(x', y', z)}{\sqrt{(x-x')^2 + (y-y')^2 + z^2}} \end{aligned} \quad (4.3.19)$$

where we added an extra δ term to enforce symmetry of the function φ . The laser beam hitting the optical component carries out a weighted measurement of the displacement of the mirror at $z = 0$ along the z -axis. Hence, what we measure is

$$\bar{X}(t) = \frac{1}{\pi r_0^2} \int_{-\infty}^{\infty} \int_{-\infty}^{\infty} dx dy e^{-(x^2+y^2)/r_0^2} \left(\frac{\partial \varphi}{\partial z} + \nu_z^{(a)} \right) \Big|_{z=0}. \quad (4.3.20)$$

In our particular case

$$\frac{\partial \varphi}{\partial z} \Big|_{z=0} = 0 \quad (4.3.21)$$

so that

$$\bar{X}(t) = \frac{1}{\pi r_0^2} \int_{-\infty}^{\infty} \int_{-\infty}^{\infty} dx dy e^{-(x^2+y^2)/r_0^2} \nu_z^{(a)} \Big|_{z=0}. \quad (4.3.22)$$

We divide the remaining work into three steps, namely:

- Compute $\sigma_{zz}|_{z=0}$.
- Compute the displacement of the surface as an average with a Gaussian weighting.
- Compute the spectrum of this displacement.

4.3.1. Computation of the stress at the free surface: $\sigma_{zz}|_{z=0}$

We substitute into the boundary condition Equation (4.3.18) the expression for φ

$$\sigma_{zz}|_{z=0} = \frac{E}{(1+\nu)} \left(-\frac{\alpha d(1+\nu)}{4\pi(1-\nu)} \right) \left(\frac{\partial^2}{\partial x^2} + \frac{\partial^2}{\partial y^2} \right) \int_{-\infty}^{\infty} \int_{-\infty}^{\infty} dx' dy' \frac{2u(x', y', 0)}{\sqrt{(x-x')^2 + (y-y')^2}}.$$

We observe that each function also depends on time: this has to be from now on explicit since at the end we will compute spectra, which are Fourier transforms of time correlation functions. We express $u(x, y, z, t)$ as the inverse Fourier transform of $\tilde{u}(k_x, k_y, k_z, \omega)$ giving

$$\begin{aligned} \sigma_{zz}|_{z=0} = & -\frac{\alpha dE}{2\pi(1-\nu)} (\partial_x^2 + \partial_y^2) \int_{-\infty}^{\infty} \int_{-\infty}^{\infty} \frac{dx' dy'}{\sqrt{(x-x')^2 + (y-y')^2}} \\ & \times \int_{-\infty}^{\infty} \int_{-\infty}^{\infty} \int_{-\infty}^{\infty} \int_{-\infty}^{\infty} \frac{d^3 k d\omega}{(2\pi)^4} \tilde{u}(k_x, k_y, k_z, \omega) e^{i\omega t + i\mathbf{k}\mathbf{r}'}. \end{aligned}$$

Using the solution of the heat equation, we find

$$\begin{aligned} \sigma_{zz}|_{z=0} = & -\frac{\alpha dE}{2\pi(1-\nu)} (\partial_x^2 + \partial_y^2) \int_{-\infty}^{\infty} \int_{-\infty}^{\infty} \frac{dx' dy'}{\sqrt{(x-x')^2 + (y-y')^2}} \\ & \times \int_{-\infty}^{\infty} \int_{-\infty}^{\infty} \int_{-\infty}^{\infty} \int_{-\infty}^{\infty} \frac{d^3 k d\omega}{(2\pi)^4} \frac{\tilde{F}(k_x, k_y, k_z, \omega)}{a^2(\mathbf{k})^2 + i\omega} e^{-i\mathbf{k}\mathbf{r}} e^{i\mathbf{k}\mathbf{r}'} e^{i\omega t + i\mathbf{k}\mathbf{r}'}. \end{aligned}$$

Taking the integrals over the plane $z = 0$ gives

$$\begin{aligned} \sigma_{zz}|_{z=0} = & -\frac{\alpha dE}{2\pi(1-\nu)} (\partial_x^2 + \partial_y^2) \int_{-\infty}^{\infty} \int_{-\infty}^{\infty} \int_{-\infty}^{\infty} \int_{-\infty}^{\infty} \frac{d^3 k d\omega}{(2\pi)^4} \frac{\tilde{F}(k_x, k_y, k_z, \omega)}{a^2(\mathbf{k})^2 + i\omega} e^{i\omega t + i\mathbf{k}\mathbf{r}} I_1 \\ I_1 \equiv & \int_{-\infty}^{\infty} \int_{-\infty}^{\infty} \frac{dx' dy'}{\sqrt{(x-x')^2 + (y-y')^2}} e^{i\mathbf{k}(\mathbf{r}' - \mathbf{r})}. \end{aligned}$$

The integral I_1 , once expressed in polar coordinates, turns out to be elementary:

$$I_1 = \frac{2\pi}{k_{\perp}} \quad (4.3.23)$$

where

$$k_{\perp} \equiv \sqrt{k_x^2 + k_y^2}. \quad (4.3.24)$$

so that, we have

$$\begin{aligned} \sigma_{zz}|_{z=0} = & -\frac{\alpha dE}{(1-\nu)} \int_{-\infty}^{\infty} \int_{-\infty}^{\infty} \int_{-\infty}^{\infty} \int_{-\infty}^{\infty} \frac{d^3 k d\omega}{(2\pi)^4} \frac{1}{k_{\perp}} \frac{\tilde{F}(k_x, k_y, k_z, \omega)}{a^2(\mathbf{k})^2 + i\omega} (\partial_x^2 + \partial_y^2) e^{i\omega t + i\mathbf{k}\mathbf{r}} \\ = & \frac{\alpha dE}{(1-\nu)} \int_{-\infty}^{\infty} \int_{-\infty}^{\infty} \int_{-\infty}^{\infty} \int_{-\infty}^{\infty} \frac{d^3 k d\omega}{(2\pi)^4} \frac{k_{\perp} \tilde{F}(k_x, k_y, k_z, \omega)}{a^2(\mathbf{k})^2 + i\omega} e^{i\omega t + i\mathbf{k}\mathbf{r}}. \end{aligned}$$

4.3.2. Computation of the displacement of the free surface: $\bar{X}(t)$

$$\begin{aligned}
 \bar{X}(t) &= \frac{1}{\pi r_0^2} \int_{-\infty}^{\infty} \int_{-\infty}^{\infty} dx dy e^{-(x^2+y^2)/r_0^2} \nu_z^{(a)}(x, y, z)|_{z=0} \\
 &= \frac{1-\nu^2}{\pi^2 E r_0^2} \int_{-\infty}^{\infty} \int_{-\infty}^{\infty} dx dy e^{-(x^2+y^2)/r_0^2} \int_{-\infty}^{\infty} \int_{-\infty}^{\infty} dx' dy' \frac{\sigma_{zz}(x', y', z')|_{z'=0}}{\sqrt{(x-x')^2 + (y-y')^2}} \\
 &= \frac{2(1+\nu)\alpha d E}{E \pi r_0^2} \int_{-\infty}^{\infty} \int_{-\infty}^{\infty} \int_{-\infty}^{\infty} \int_{-\infty}^{\infty} \frac{d^3 k d\omega}{(2\pi)^4} \frac{\tilde{F}(\mathbf{k}, \omega)}{a^2(\mathbf{k})^2 + i\omega} e^{i\omega t} I_2
 \end{aligned}$$

where we introduced

$$I_2 \equiv \int_{-\infty}^{\infty} \int_{-\infty}^{\infty} dx dy e^{i\mathbf{k}\mathbf{r}} e^{-(x^2+y^2)/r_0^2}.$$

I_2 is also a standard integral which turns out to be

$$I_2 = \pi r_0^2 e^{-k_{\perp}^2 r_0^2/4}.$$

We can now express $\bar{X}(t)$ and its complex conjugate in a form suitable for the following calculations:

$$\begin{aligned}
 \bar{X}(t) &= 2\alpha d(1+\nu) \int_{-\infty}^{\infty} \int_{-\infty}^{\infty} \int_{-\infty}^{\infty} \int_{-\infty}^{\infty} \frac{d^3 k d\omega}{(2\pi)^4} \frac{\tilde{F}(\mathbf{k}, \omega)}{a^2(\mathbf{k})^2 + i\omega} e^{i\omega t - k_{\perp}^2 r_0^2/4} \\
 \bar{X}^*(t+\tau) &= 2\alpha d(1+\nu) \int_{-\infty}^{\infty} \int_{-\infty}^{\infty} \int_{-\infty}^{\infty} \int_{-\infty}^{\infty} \frac{d^3 k_1 d\omega_1}{(2\pi)^4} \frac{\tilde{F}^*(\mathbf{k}_1, \omega_1)}{a^2(\mathbf{k}_1)^2 - i\omega_1} e^{-i\omega_1(t+\tau) - k_{\perp}^2 r_0^2/4}.
 \end{aligned} \tag{4.3.25}$$

4.3.3. Computation of the spectrum of the thermoelastic noise

We introduce the two-time correlation function as

$$B(\tau) \equiv \langle \bar{X}(t) \bar{X}^*(t+\tau) \rangle. \tag{4.3.26}$$

By direct substitution of Equation (4.3.25) into Equation (4.3.26) we have

$$\begin{aligned}
 B(\tau) &= 4\alpha^2 d^2 (1+\nu)^2 \int_{-\infty}^{\infty} \int_{-\infty}^{\infty} \int_{-\infty}^{\infty} \int_{-\infty}^{\infty} \frac{d^3 k d\omega}{(2\pi)^4} \frac{e^{-i\omega\tau - k_{\perp}^2 r_0^2/2}}{|a^2(\mathbf{k})^2|^2 + \omega^2} |\mathbf{k}|^2 2F_0^2 T_0^2 \\
 &= \int_{-\infty}^{\infty} \frac{d\omega}{2\pi} e^{-i\omega\tau} \left[8\alpha^2 d^2 (1+\nu)^2 \int_{-\infty}^{\infty} \int_{-\infty}^{\infty} \int_{-\infty}^{\infty} \frac{d^3 k}{(2\pi)^3} e^{-k_{\perp}^2 r_0^2/2} |\mathbf{k}|^2 \frac{F_0^2 T_0^2}{|a^2(\mathbf{k})^2|^2 + \omega^2} \right].
 \end{aligned} \tag{4.3.27}$$

The quantity in square brackets is called the two-sided spectral density. That is

$$B(\tau) \equiv \int_{-\infty}^{\infty} \frac{d\omega}{2\pi} e^{-i\omega\tau} S^{\text{two-sided}}(\omega) \quad (4.3.28)$$

If we choose to integrate only over positive ω we are left with the one-sided spectral density, which is a quantity closer to the directly measurable ones (by means of a spectrum analyzer for example). This means we can define another quantity, $S^{\text{one-sided}}(\omega)$, as

$$B(\tau) \equiv \int_0^{\infty} \frac{d\omega}{2\pi} e^{-i\omega\tau} S^{\text{one-sided}}(\omega). \quad (4.3.29)$$

In our case

$$S^{\text{one-sided}}(\omega) = 16\alpha^2 d^2 (1+\nu)^2 \int_{-\infty}^{\infty} \int_{-\infty}^{\infty} \int_{-\infty}^{\infty} \frac{d^3 k}{(2\pi)^3} e^{-k_{\perp}^2 r_0^2/2} |\mathbf{k}|^2 \frac{F_0^2 T_0^2}{|a^2(\mathbf{k})|^2 + \omega^2}. \quad (4.3.30)$$

Moving to cylindrical coordinates, with the z -axis as the cylinder axis, we have

$$S(\omega) \equiv S^{\text{one-sided}}(\omega) = \frac{4\alpha^2 d^2 (1+\nu)^2 F_0^2 T_0^2}{\pi^2} \int_{-\infty}^{\infty} \int_0^{\infty} \frac{dk_z dk_{\perp} 2k_{\perp}}{2} \frac{|\mathbf{k}|^2 e^{-r_0^2 k_{\perp}^2/2}}{|a^2(\mathbf{k})|^2 + \omega^2}. \quad (4.3.31)$$

We use the condition

$$\omega \ll \frac{a^2}{r_0^2} \quad (4.3.32)$$

and the fact that, since the z dimension is much smaller than the other two we have

$$k^2 \approx k_z^2. \quad (4.3.33)$$

Within these two approximations the last two integrals we have to compute decouple from each other, and taking the integral over k_{\perp} we are left with

$$\begin{aligned} S(\omega) &= \frac{2\alpha^2 d^2 (1+\nu)^2 F_0^2 T_0^2}{\pi^2} \int_{-\infty}^{\infty} dk_z \frac{k_z^2}{a^4 k_z^4 + \omega^2} \frac{2}{r_0^2} \\ &= \frac{4\alpha^2 d^2 (1+\nu)^2 F_0^2 T_0^2}{\pi^2 r_0^2} (2I_3). \end{aligned} \quad (4.3.34)$$

The last integral is also a standard one ⁹:

$$I_3 \equiv \int_0^{\infty} dk_z \frac{k_z^2}{a^4 k_z^4 + \omega^2} = \frac{\pi}{4\omega^2} \sqrt[4]{\frac{4\omega^6}{a^{12}}}. \quad (4.3.35)$$

After a little algebra we can finally write the spectrum of the thermoelastic noise as

$$S(\omega) = \frac{4\sqrt{2}(1+\nu)^2}{\pi} \frac{\alpha^2 d^2 k_B T^2}{r_0^2 \sqrt{\rho C \kappa \omega}}. \quad (4.3.36)$$

⁹This integral given in Gradshteyn's book [16] is in our opinion incorrectly calculated. Another book of integrals, albeit an older one, by Gröbner [17] gives the correct result.

4.3.4. Interpretation of equation (4.3.36)

While being correct, the expression we derived for the spectrum of the thermoelastic noise, Equation (4.3.36) needs to be further analyzed before we can substitute numerical values in it. Note that the given equation refers to an homogeneous body, whose surface, due to temperature fluctuations, moves.

If the free surface of the body is coated with a material whose parameters coincide with the bulk's ones except for the linear expansion coefficient, then we simply have to use a new linear expansion coefficient in the formula given by:

$$\alpha = \alpha_{\text{layer}} - \alpha_{\text{bulk}} \quad (4.3.37)$$

where α_{layer} and α_{bulk} are the linear expansion coefficients of the coating and of the bulk, respectively. If Poisson's ratio ν and Young modulus E are also distinct between coating and substrate, then we should proceed as follows: We recall here Equation (4.2.81) and express it in Braginsky's notation

$$\frac{E}{1-2\nu} \left[\frac{(1-\nu)}{1+\nu} \vec{\nabla} \vec{\nabla} \vec{v} - \frac{1-2\nu}{2(1+\nu)} \vec{\nabla} \times (\vec{\nabla} \times \vec{v}) \right] = \frac{E}{1-2\nu} \alpha \vec{\nabla} u \quad (4.3.38)$$

In the case in which the coating is very thin with respect to the other geometrical dimensions of the body, the elastic properties are given by the bulk, while the coating's parameter determines the "source term" responsible for the stresses induced by the temperature fluctuations. Practically this means that the coefficient appearing on both sides of this equation are numerically no longer identical, as the one on the left hand side is related to the bulk, and the one on the right hand side is related to the coating:

$$\left(\frac{E}{1-2\nu} \right)_{\text{bulk}} \left[\frac{(1-\nu)}{1+\nu} \vec{\nabla} \vec{\nabla} \vec{v} - \frac{1-2\nu}{2(1+\nu)} \vec{\nabla} \times (\vec{\nabla} \times \vec{v}) \right] = \left(\frac{E}{1-2\nu} \alpha \right)_{\text{layer}} \vec{\nabla} u.$$

Multiplying both sides by $(\frac{1-2\nu}{E})_{\text{bulk}}$ we have

$$\frac{1-\nu}{1+\nu} \vec{\nabla} \vec{\nabla} \vec{v} - \frac{1-2\nu}{2(1+\nu)} \vec{\nabla} \times (\vec{\nabla} \times \vec{v}) = \left(\frac{1-2\nu}{E} \right)_{\text{bulk}} \left(\frac{E}{1-2\nu} \alpha \right)_{\text{layer}} \vec{\nabla} u.$$

We see that considering a thin coating whose parameters are different from that of the bulk leads us to employ a new linear expansion coefficient given by

$$\alpha = (\alpha_{\text{layer}})_{\text{modified}} - \alpha_{\text{bulk}} = \left(\frac{1-2\nu}{E} \right)_{\text{bulk}} \left(\frac{E}{1-2\nu} \right)_{\text{layer}} \alpha_{\text{layer}} - \alpha_{\text{bulk}}. \quad (4.3.39)$$

The very last step consists of taking into account that coatings are usually made by a sequence of alternating layers. In this case the modified linear expansion coefficient for the layer we found becomes a sum of two contributions weighted by the relative length of each of the two components: if we label these two components with indices 1, 2 then we can write

$$\alpha = \frac{\alpha_1 d_1}{d_1 + d_2} \frac{E_1(1-2\nu_1)}{E(1-2\nu_1)} + \frac{\alpha_2 d_2}{d_1 + d_2} \frac{E_2(1-2\nu_2)}{E(1-2\nu_2)} - \alpha_{\text{bulk}} \quad (4.3.40)$$

where d_1, d_2 are the total lengths of layer number 1 and 2, respectively.

4.4. Photo-thermal noise

As we did for the thermoelastic noise, we *closely* follow Braginsky's work [2], adding some more hints about the explicit calculations involved.

The photo-thermal noise is the result of a two-step process. First photons are absorbed within the optical material giving rise to thermal phonons. After a very short time the thermal phonons are absorbed as well, resulting in a local jump in temperature. Here we will give a derivation of the noise spectral density without resorting to the full elasticity theory framework: it can be shown that the differences are minor and it is possible to carry out the full calculation just as we did for the thermoelastic noise. The body is considered as semi infinite. The reference system is chosen so that its free surface (that which is hit by the laser radiation) is identified by the plane $x = 0$, and the body occupies the region $x \geq 0$. We start with a heat equation with a source term (on its left hand side):

$$\frac{\partial u(x, t)}{\partial t} - a^2 \frac{\partial^2 u(x, t)}{\partial x^2} = \frac{w(t)}{\rho C \pi r_0^2} 2\delta(x). \quad (4.4.1)$$

The boundary condition is

$$\left. \frac{\partial u(x, t)}{\partial x} \right|_{x=0} = 0 \quad (4.4.2)$$

where

$$a^2 \equiv \frac{\lambda^*}{\rho C} \quad (4.4.3)$$

and where λ^* is the thermal conductivity, ρ is the material density and C is the specific heat capacity. The source term is different from the one used in the study of the thermoelastic noise. The physical reason is that the source term, which is ultimately responsible for the noise, is now a simple function of the material constants of the body and the rate of absorbed photons which we wrote as $w(t)$, and which is quantitatively defined by the following relations:

$$\langle w(t)w^*(t_1) \rangle = \hbar\omega_0 W_0 \delta(t - t_1) \quad (4.4.4)$$

$$w(t) = W_{abs}(t) - \langle W_{abs}(t) \rangle \equiv W_{abs}(t) - W_0 \quad (4.4.5)$$

where W_0 is the mean absorbed power, $W_{abs}(t)$ is the absorbed power at an instant t , ω_0 is the laser angular frequency (that is the angular frequency of the absorbed photons) and r_0 is the laser beam radius. The quantity whose spectral density we are interested in is the one-dimensional displacement of the mirror along the x -axis: if we indicate this displacement with X_{1D} we can immediately write it as the integral of the temperature along the x -axis times the linear expansion coefficient α

$$X_{1D} = \alpha \int_0^\infty dx u(x, t). \quad (4.4.6)$$

If we indicate with $\tilde{u}(k, \omega)$ the Fourier transform of $u(x, t)$ we can write

$$X_{1D}(t) = \alpha \int_0^\infty dx \int_{-\infty}^\infty \int_{-\infty}^\infty \frac{d\omega dk}{(2\pi)^2} e^{-i\omega t} e^{-ikx} \tilde{u}(k, \omega). \quad (4.4.7)$$

If we take the Fourier transform of the heat equation we get the following expression for $\tilde{u}(k, \omega)$

$$\tilde{u}(k, \omega) = \frac{\tilde{w}(\omega)}{(\rho C \pi r_0^2)(a^2 k^2 + i\omega)} \quad (4.4.8)$$

where $\tilde{w}(\omega)$ is the Fourier transform of $w(t)$. Plugging this expression for $\tilde{u}(k, \omega)$ into (4.4.7) we have

$$\begin{aligned} X_{1D}(t) &= \frac{\alpha}{\rho C \pi r_0^2} \int_{-\infty}^{\infty} \int_{-\infty}^{\infty} \frac{d\omega dk}{(2\pi)^2} e^{-i\omega t} \frac{\tilde{w}(\omega)}{a^2 k^2 + i\omega} \int_0^{\infty} dx e^{-ikx} \\ &= \frac{\alpha}{\rho C \pi r_0^2} \int_{-\infty}^{\infty} \int_{-\infty}^{\infty} \frac{d\omega dk}{(2\pi)^2} e^{-i\omega t} \frac{\tilde{w}(\omega)}{a^2 k^2 + i\omega} \frac{1}{2} (2\pi \delta(k)) \\ &= \frac{\alpha}{2\rho C \pi r_0^2} \int_{-\infty}^{\infty} \frac{d\omega}{2\pi} e^{-i\omega t} \frac{\tilde{w}(\omega)}{i\omega}. \end{aligned} \quad (4.4.9)$$

Its complex conjugate is¹⁰

$$X_{1D}^*(t_1) = \frac{\alpha}{2\rho C \pi r_0^2} \int_{-\infty}^{\infty} \frac{d\omega_1}{2\pi} e^{i\omega_1 t_1} \frac{\tilde{w}^*(\omega_1)}{(-i\omega_1)}. \quad (4.4.10)$$

The two-time correlation function is

$$\begin{aligned} \langle X_{1D}(t) X_{1D}^*(t_1) \rangle &= \frac{\alpha^2}{4(\rho C \pi r_0^2)^2} \int_{-\infty}^{\infty} \frac{d\omega_1}{2\pi} \int_{-\infty}^{\infty} \frac{d\omega}{2\pi} e^{-i\omega t - i\omega_1 t_1} \frac{\langle \tilde{w}(\omega) \tilde{w}^*(\omega_1) \rangle}{\omega^2} \\ &= \frac{\alpha^2}{4(\rho C \pi r_0^2)^2} \hbar \omega_0 W_0 \int_{-\infty}^{\infty} \frac{d\omega}{2\pi} \frac{e^{-i\omega(t-t_1)}}{\omega^2} \equiv B(t-t_1) \end{aligned} \quad (4.4.11)$$

where we used the defining property of $w(\omega)$. The *two-sided* spectral density is the Fourier transform of the two-time correlation function, so

$$B(t) \equiv \int_{-\infty}^{\infty} \frac{d\omega}{2\pi} e^{-i\omega t} S^{\text{two-sided}}(\omega). \quad (4.4.12)$$

The *one-sided* spectral density is similarly defined: the only difference is that the integral is only over positive frequencies. In this case

$$B(t) \equiv \int_0^{\infty} \frac{d\omega}{2\pi} e^{-i\omega t} S^{\text{one-sided}}(\omega). \quad (4.4.13)$$

Since the one-sided spectral density is the one more directly measurable, e.g. by means of a spectrum analyzer, we have

$$S_{PT}(\omega) \equiv S^{\text{one-sided}}(\omega) = 2S^{\text{two-sided}}(\omega) = \frac{2\alpha^2 \hbar \omega_0 W_0}{(\rho C \pi r_0^2)^2 \omega^2} \quad (4.4.14)$$

¹⁰We have to explicitly check at the end of the calculation that physical quantities are actually real quantities as they should be.

4.5. Quantitative comparison between the different thermal noise effects

After the theoretical derivation of the expression for coating thermal noise due to thermodynamic temperature fluctuations and to photon absorption, we turn our attention to the comparison between the four types of noise. Their analytical expressions are [2, 4]

$$\begin{aligned}
 S_{TE}(\omega) &= \frac{4\sqrt{2}(1+\nu)^2 \alpha^2 d^2 k_B T^2}{\pi r_0^2 \sqrt{\kappa \rho C \omega}} \\
 S_{PT}(\omega) &= 2\alpha^2 \frac{\hbar \omega_0 W_0}{(\rho C \pi r_0^2)^2 \omega^2} \\
 S_{TR}(\omega) &= \frac{\beta^2 \lambda^2 k_B T^2}{\pi r_0^2 \sqrt{\rho C \kappa} \sqrt{\omega}} \\
 S_{BN}(\omega) &= \frac{4k_B T(1-\nu^2)\phi}{\omega \sqrt{2\pi} E r_0}
 \end{aligned} \tag{4.5.1}$$

where S_{TE} is thermoelastic noise, S_{PT} is photo-thermal noise, S_{TR} is thermorefractive noise, and S_{BN} is Brownian noise. The parameters appearing in these formulas are listed and discussed in Appendix A. We can see in Figure 4.1 that the expected noises

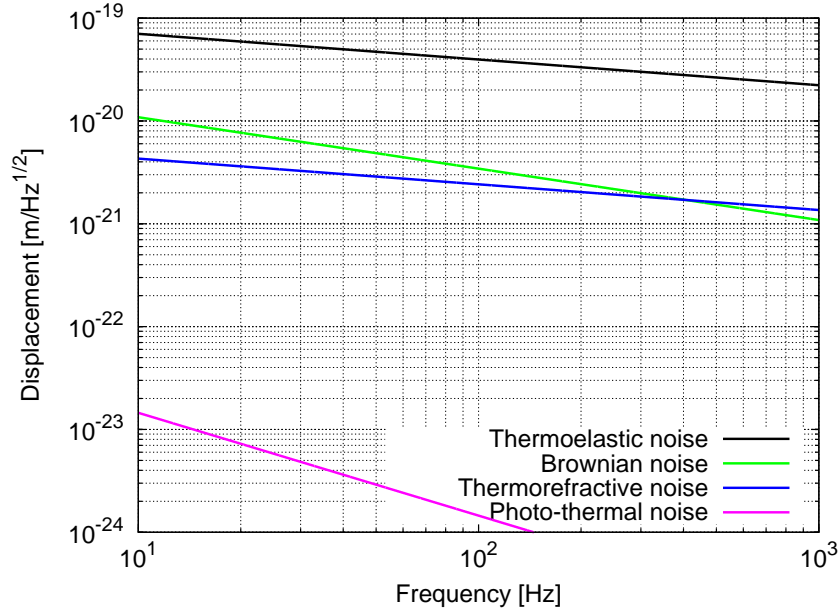


Figure 4.1.: Quantitative comparison of the four different thermal noises. For each noise the *square root of the spectral density* is plotted, which is the quantity directly comparable with experiment. The parameters are the those given by Braginsky [4]: in particular the beam radius is $r_0 = 6 \cdot 10^{-2}$ m.

sources produce very small displacements. One parameter which can be changed in order

to produce bigger noises is the beam radius r_0 . Making the beam radius a bit smaller enables us to use smaller optics.

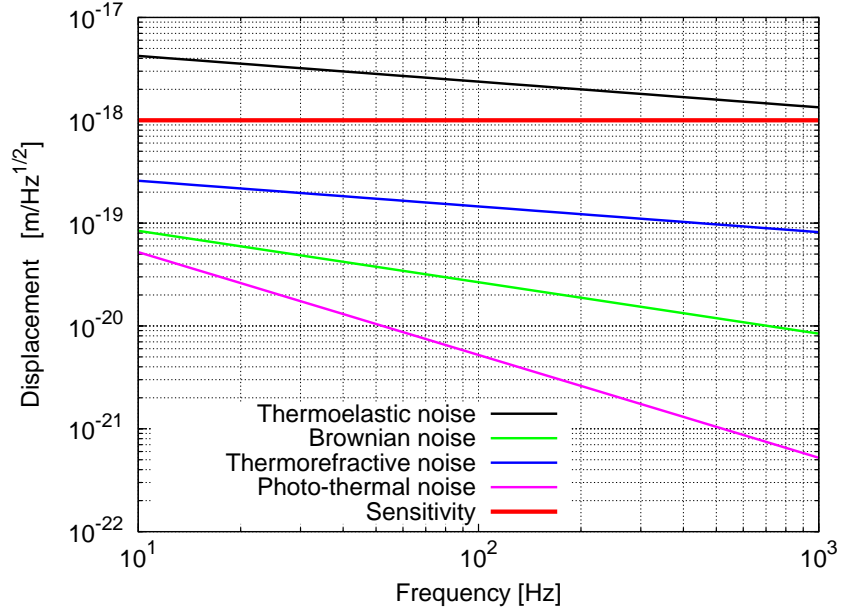


Figure 4.2.: Same plot as Figure 4.1, but using a smaller beam radius, $r_0 = 10^{-3}$ m . The noises are in this case bigger, so that at least one of them can be measured in a small scale experiment: the red line labeled “Sensitivity” sets the sensitivity level required for such a goal.

Figure 4.2 shows the sensitivity level we must achieve to be able to see at least one kind of thermal noise. This sensitivity will be the most important design parameter for the internal thermal noise experiment which we will draft in the following chapter.

5. Toward internal thermal noise measurement

5.1. Shaping the experiment around the required sensitivity

In the previous chapter we obtained an estimate for the length noise produced by internal thermal noise. In order to carry out such a measurement we found that a sensitivity of

$$\Delta l = 10^{-18} \frac{\text{m}}{\sqrt{\text{Hz}}} \quad (5.1.1)$$

is required. This quantity affects the experimental setup in each of its subsystems, which are:

- The laser¹.
- The resonator² which reacts to the internal thermal noise altering its transmission and reflection.
- The readout system which is basically composed of a photodiode converting the reflected or transmitted light into a current, and an electronic device which analyzes the electrical signal.

In this case, the length noise of the resonator (which is the physical quantity we want to measure) and the frequency noise are related to each other³ by the following relation:

$$\frac{\Delta f}{f_0} = \frac{\Delta l}{l_0} \quad (5.1.2)$$

where

- l_0 is the length of the resonator.
- f_0 is the laser frequency.
- $\Delta f, \Delta l$ are the frequency and length noises respectively.

¹We will always refer in the following to a Nd:YAG laser running at the wavelength $\lambda = 1064$ nm: this laser system is the standard in GW research.

²A resonator is a standard tool in optics, see for example [18].

³This relationship between Δl and Δf enable us to consider a length variation as a frequency variation, and vice versa.

If we choose a small resonator (i.e. if l_0 is small), we can convert a small length change into a relatively large frequency change that can be measured.

Since we are interested in measuring the coating thermal noise, it makes sense to employ a small device where the coating should be responsible for most of the noise.

An etalon coated on a standard one inch optical substrate is a sensible choice since by choosing a reasonably small length we can convert length noise into frequency noise which can be detected.

An important issue has to be stressed: if the coating thermal noise results in a coherent displacement of both of the etalon's surfaces, we will get very little signal if any at all. We must state that the effect of the etalon on the theory we developed and on the size of the expected signal is not yet known. The employment of an etalon seemed to us the only way to measure internal thermal noise in a table-top experiment. In other words: the discrepancy between the theory developed in the last chapter for a coated substrate and the measurement's results were one of the goals of the experiment.

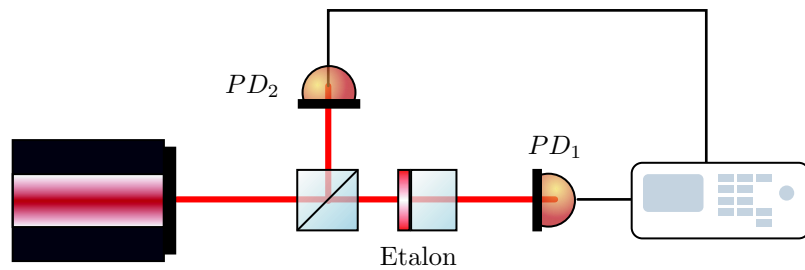


Figure 5.1.: The experimental setup: a laser beam is sent to the etalon. The transmitted light power is measured by the photodiode PD_1 , while the photodiode PD_2 measures the incident light power. The two signals are then analyzed by a spectrum analyzer. (The laser has to be intensity- and frequency-stabilized.)

That being said, the experimental setup is in principle very simple: given an etalon resonant with the laser frequency, we can measure the transmitted light intensity by means of a photodiode. This electric signal will carry the information about the length noise, in addition to a number of noise sources that need to be kept to a minimum. We will then establish the main etalon's features:

- Length: l_0
- Optical response function.

Regarding the length, we need a very short etalon. Since the etalon sits between two high reflectivity coatings, we need to make this distance much larger than the length of a single coating layer. Since the single layers have lengths of $l = \frac{\lambda}{4}$ where λ is the laser wavelength, we choose the etalon's *optical length* to be

$$l_0 = 10\lambda \approx 10 \mu\text{m}. \quad (5.1.3)$$

The optical response function should be as steep as possible: that is, the etalon should react to small length variations (driven by internal thermal noise) with big changes of transmitted light power. In the next section we will set the relevant parameters that have to be met by the company that actually produce the etalon, and find out the *optimal working point* that will give us the largest variation of the transmitted light power per unit length change.

5.1.1. Calibration issues

The calibration of the results can be easily done by analyzing the etalon's transmission profile near the selected working point. This can be done in two ways: by changing the laser frequency and by changing the optical length by a known amount. The former method is achieved by acting on the laser crystal piezo itself, the latter by tilting the etalon.

5.2. Tight constraints on the etalon

We review here the basic etalon's theory and we give constraints on etalon's parameters which have to be met in order to be able to reach the sensitivity goal.

The etalon's basic theory is well known [19]: it is a direct consequence of the interference of light. Let's consider an etalon of thickness d and refraction index is n : its optical length is then

$$l = nd. \quad (5.2.1)$$

If we illuminate it with laser light of wavelength λ , then the reflected and transmitted light will depend on the length difference

$$\Delta s = 2d\sqrt{n^2 - \sin^2 \alpha}. \quad (5.2.2)$$

We indicate the transmissivity, reflectivity and losses at each of the two plane surfaces

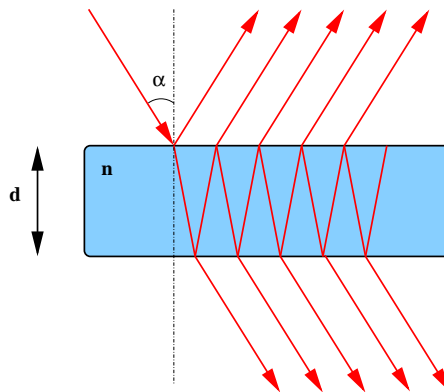


Figure 5.2.: Schematic of an etalon illuminated by a laser beam.

with T, R and A respectively. These quantities⁴ are dimensionless and constrained between 0 and 1. Conservation of energy gives

$$T + R + A = 1. \quad (5.2.3)$$

The reflected and transmitted light intensities, with respect to the incoming light inten-

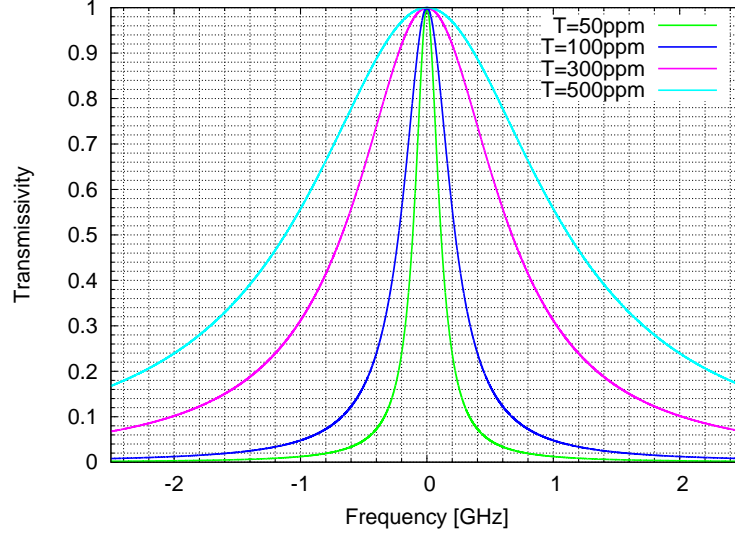


Figure 5.3.: Fraction of the transmitted power with respect to the incident power as a function of the *frequency difference* between laser frequency and etalon's resonance frequency, for different etalon's transmissivities. The incident angle is $\alpha = 0$, the optical resonator length is 10λ and we assumed no losses.

sity⁵ I_0 , can now be written as

$$I_R = I_0 R \frac{1 + (R + T)^2 - 2(R + T) \cos \Delta\phi}{1 + R^2 - 2R \cos \Delta\phi} \quad (5.2.4)$$

$$I_T = I_0 \frac{T^2}{1 + R^2 - 2R \cos \Delta\phi} \quad (5.2.5)$$

where

$$\Delta\phi = 2\pi \frac{\Delta s}{\lambda}. \quad (5.2.6)$$

The expression for the transmitted and reflected light intensity are periodic, as can be inferred by the presence of the $\cos \Delta\phi$ function. However, if we remember that the resonator is 10λ long, we find that two transmission maxima are separated in frequency by the so-called *free spectral range*, which is in our case

$$\text{FSR} = \frac{c}{2nd} \approx 15 \text{ THz}. \quad (5.2.7)$$

⁴ T, R and A are transmissivity, reflectivity and losses with respect to laser *power*. We will use for T, R and A the suffix ppm which means *part per million*.

⁵In this work we used I_0 for both the incoming light intensity and for the maximal measured photocurrent (later in the text). It should be easy, by means of a dimensional analysis, to distinguish between the two meanings.

This means the resonant condition has to be achieved with very good precision, since the resonator length cannot be changed after its production and since it is not possible to scan the laser frequency over such a range⁶. In Figure 5.3 we show the etalon's transmissivity as a function of the laser frequency according to different values of T . (We assumed *no losses*.)

As we already said, the etalon should react to small variation of its length with big variation of its reflectivity. The length sensitivity target given by Equation (5.1.1) can be expressed, by using Equation (5.1.2) as a frequency target Δf

$$\Delta f \approx 30 \frac{\text{Hz}}{\sqrt{\text{Hz}}}. \quad (5.2.8)$$

If we now set the incoming laser power to $P_0 = 1 \text{ mW}$ in order not to damage the etalon, we immediately find out that our shot noise level for a photocurrent measurement is (see Appendix B)

$$I_{shot} = 12.6 \frac{\text{pA}}{\sqrt{\text{Hz}}} \quad (5.2.9)$$

usually one requires the actual measure to be considerably bigger than the shot noise,

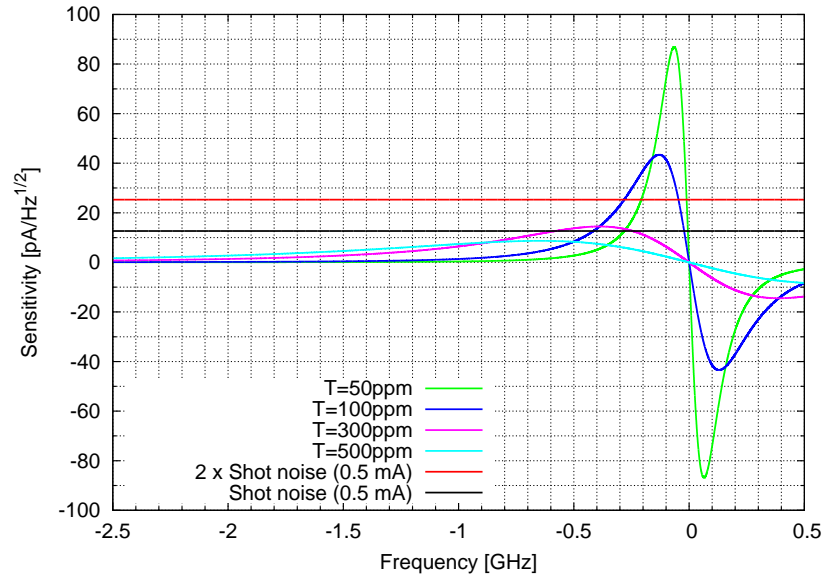


Figure 5.4.: Graph of the etalon sensitivity $S(f)$ as a function of f , for different values for T . No losses are here assumed ($A = 0$).

which means having an acceptable *signal to noise ratio*. Requiring our signal to be two times bigger than the shot noise level we then must have

$$I_{signal} = 2I_{shot} = 25.2 \frac{\text{pA}}{\sqrt{\text{Hz}}} \quad (5.2.10)$$

If we now

⁶The laser frequency can be tuned at most by 15 GHz by acting on the laser crystal temperature (from the laser producer's web site <http://innolight.de>).

5. Toward internal thermal noise measurement

- take the derivative of I_T/I_0 with respect to the frequency
- normalize this quantity to a maximal measured photocurrent (see Appendix B) of 0.5 mA
- multiply the result by the expected frequency noise we want to detect, which is $\Delta f \approx 30 \frac{\text{Hz}}{\sqrt{\text{Hz}}}$

we finally obtain the etalon's sensitivity $S(f)$ as a function of the frequency difference between the laser frequency and the etalon's resonance frequency. It is easy to see that the sensitivity $S(f)$ has dimensions of

$$[S(f)] = \frac{\text{A}}{\sqrt{\text{Hz}}} \quad (5.2.11)$$

and can therefore be directly compared with I_{shot} and I_{signal} . The condition that has to be fulfilled is

$$|S(f)| \geq I_{signal} \quad (5.2.12)$$

at least for some frequencies f . In Figures 5.4, 5.5 and 5.6 we clearly see that the required transmissivity at each etalon surface should be

$$T \approx 100 \text{ ppm} \quad (5.2.13)$$

and the losses

$$A \approx 10 \text{ ppm} \quad (5.2.14)$$

in order to be able to measure the internal thermal noise.

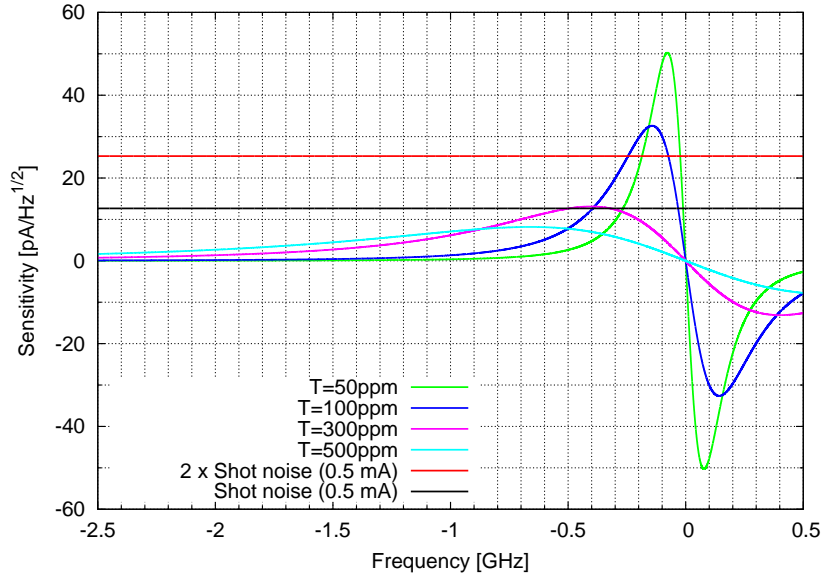


Figure 5.5.: Graph of the etalon sensitivity $S(f)$ as a function of f , for different values for T , in the case of $A = 10$ ppm.

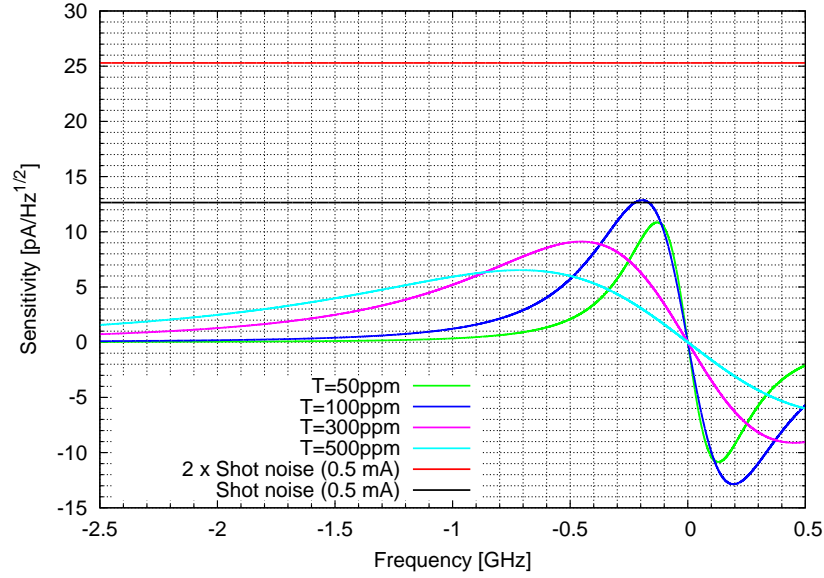


Figure 5.6.: Graph of the etalon sensitivity $S(f)$ as a function of f , for different values for T , in the case of $A = 50$ ppm

5.2.1. Etalon's internal tilt

If the two high reflectivity surfaces are tilted against each other, then the etalon's performance degrades considerably. Ideally one would keep this angle to zero, but since this is in practice not possible, an upper limit is needed to the angle we can tolerate without compromising the whole experiment. To solve this problem, we employed a program for simulation of the optical system written by Roland Schilling, called WaveProp.

This program can simulate a wide range of optical systems: here it is enough to say that the program proved useful in simulating both the GEO600 interferometer (which is 600 m long) and our small etalon (which is 10 μm long). More details about the simulation program are in Appendix C. The only restriction we encountered was of a technical nature: the program ran on a high performance computer under a strict time-sharing policy. This means the simulations could take at most five minutes, and therefore we had to face some trade-offs in the choice of the parameters in order to keep the running time within the given limit. The Figures 5.7, 5.8 and 5.9 show the simulation results for the etalon with increasing tilt between its surfaces. Given the high reflectivity, even the smallest internal angle leads to vanishing transmitted power. The simulations helped us to realize that the maximal acceptable internal angle should be much less than $\theta_{max} = 10^{-7}$ rad. This parameter is clearly beyond current coating technology. Therefore we decided to interpret this requirement in the following way: the planarity of the surfaces must be better than θ_{max} only in a small region of the optics not bigger than a few millimeters, preferably located at the center of the optical surface.

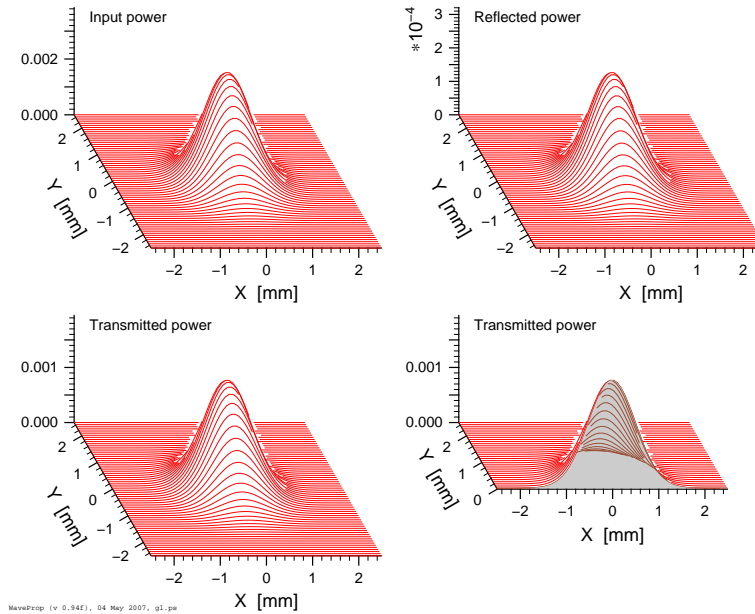


Figure 5.7.: A laser beam of 1 W and waist $w_0 = 1$ mm hits the etalon. The internal tilt is in this case $\theta = 0$. The upper left picture represents the incoming beam and the lower left the transmitted beam. (The etalon is resonant with respect to the incoming laser beam).

5.2.2. Etalon production: a challenge for thin film technology

The requirements on the etalon are *very* stringent. We state them here once more:

- A 1 inch optical substrate has to be coated with a high reflectance coating, a spacer and another high reflectance coating.
- The spacer has to be resonant for the Nd:YAG wavelength and has to be 10λ long. The resonant condition has to be nearly exactly matched since neither the etalon nor the laser are tunable over the etalon's free spectral range (which is of the order of 15 THz).
- The coatings should have a transmissivity $T \approx 100$ ppm.
- The losses A should be much less than T : $A \ll T$.
- The planarity should be better than 10^{-7} rad in a region extending a few millimeters around the center of the optical surface.

These constraints which have to be matched *independently and at the same time*, put a serious challenge on the coating companies. From a handful of companies in the whole world with the capabilities to build such a device, some of them explicitly or implicitly declined the order, leaving us with basically only one company willing to undertake the task *under best effort*. This company was the Laser Zentrum Hannover (LZH).

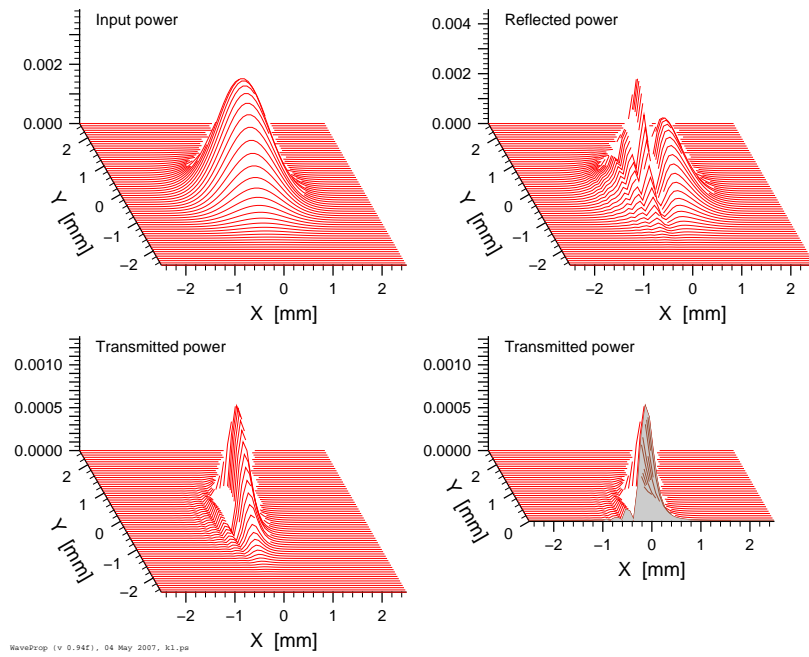


Figure 5.8.: A laser beam of 1 W and waist $w_0 = 1$ mm hits the etalon. The internal tilt is $\theta = 10^{-7}$ rad.

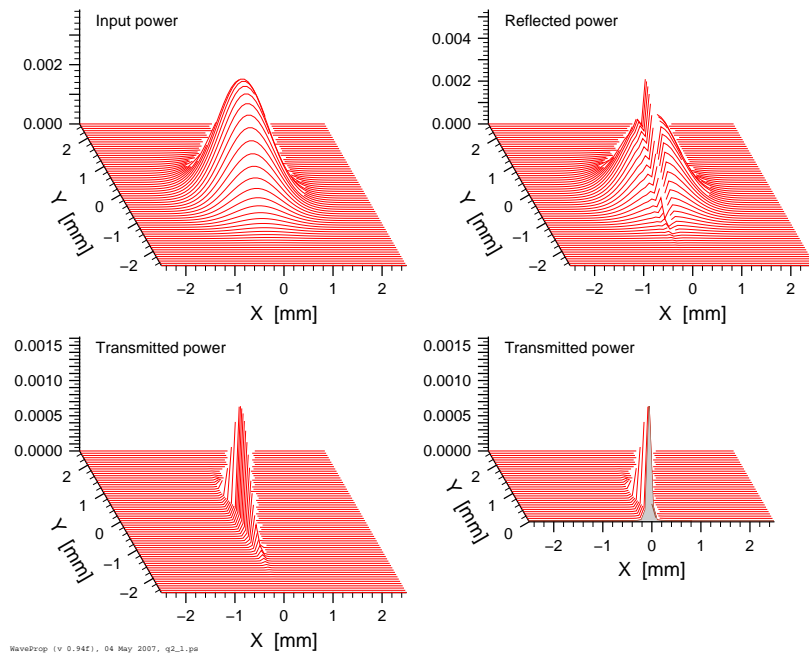


Figure 5.9.: A laser beam of 1 W and waist $w_0 = 1$ mm hits the etalon. The internal tilt is $\theta = 10^{-6}$ rad.

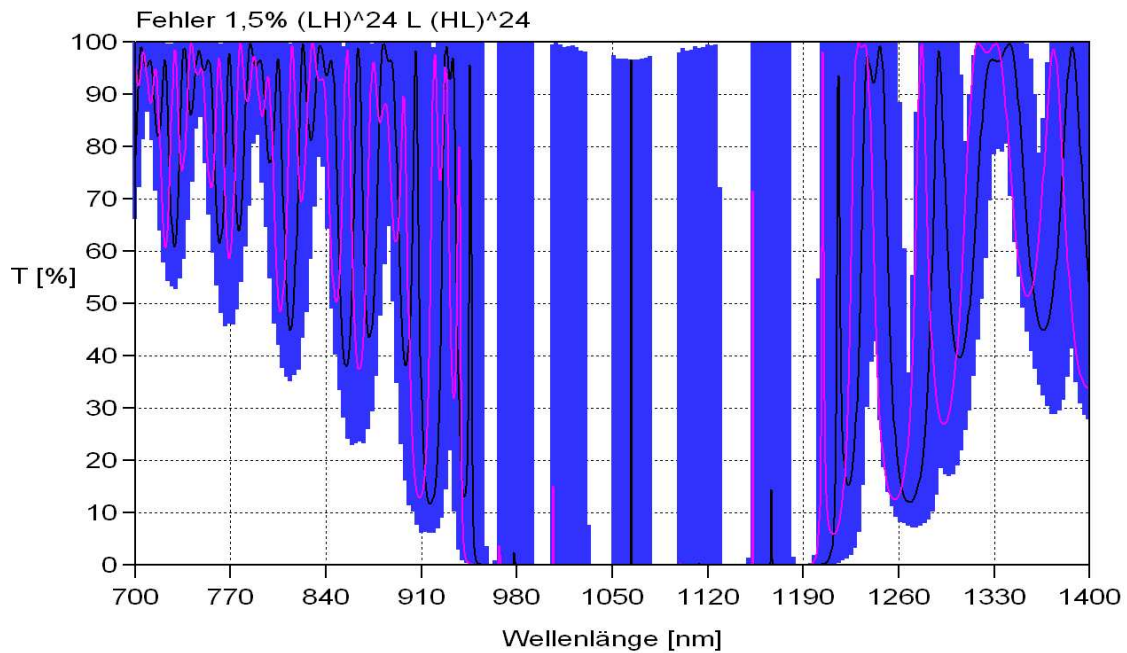


Figure 5.10.: The transmission profile as planned is shown in black. The blue region shows the errors introduced by realistic thickness variations that occur during the coating process.

5.3. Etalon performance

We got *three* deliveries of six etalons each, over a time period lasting more than two years. Unfortunately, we were *not* able to put the etalons in resonance with the laser light, and therefore we were not able to get the steep resonance signal required to measure the internal thermal noise. Quantitatively the transmitted light power was at most 2% of the incoming light power, this “maximum” happened at a significant etalon tilt with respect to the incoming laser beam (approximately 0.5 rad) and the maximum itself often showed strong asymmetry with respect to the frequency.

This poor transmissivity did not permit us to estimate the etalons’ parameters like transmissivity, losses, internal tilt and resonance frequency.

5.4. Additional etalon simulations

After the delivery of the etalons and the attempt to measure the internal thermal noise, we had the opportunity to get some additional simulations from Dr. Hung Ly. These simulations were made by using the software tools developed by LZH to actually produce the etalons themselves. In Figure 5.10 we show the transmissivity of the etalon in a wide

wavelength range. The black curve represents the planned transmissivity profile, showing the sharp maximum at 1064 nm. The blue regions show the error that would result as a consequence of coating thickness error of $\pm 1.5\%$. This means these coating thickness variations can displace the resonance far beyond the laser tunability range. It was also possible to simulate the square of the field inside the etalon, which is proportional to the power inside the etalon. This quantity is strongly dependent on interference effects which in turn dictate the overall etalon's performance. We also simulated the effect of small thickness variations in the spacer and in one of the layers which is next to the spacer. The results are shown in Figures 5.12 and 5.13. These simulations confirm the conclusions we were already able to draw: the production of such a etalon can be done only at the cutting edge of current thin film technology. Therefore the delivery of the etalons by LZH *under best effort* appears now a fully reasonable and fair decision.

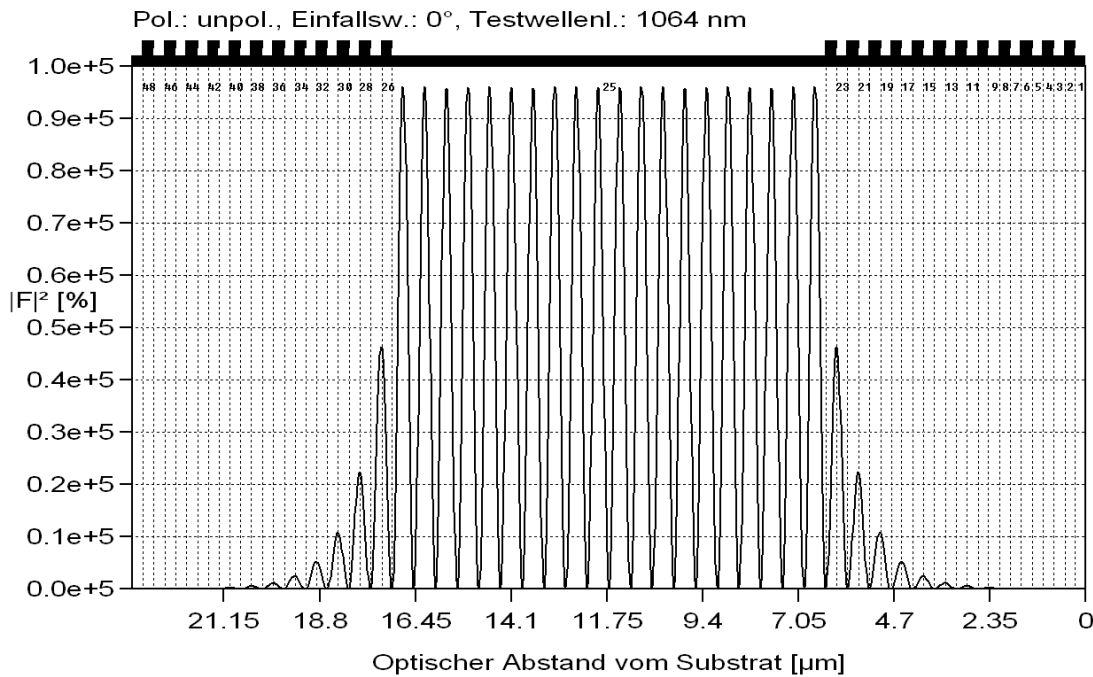


Figure 5.11.: The power intensity inside the etalon (apart from a proportionality coefficient). From right to left we clearly see the high reflectance coating as a structure of $\lambda/4$ layers with alternating materials, the spacer which is 10λ long, and another high reflectance coating.

5. Toward internal thermal noise measurement

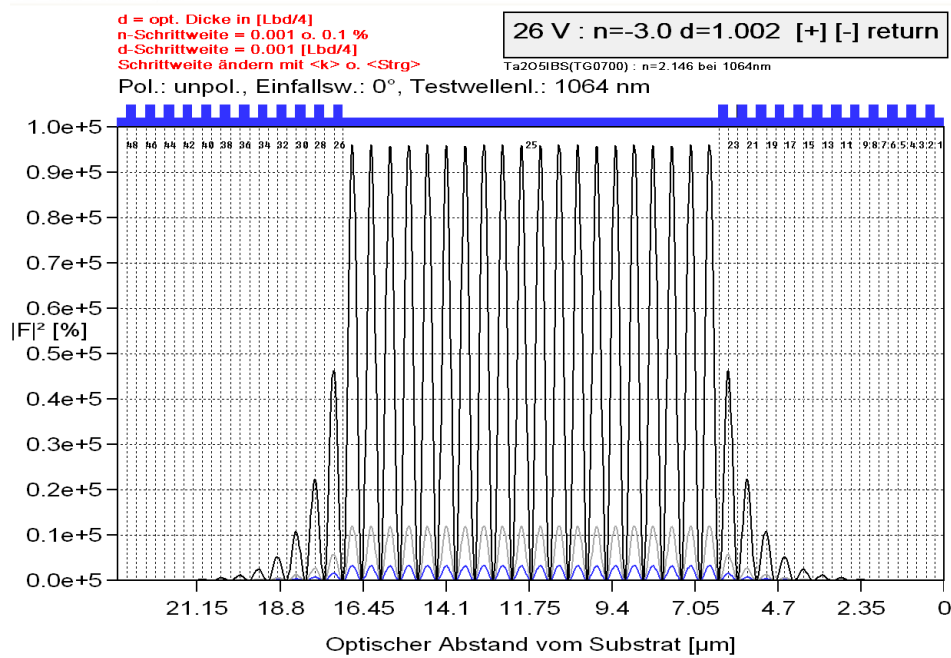


Figure 5.12.: The effect of a small thickness variation (by $\lambda/4000$) in a layer near the spacer. The effect is clearly visible.

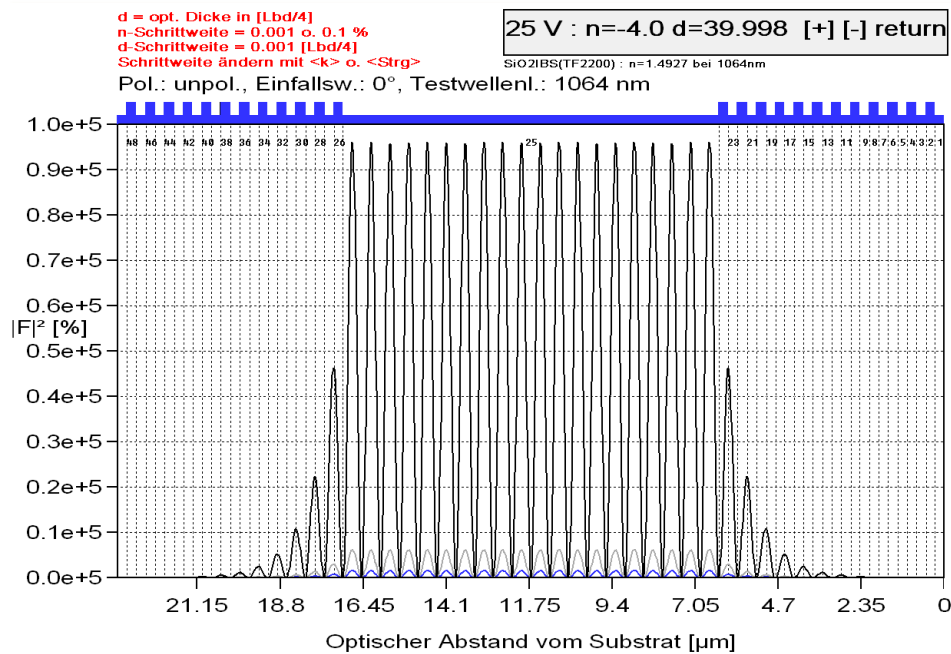


Figure 5.13.: A variation of the spacer (by $\lambda/4000$) has an even stronger effect with respect to the same variation in the nearby layer.

5.4.1. Temperature tuning

Finally we also studied the possibility to compensate small production imperfections by changing the etalon's temperature, thereby making it "longer" or "shorter". In Figure 5.14 we see that a length variation of $\lambda/4000$ either in the spacer or in the first coating layer leads to a drastic decrease of the transmissivity. Let l_1 and l_2 be the optical length of the spacer and the first coating layer, respectively. Then it is easy to see that the relative change of the optical length with respect to temperature is

$$\frac{1}{l_i} \frac{dl_i}{dT} = \alpha_i + \frac{\beta_i}{n_i} \quad (5.4.1)$$

where:

- the indexes 1 and 2 refer to the spacer and the first coating layer, respectively.
- α_i is the relative linear expansion coefficient.
- n_i is the index of refraction.
- β_i is the variation of the refractive index with respect to the temperature.

If we take the material parameters from Appendix A, we see that

$$\alpha_i \ll \beta_i \quad (5.4.2)$$

so that

$$\frac{1}{l_i} \frac{\Delta l_i}{\Delta T} \approx \frac{\beta_i}{n_i}. \quad (5.4.3)$$

A temperature variation ΔT leads to a length variation Δl_1 in the spacer and Δl_2 in the first coating layer which are

$$\Delta l_i = \frac{\beta_i l_i}{n_i} \Delta T \quad (5.4.4)$$

substituting our design parameters we observe that

$$|\beta_1 l_1| \approx |\beta_2 l_2| \quad (5.4.5)$$

and this means that we cannot "tune" the spacer without "detuning" the first coating layer. From this analysis we learned that it would be a more sensible choice to build an etalon whose spacer is made of Tantal pentoxide: in this case we would have

$$|\beta_1 l_1| \gg |\beta_2 l_2| \quad (5.4.6)$$

and the spacer would react much more than the first coating layer with respect to temperature changes, thereby giving us the possibility to "tune" it.

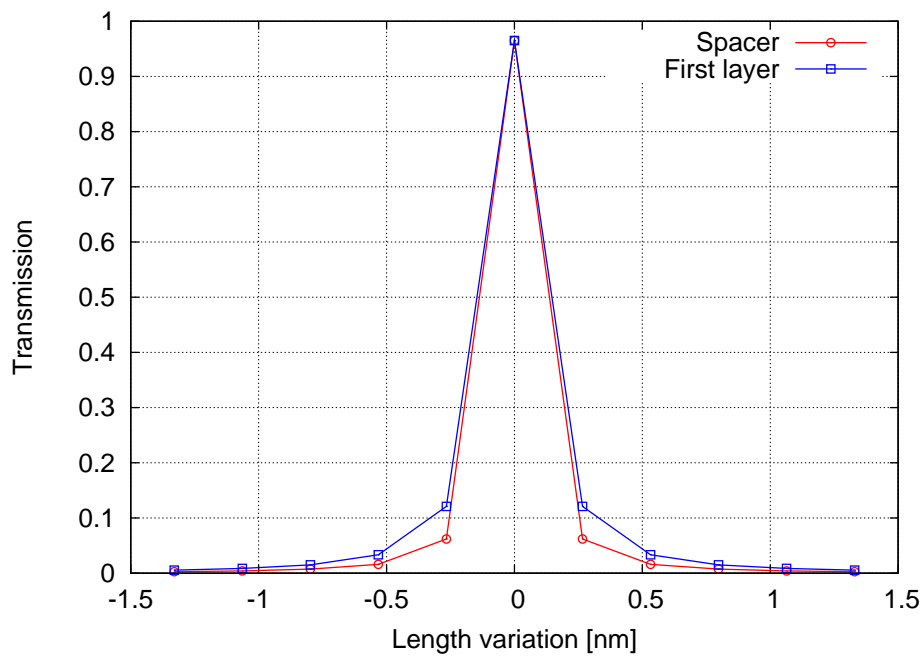


Figure 5.14.: The graph shows the variation of the etalon's transmissivity at 1064 nm as a function of small length variations in the spacer and in the first coating layer. The data points are separated by $\lambda/4000$.

6. Conclusion and outlook

In this work we showed our investigations into thermal noise as relevant for gravitational wave research. We found that, in the lower frequency band, the pendulum suspension needs to be better understood. Especially the cross coupling between the various degrees of freedom needs to be quantitatively estimated and verified by experiment. Especially interesting was the fact that changing the moments of inertia of the suspended masses caused a clear lowering of the length noise, while efforts to reduce other noise sources did not change the length noise at all. Our work in finding a model for such a complex system, could be useful as a new starting point to raise the attention of the community toward an approach which looks efficient and effective. In particular, the numerical instability of Holzer's method can be easily eliminated by using a custom numerical precision in the calculations.

Regarding internal thermal noise we can say that our plan to provide a novel setup to measure it was, and still is, a valuable one, since it aims to deliver data which provide additional information with respect to other measurement techniques already available [20].

Since the required optical component for such an experiment (the etalon) can only be produced at the highest production standard currently available, we faced here a common difficulty in gravitational wave research, namely the difficulty in obtaining optical devices which cannot be routinely produced by companies as standard goods. The result is often that these components have to be accepted by the experimentalists as produced under *best effort*, thereby leaving them with the risk of not being able to carry out the planned experiment.

Nevertheless, we do hope that this work will help the scientific community toward a better understanding of thermal noise, an issue of growing relevance for gravitational wave research.

A. Parameter list for internal thermal noise calculations

We list the parameters for the thermal noise calculations carried out in Chapter 4. Firstly we list the natural constants and other laser-related parameters.

Name	Symbol	Value	Units
Boltzmann's constant	k_B	$1.38 \cdot 10^{-23}$	JK^{-1}
Reduced Planck's constat	\hbar	$1.05 \cdot 10^{-34}$	Js
Speed of light (in vacuum)	c	$3 \cdot 10^8$	ms^{-1}
Laser wavelenght	λ	$1064 \cdot 10^{-9}$	m
Laser frequency	f_0	$2.81 \cdot 10^{14}$	Hz
Laser angular frequency	ω_0	$1.77 \cdot 10^{15}$	Hz
	π	≈ 3.14	—

Secondly we list the etalon's material parameters. The substrate material for the etalon is fused silica. The coatings are made by a combination of two materials: fused silica and Tantal pentoxide (Ta_2O_5).

The material parameters for fused silica are:

Name	Symbol	Value	Units
Thermal expansion coefficient	α	$5.5 \cdot 10^{-7}$	K^{-1}
Density	ρ	2200	kgm^{-3}
Young modulus	E	$7.2 \cdot 10^{10}$	Jm^{-3}
Thermal conductivity	k	1.4	J(mKs)^{-1}
Specific heat capacity	C	$6.7 \cdot 10^{-2}$	J(KgK)^{-1}
Poisson ratio	ν	.17	—
Angle of loss	ϕ	$5 \cdot 10^{-9}$	—
index of refraction	n	1.45	—
	β	$-1.5 \cdot 10^{-5}$	K^{-1}

The material parameters for Tantal pentoxide (Ta_2O_5) are:

Name	Symbol	Value	Units
Thermal expansion coefficient	α	$-4.4 \cdot 10^{-5}$	K^{-1}
Density	ρ	8200	kgm^{-3}
Young modulus	E	$1.4 \cdot 10^{11}$	Jm^{-3}
Poisson ratio	ν	.23	—
index of refraction	n	2.1	—
	β	$1.21 \cdot 10^{-4}$	K^{-1}

A. Parameter list for internal thermal noise calculations

Lastly, the remaining parameters are:

Name	Symbol	Value	Units
Absorbed power	W_0	$1.5 \cdot 10^{-3} \leq W_0 \leq 1$	W
Beam radius	r_0	$10^{-3} \leq r_0 \leq 6 \cdot 10^{-2}$	m
Coating thickness	d	$\approx 6 \cdot 10^{-6}$	m
Interferometer length	L	$4 \cdot 10^3$	m

The analytical expressions for the various thermal noise effects are

$$\begin{aligned}
S_{TE}(\omega) &= \frac{4\sqrt{2}(1+\nu)^2 \alpha^2 d^2 k_B T^2}{\pi r_0^2 \sqrt{\kappa \rho C \omega}} \\
S_{PT}(\omega) &= 2\alpha^2 \frac{\hbar \omega_0 W_0}{(\rho C \pi r_0^2)^2 \omega^2} \\
S_{TR}(\omega) &= \frac{\beta^2 \lambda^2 k_B T^2}{\pi r_0^2 \sqrt{\rho C \kappa} \sqrt{\omega}} \\
S_{BN}(\omega) &= \frac{4k_B T(1-\nu^2)\phi}{\omega \sqrt{2\pi} E r_0}.
\end{aligned} \tag{A.1}$$

In the expression for the thermoelastic noise the parameter α needs to be modified accordingly to the theoretical analysis we carried out in Chapter 4. This means that

$$\alpha = \alpha_1 \frac{d_1}{d_1 + d_2} + \alpha_2 \frac{d_2}{d_1 + d_2} \frac{E_2(1-2\nu_1)}{E_1(1-2\nu_2)} \tag{A.2}$$

where the index 1 refers to fused silica and index 2 refers to Tantal pentoxide. Moreover,

$$d_i \equiv \frac{\lambda}{4n_i} \tag{A.3}$$

where $i = 1, 2$. All other material parameters refer directly to fused silica. Regarding thermorefractive noise we observe that

$$\beta = \frac{n_1 n_2 (\beta_1 + \beta_2)}{4(n_1^2 - n_2^2)} \tag{A.4}$$

where the indices refer to the different materials. The other two noises can be computed by direct substitution of the proper parameters, taking care to use those of the fused silica material.

Finally, we show how these noises affect the sensitivity of a GW detector. To do this we have to take the square root of the power spectral density of each noise and divide by the length of the detector¹ (is it easy to check that these quantities have the expected

¹the numerical factors 2 or 4 take into account how many independent noise contributions have to be added together. The numerical factor 4 corresponds to the four mirrors (two for each cavity) whose noises have to be independently added together. However, in the case of thermoelastic noise one must observe that only one the “end mirror” in each arm contributes to the noise since the other must have a much lower reflectivity to let the laser light couple into the arm resonators. (This of course applies to laser interferometers with arm cavities as LIGO).

dimensions, namely $(\text{Hz})^{-1/2}$.

$$\begin{aligned}
 h_{TE} &= \frac{\sqrt{2S_{TE}(\omega)}}{L} \\
 h_{PT} &= \frac{\sqrt{4S_{PT}(\omega)}}{L} \\
 h_{TR} &= \frac{\sqrt{4S_{TR}(\omega)}}{L} \\
 h_{BN} &= \frac{\sqrt{4S_{BN}(\omega)}}{L}.
 \end{aligned}
 \tag{A.5}$$

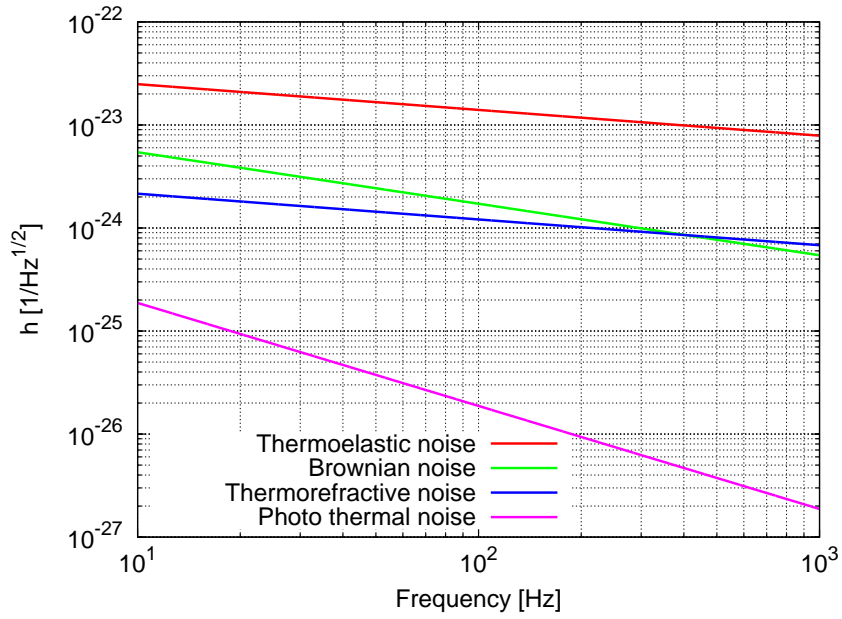


Figure A.1.: Limit to the sensitivity of the LIGO detectors due to thermal noise effects. The parameters used are exactly as given by Braginsky [4]. The reproduction of this known result was also a check that the formulas and parameters we used were correct, apart from a slight deviation in the case of the thermorefractive noise of unclear origin.

B. Shot noise and electronic noise sources

We estimate here the various noises that will be introduced by the experimental setup in order to be sure that these will not compromise the whole measurement. The experiment is in principle simple: we send an intensity- and frequency-stabilized laser beam to the etalon and measure the transmitted light by means of a photodetector (which includes a transimpedance amplifier) and a spectrum analyzer. Since the etalon's transmitted power is a non-linear function of the frequency, the working point has to be chosen to maximize the sensitivity, or, other words, to maximize the conversion factor from Hz to Volt. The detection of the signal itself deserves some further discussion, since we need to keep two noise sources at a level such that they do not spoil the whole detection scheme. These noise sources are the shot noise (of the laser beam) and the electronic noise.

B.1. Shot noise

Shot noise affects virtually every measurement involving lasers. The physical mechanism for shot noise lies in the quantum nature of light. This means a measurement of light amounts to a “counting process”, and this counting process carries a fundamental noise with it. The relevant equation is [21]

$$\Delta I = \sqrt{2eI_0} \quad (\text{B.1})$$

where e is the electron charge, I_0 is the photocurrent and ΔI the linear spectral density of I_0 .

We see that shot noise affects the photocurrent and the higher the photocurrent, the lower the relative noise. The laser light hitting the photodiode has a power P_0 , and the resulting photocurrent is given by

$$I_0 = \gamma P_0 \quad (\text{B.2})$$

with a efficiency γ which is of the order of

$$\gamma \approx 0.5 \text{ AW}^{-1}. \quad (\text{B.3})$$

In order not to damage the etalon, we set the laser power at $P_0 = 1 \text{ mW}$. A laser beam of $P_0 = 1 \text{ mW}$ has a shot noise of

$$\Delta I \equiv I_{shot} = \sqrt{2e\gamma P_0} = 1.26 \cdot 10^{-11} \frac{\text{A}}{\sqrt{\text{Hz}}} \quad (\text{B.4})$$

This fundamental noise source set a sort of “border” between the photocurrent resulting from the internal thermal noise, which must be bigger than I_{shot} , and the electronic noise sources which, once converted to current noises, should be smaller than I_{shot} .

B.2. Electronic noise sources

In order to convert the light into an electric signal some circuitry has to be employed. As we said, the electronic noise should not overcome the shot noise, what we need is a shot noise limited detection scheme. The detector is basically composed of a high efficiency photodiode and a transimpedance amplifier, as shown in Figure B.1. If we consider

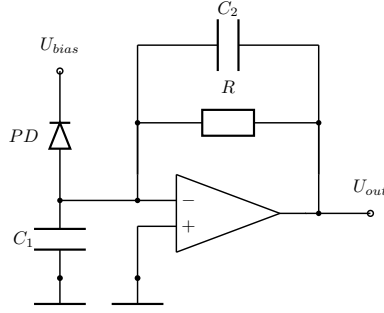


Figure B.1.: A transimpedance amplifier is used to convert a current signal (in this case produced by the photodiode PD) into a voltage signal U_{out} that is better suited for analysis by means of a spectrum analyzer.

the photodiode as a “black box” that cannot be tuned, we are left with the design of a transimpedance amplifier, that is the device which converts the photocurrent produced by the photodiode into a voltage signal. Our analysis will closely follow that developed in [22]. The capacitor C_1 is used to take into account the internal capacitance of the photodiode itself (and in order to keep this unwanted effect at a minimum it is customary to bias the photodiode at U_{bias}). The capacitor C_2 ensures the stability of the circuit. The resistor and the operational amplifier are noisy components and because of them, at the the circuit’s output three additional noises appear, namely:

- Thermal Johnson noise $U_j = \sqrt{4k_B T R}$
- Operational amplifier current noise I_n
- Operational amplifier voltage noise U_n

where k_B is the Boltzmann’s constant, T is the temperature. The requirement is that each of these noises should not exceed the the noise produced by the light itself, namely the shot noise. Since the shot noise at the input of the operational amplifier is

$$\Delta I \equiv I_{shot} = \sqrt{2eI_0} \quad (\text{B.1})$$

this noise will appear at the output as

$$U_{shot} = R I_{shot}. \quad (\text{B.2})$$

We get

$$U_{shot} > \max(U_j, U_i, U_n) \quad (\text{B.3})$$

where

$$U_i = RI_n. \quad (\text{B.4})$$

I_n, U_n are the input noise current density and the input noise voltage density respectively. These two last parameters are specific to each operational amplifier and can be found in the respective datasheets. Now we can perform a quantitative analysis of the noises added by the transimpedance amplifier with respect to the shot noise level. We take for the electronic circuit a feedback resistance of $R = 1 \text{ k}\Omega$ and an OP-27 low noise operational amplifier. Then

$$U_{shot} = RI_{shot} = 1.26 \cdot 10^{-8} \frac{\text{V}}{\sqrt{\text{Hz}}} \quad (\text{B.5})$$

$$U_j = 4 \cdot 10^{-9} \frac{\text{V}}{\sqrt{\text{Hz}}} \quad (\text{B.6})$$

$$U_n = 3 \cdot 10^{-9} \frac{\text{V}}{\sqrt{\text{Hz}}} \quad (\text{B.7})$$

$$U_i = 1 \cdot 10^{-9} \frac{\text{V}}{\sqrt{\text{Hz}}}. \quad (\text{B.8})$$

We can see that the condition expressed by the inequality (B.3) can be easily satisfied.

The analysis we carried out refers to signals that do not depend on time, this is usually the first step in a design process, however, since the signals we want to measure are time dependent, additional issues such as bandwidth and stability need to be studied. The resistance R , for example, has a feedback effect on the operational amplifier, and this feedback circuit has to be stable. From the producer's datasheet and application notes it is possible to find out the values of the capacitance C_2 that is needed to ensure the stability of the circuit. It should also be clear that this value depend also on R and in our case it may be easily found that the required capacitance is of the order of the pF. In such cases it can be omitted, taking into account that such tiny capacitances are always present in a real circuit.

C. Etalon simulations

The etalon was simulated by using a simulation program written by Roland Schilling. The program requires the user to write a file resembling a Fortran 90 source code file, describing the optical system to be simulated. Such a file is shown in Listing C.1: it is easy to recover the parameters used in this example:

- Laser beam waist: 1 mm.
- Resonant cavity length: 10λ .
- Transmissivity of each surface $T = 100$ ppm.
- Losses at each surface $A = 30$ ppm.
- Refraction index of the material between the two high reflectivity surfaces: $n = 1.45$.
- Planarity: $\theta = 0$ rad.

Two parameters are especially important for the computation:

- Dimension of the grid: $2^7 \times 2^7$.
- Number of round trips: 20000.

The dimension of the grid is simply the number of “pixels” in which the input beam is decomposed. In principle, the finer the grid the better. In reality, this value was the finest allowable, since a finer grid caused the computation time to exceed the limit set by the time-sharing system.

Listing C.1: input file for the WaveProp program.

```
1   Program MICROCAV
2   !
3   ! Simulate a plane - plane miniature FP cavity.
4   !                               Roland Schilling, 02 Nov 2006
5   !                               Last modified:   03 May 2007
6   !
7   use rsutil           ! utility package
8   use rsplot          ! plot package
9   use waveprop        ! wave-propagation package
10  !
11  integer ,            parameter :: nx=7      ! 2**nx grid points in x and y direction
12  !
13  character            :: fileout*32
14  integer              :: irt, nrt, ic(10)
15  real                 :: wi, lambda, dist, sog, rl, rt(1000), pwi(1000)
16  type(field)         :: psi_in             ! initial field
17  type(field)         :: psi_ci            ! cavity input field
18  type(field)         :: psi_ca            ! cavity field
```

C. Etalon simulations

```

19     type(field)           :: psi_ct           ! transmitted field
20     type(surface)        :: mfp1, mfp2       ! cavity mirrors
21 !
22 ! Set parameters:
23     nrt    = 20000         ! number of round trips in cavity
24     sog    = 10.0         ! size of the grid in one dimension [mm]
25     lambda = 1.064e-3     ! light wavelength [mm]
26     dist   = 10*lambda    ! length of cavity [mm]
27     wi     = 1.0000       ! radius of initial beam [mm]
28     ri     = 1.45
29     mfp1%n1 = ri
30     mfp2%n1 = ri
31     mfp1%t = sqrt(100.e-6) ! transmittance of cavity input mirror
32     mfp1%r = sqrt(1-130.e-6) ! reflectance of cavity input mirror
33     mfp2%t = sqrt(100.e-6) ! transmittance of cavity end mirror
34     mfp2%r = sqrt(1-130.e-6) ! reflectance of cavity end mirror
35     mfp2%ti= 0.e-7        ! tilt of cavity end mirror
36 !
37     fileout=arg(0)
38     u_norm=-gun()         ! write output to file _and_ to terminal
39     if (u_norm /= 6) open(abs(u_norm),file=trim(fileout)//'.log')
40 !
41 !call saft(timing=1)
42     call wp_init(nx,sog,fftw='m',unit='mm',nthreads=4) ! initialize WaveProp
43     rl=pi*wi**2/lambda
44     call msg(0,'\ Rayleigh length = '//trim(r2c(rl))//' mm\\')
45     call hg_mode(psi_in,wi) ! generate initial field
46     call transmit(psi_in,mfp1,'b',psi_out=psi_ci)! transmit through input mirror
47     call set_up(psi_ca,ri) ! set up and clear cavity field
48                             ! added argument ri 04/05/2007
49     call set_up(psi_ct) ! set up and clear transmitted field
50     call set_up(mfp1) ! set up cavity input mirror
51     call set_up(mfp2) ! set up cavity end mirror
52     np=0 ! number of points for plotting
53     is=1 ! print output every 'is' round trips
54     do irt=1,nrt ! do nrt round trips
55         call reflect(psi_ca,mfp1) ! reflect at near mirror
56         call interfere(psi_ci,psi_ca,psi_ca,'c',pw_c=pw)
57         if (mod(irt,is) == 0) then
58             np=np+1
59             rt(np)=real(irt)
60             pwi(np)=pw
61             call msg(0,' irt = '//trim(i2c(irt,'I6'))// ' &
62                 ' pwi = '//trim(r2c(pw,'E4.3e+'))')
63             if (irt == 10) then
64                 is=2
65             else if (irt == 30) then
66                 is=5
67             else if (irt == 100) then
68                 is=20
69             else if (irt == 300) then
70                 is=50
71             else if (irt == 1000) then
72                 is=200
73             else if (irt == 3000) then
74                 is=500
75             end if
76         end if
77         call propagate(psi_ca,dist) ! propagate to far mirror
78         if (irt == nrt) psi_ct=psi_ca ! transmitted field
79         call reflect(psi_ca,mfp2) ! reflect at far mirror
80         call propagate(psi_ca,dist) ! propagate to near mirror
81     end do

```

```

82     call transmit(psi_ct,mfp2)           ! transmit through end mirror
83     call plot_3d(psi_in,4,'Input power',zoom=2.)      ! plot input field
84 !   call plot_3d(psi_ct,4,'Transmitted power',zoom=2.) ! plot xmitted field
85     call transmit(psi_ca,mfp1)          ! transmit through input mirror
86     call reflect(psi_in,mfp1,'b')       ! reflect at input mirror
87     call interfere(psi_in,psi_ca,psi_ca,'d') ! destructive interference
88     call plot_3d(psi_ca,4,'Reflected power',zoom=2.) ! plot return. field
89 !   call plot_3d(psi_ca,4,'Reflected power',cut=0.5,zoom=2.)
90     call plot_3d(psi_ct,4,'Transmitted power',zoom=2.) ! plot xmitted field
91     call plot_3d(psi_ct,4,'Transmitted power',cut=.5,zoom=2.) ! xmitted field
92     pwt=sum(abs(psi_ct%a)**2)
93     call msg(0,'\ Transmitted power = '//trim(r2c(pwt))//' W\\')
94 !
95     call ps_init
96     call ps_frame(1,1.,1.e-5,real(nrt),1.e4,60.,xlog=1,ylog=1,clip=1)
97     call ps_grid(1,'10:*10','1e-6:*10',lw=.2,ci=14)
98     call ps_grid(1,' 2:*10',lw=.2,ci=14)
99     call ps_grid(1,' 5:*10',lw=.2,ci=14)
100    call ps_axis(1,ax='Xx',title='Number of round trips',d_tl=10.)
101    call ps_axis(1,ax='Yy',title='Light power in FP cavity [W]', &
102              d_tl=10.,exp=0,d_tm=.5)
103    call ps_plot(1,np,rt,pwi)           ! power in FP cavity
104 !
105 !call sf_usage('')
106     call wp_exit
107     end

```

The number of the round trips is the number of round trips made by a single photon inside the etalon. This is an important parameter, since the program is able to compute the laser power inside the resonator. Since this quantity has to reach a steady state in resonance, one has to set the number of round trips to a value such that the power inside the resonator becomes constant with respect to the number of round trips. In Figure C.1 we show the power inside the resonator as a function of the computed round trips: it can be seen that 20000 round trips should at least be computed in order to get meaningful values. Since this parameter also heavily affects the computation time, this value was the highest one we could use.

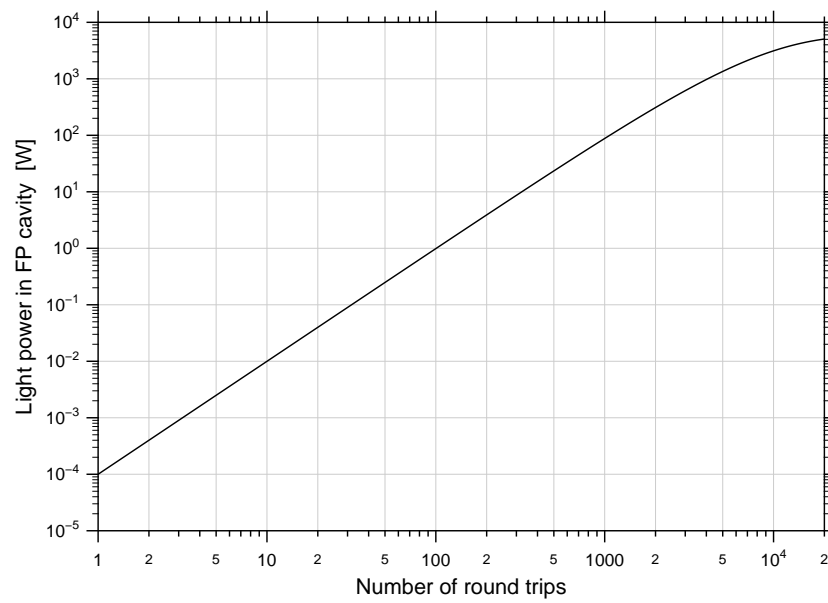


Figure C.1.: The power inside the resonator as a function of the number of computed round trips. The power approaching a stationary state indicates the appropriate number of round trips to be computed to obtain meaningful results.

Bibliography

- [1] Peter R. Saulson. Thermal noise in mechanical experiments. *Phys. Rev. D*, 42(8), 1990.
- [2] V.B. Braginsky and S.P. Vyatchanin. Thermodynamical fluctuations and photo-thermal shot noise in gravitational wave antennae. *Phys. Lett. A*, 264:1–10, 1999. Also available in internet as <http://arxiv.org/cond-mat/9912139>.
- [3] V.B. Braginsky, M.L. Gorodetsky, and S.P. Vyatchanin. Thermorefractive noise in gravitational wave antennae. *Phys. Lett. A*, 271:303–307, 2000. Also available as <http://arxiv.org/cond-mat/0008109>.
- [4] V.B. Braginsky and S.P. Vyatchanin. Thermodynamical fluctuations in optical mirror coatings. *Phys. Lett. A*, 312:244–255, 2003. Also available as <http://arxiv.org/cond-mat/0302617>.
- [5] J.H. Taylor and J.M.Weisberg. A new test of General Relativity: Gravitational Radiation and the Binary Pulsar PSR1913+16. *The Astrophysical Journal*, 253:908–920, 1982.
- [6] H.Lück et al. Status of the GEO600 detector. *Class. Quantum Grav.*, 23:S71–S78, 2006.
- [7] H. B. Callen and R. F. Greene. On a theorem of irreversible thermodynamics. *Phys. Rev.*, 86(4), 1952.
- [8] L. D. Landau and E. M. Lifschitz. *Lehrbuch der Theoretischen Physik. Band 1: Mechanik*. Akademie Verlag, 1984.
- [9] Volker Leonhardt. *Displacement measurements on suspended mirrors for off-resonant thermal noise detection*. PhD thesis, University of Hannover, 2003.
- [10] L. Meirovitch. *Principle and techniques of vibrations*. Prentice-Hall, 1997.
- [11] G.Cella. Private communication.
- [12] A. Vicerè. Introduction to the mechanical simulation of seismic isolation systems. In M. Mazzoni R. Stanga M. Barone, G. Calamai and F. Vetrano, editors, *Experimental physics of Gravitational Waves*, pages 349–378, 2000.
- [13] E.C. Pestel and F.A.Leckie. *Matrix methods in elastomechanics*. McGraw-Hill, 1963.
- [14] R.W.Hamming. *Numerical Methods for Scientists and Engineers*. Dover Publications, 1973.

- [15] L. D. Landau and E. M. Lifschitz. *Teoria dell'elasticità*. Editori riuniti, 1979.
- [16] I.S. Gradshteyn and I.M. Ryzhik. *Table of integrals, series and products*. Academic Press, 2000.
- [17] Gröbner and Hofreiter. *Integraltafel Teil 2: Bestimmte Integrale*. Springer, 1973.
- [18] M. Born and E. Wolf. *Principles of Optics*. Cambridge University Press, 1999.
- [19] W. Demtröder. *Experimentalphysik 2*. Springer, 2006.
- [20] E. Black. Direct Observation of Broadband Coating Thermal Noise in a Suspended Interferometer. Available as <http://arxiv.org/gr-qc/0401034>.
- [21] Oliver Sascha Brozek. *Frequenzstabilisierung eines Nd:YAG-Hochleistungs-Laser-Systems für den Gravitationswellendetektor GEO600*. PhD thesis, university of Hannover, 1999.
- [22] Gerhard Heinzel. *Advanced optical techniques for laser-interferometric gravitational-wave detectors*. PhD thesis, University of Hannover, 1999.

Thanks

Lots of people contributed to this work, directly and indirectly. At the top of the list is my family which granted me the warm environment and the daily comforts that enabled me to spend my time with books and computers since my childhood.

While being at high school, my inclination toward physics was amplified by my physics teacher, who taught me to pay due attention to the units of measurement in *every* calculation. At University I enjoyed highly competent professors and a handful of true friends that helped me a lot. Among my friends Riccardo Natali is due special credit for his help when I most needed it: thanks.

My PhD work was in the first place possible due to the generous scholarship that I got from Prof. Dr. Karsten Danzmann. He showed himself to be a fine scientist and boss too. Dr. Harald Lück helped me a lot during my thesis, and I will always remember his constant effort to concentrate the forces to the solution of scientific problems, thereby making everything else irrelevant and not worth worrying about. The first half of my PhD work took place in strong collaboration with Dr. Volker Leonhardt: he taught me most of the experimental physics I know. Thanks to all the people at the Albert Einstein institute in Hannover.

On the private side I must mention Eva who showed me that there are things in life more important than science.

Thanks to Dr. Benjamin Sheard, Dr. Paul Cochrane and Dr. Harald Lück for proof-reading this work.

Thanks to Dr. Hung for his help in simulating the etalon's coating process.

Thanks to Roland Schilling who introduced me to his simulation program for optical systems, and let me use one of the high-performance computers of the "Garching computer farm".

Thanks to Alexander Franzen who crafted some of the graphics I used in my figures.

Thanks to Prof. Knuth for his T_EX typesetting system.

Thanks to the Linux community. I came in contact with a Unix-like system at high school so that my astonishment is great every time I think that a Unix-like operating system is now available *for free* and for every computer.